FUNDAMENTAL INVESTIGATIONS OF CUTTING OF SILICON FOR PHOTOVOLTAIC APPLICATIONS

A Thesis
Presented to
The Academic Faculty

By

Hao Wu

In Partial Fulfillment of the
Requirements for the Degree of
Doctor of Philosophy

The George W. Woodruff School of Mechanical Engineering
Georgia Institute of Technology
December 2012

FUNDAMENTAL INVESTIGATIONS OF CUTTING OF SILICON FOR PHOTOVOLTAIC APPLICATIONS

Approved by:

Dr. Shreyes Melkote, Advisor
School of Mechanical Engineering
Georgia Institute of Technology

Dr. Jianjun Shi
School of Industrial & System Engineering
Georgia Institute of Technology

Dr. Steven Danyluk
School of Mechanical Engineering
Georgia Institute of Technology

Dr. Naresh Thadhani
School of Materials Science & Engineering
Georgia Institute of Technology

Dr. Steven Liang
School of Mechanical Engineering
Georgia Institute of Technology

Date Approved: October 9, 2012

This thesis is dedicated to

My family

For their love

ACKNOWLEDGEMENTS

First of all, I would like to express my sincere gratitude to my thesis advisor, Professor Shreyes N. Melkote, for his continuous support, mentorship and encouragement throughout my research activities in the area of Photovoltaic manufacturing at Georgia Tech. In the last four years, he created tremendous amount of opportunities for me to think, reflect, learn and grow. I would also like to thank Prof. Steven Danyluk, Prof. Steven Liang, Prof. Jianjun Shi and Prof. Naresh Thadhani for serving on my thesis committee and overseeing my thesis work.

My gratitude is also extended to the Photovoltaic manufacturing research group at the school of Mechanical Engineering. They are Prof. Steven Danyluk, Dr. Chris Yang, Dr. Frank Mess, my office buddies Kevin Skenes, Yury B. Pyekh, Rajaguruprasath Raveendran and Arkadeep Kumar and former group members Dr. Xavier Brun and Dr. Fang Li. Thanks to them for tirelessly listening to my Friday PV meeting presentations and providing invaluable feedback and recommendations. Talking and hanging out with Kevin has been a lot of fun. Post-soccer game beer with Yury and other European fellows are wonderful memories. Watching Euro 2012 and London Olympics in office with them gave me the best summer ever in Atlanta.

I also would like to acknowledge the support, help and entertainment I have been enjoying from my fellow coworkers in Prof. Melkote's group at PMRC. They are Dr. Mukund Kumar, George Mathai, Richard Marsh, Rui Liu, Craig Woodin, Christian Biggs, Andrea Macon, Jennifer Flachs, Prof. Keiji Ogawa, Satyanarayanan Raghavan and John Morehouse. Gun shooting on 4th of July holiday at Richard's parents' in South Carolina was a lot of fun. Thanks

to Steven Sheffield for manufacturing the parts for my experiment setup and Pam Rountree for her help in administrative issues.

I give my appreciation to friends and colleagues from the System Realization Laboratory of the School of Mechanical Engineering for their support during the first year of my study in Georgia Tech. They are my former advisor Dr. Mervyn Fathianathan, Sen Yang, Dr. Fei Ding, Chenjie Wang, Xiayun Zhao, Jiten Patel, Prof. David W. Rosen, Prof. Jitesh H. Panchal and Prof. Janet Allen.

Special thanks to my friends, Sen Yang, Dr. Chunhui Lu and Xi Liu for stepping out and help when I was involved in trouble. Life was not always easy but I have been fortunate to enjoy most of it with friends in Atlanta.

The financial support from Silicon Solar Consortium (SiSoC), a National Science Foundation Industry/University Cooperative Research Center, on my thesis research is acknowledged. SiSoC provides a platform for me to learn to be a professional beyond academia.

Finally, I would like to thank my family, my grandfather Baohua Wu, grandmother Xiulan Zhong, father Zhenyu Wu, mother Anfang Zou, brothers Dong Wu and Jie Wu, for their love and support and would like to dedicate this thesis to them.

TABLE OF CONTENTS

LIST OF TABLES

LIST OF FIGURES

SUMMARY

Crystalline silicon (Si) wafers used as substrates in the semiconductor and photovoltaic (PV) industries are traditionally manufactured using a multi-wire slurry sawing (MWSS) technique. Due to its high productivity potential, the fixed abrasive diamond wire sawing (DWS) technique is of considerable interest to Si wafer producers. Although both sawing techniques are currently used in the industry, a fundamental understanding of the underlying process is still lacking, particularly for diamond wire sawing. Consequently, optimization of the wire sawing process is carried out largely based on experience and trial and error.

This thesis aims to develop a systematic fundamental understanding of diamond wire sawing of Si materials used for PV applications. First of all, a comparative analysis of the characteristics of silicon wafers cut by slurry and fixed abrasive diamond wire sawing is presented. The analysis results indicate that fixed abrasive diamond wire sawing may be a viable alternative to slurry wire sawing.

Modeling and experimental studies of single grit diamond scribing of Si are proposed to shed light on the basic cutting mechanisms. Although Si is brittle at room temperature, it is possible to properly control the cutting conditions to obtain a completely ductile mode of material removal. The effects of material anisotropy, abrasive grit shape, friction condition and external hydrostatic pressure on the ductile-to-brittle mode transition in cutting of single crystal Si (c-Si) are systematically investigated.

Multicrystalline Si (mc-Si) based solar cells take up the majority of the global PV market. Hard inclusions (SiC and Si_3N_4) in multicrystalline Si (mc-Si) ingots may cause

wire breakage and negatively impact the process, surface/subsurface morphology and mechanical properties of the resulting wafer. Their effects are experimentally studied through the single grit diamond scribing on the mc-Si sample with high density of inclusions. Finally, it is identified that there is a correlation between the high dislocation density and the increase of fracture toughness in mc-Si. The increase in fracture toughness leads to greater capability of ductile mode of cutting and higher specific scribing energy in the brittle fracture regime.

Results of these fundamental investigations are expected to generate useful knowledge for optimizing the diamond wire sawing process in order to achieve high productivity and minimum surface/subsurface damage.

CHAPTER 1

INTRODUCTION

This chapter presents the background of the research in wire sawing of silicon for Photovoltaic applications. Fundamentals of the wire sawing operation will be described, followed by the research questions, objectives and approach adopted in this study. Finally, the outline of this dissertation will be presented.

1.1 Wire Sawing of Silicon for PV Manufacturing

Crystalline silicon (Si) continues to be the dominant material used in the manufacture of commercial solar cells. The cost to produce Si wafers accounts for approximately 30-40% of the total solar cell fabrication cost [1-3]. Traditionally, Si wafers are cut from ingots using the multi-wire slurry sawing (MWSS) technique [4]. A schematic of the multi-wire slurry sawing technology is shown in Fig. 1.1. A single stainless steel wire is fed from a supply spool through a pulley and tension control unit to the wire guides. Multiple strands of a wire web are formed by winding the wire through the 500-700 parallel grooves on the wire guides. The wire web is pulled by the torque applied by the main drive and slave rolls, while at the same time, the Si ingot, glued to the holder, is fed against the moving wire web and sliced into hundreds of wafers. Cutting is achieved by silicon carbide (SiC) abrasive slurry, which is supplied through nozzles over the wire web and carried by the wire into the sawing channel. The slurry is typically oil or polyethylene glycol (PEG) based [4].

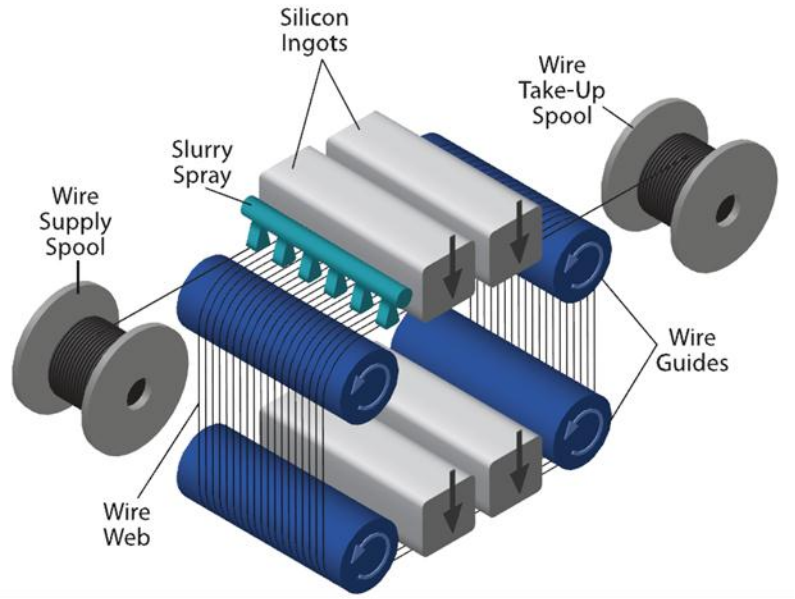

Figure 1.1: Schematic of multi-wire slurry sawing of silicon wafers [5].

Compared with other methods (such as Inside Diameter (ID) sawing and Outside Diameter (OD) sawing), the multi-wire slurry sawing technique has the advantages of large throughput and the ability to cut ingots of large size. However, the MWSS process is very slow, thereby compromising productivity. Recently, the multi-wire fixed abrasive diamond wire sawing (DWS) technology has rapidly gained industrial attention due to its potential for two to three times higher productivity and the potential for kerf recycling. Instead of using abrasive slurry, the stainless steel wire used in DWS is impregnated or electroplated with diamond grits that serve as fixed cutting points. Water based slurry is typically used. An example of the commercially available diamond wire is shown in Fig. 1.2.

Although the actual operation systems share similar features, the slurry sawing process is fundamentally different from the diamond wire sawing process. As shown in Fig. 1.3(a), the schematics of the sawing channel, material removal in slurry sawing is

achieved by the interactions between the SiC particles, the slurry and the Si substrate, this process is referred to as three-body-wear in tribology. In diamond wire sawing, however, the Si substrate is removed through two-body-wear, which involves the direct interaction of the diamond grits with the silicon ingot materials, as shown schematically in Fig. 1.3(b).

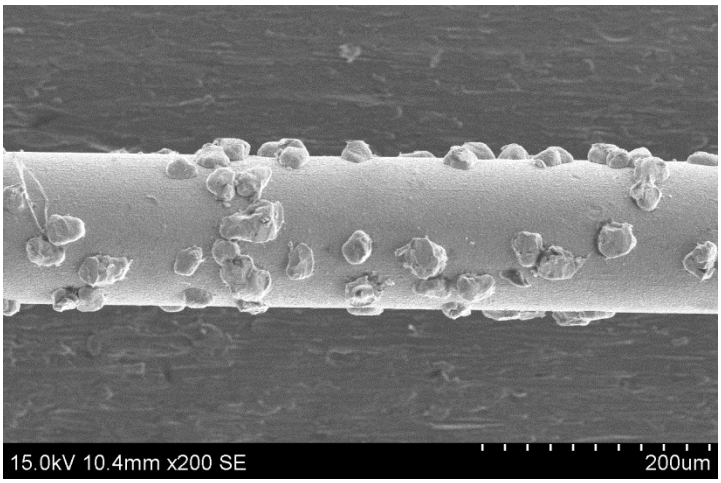

Figure 1.2: Scanning electron microscope (SEM) image of diamond wire.

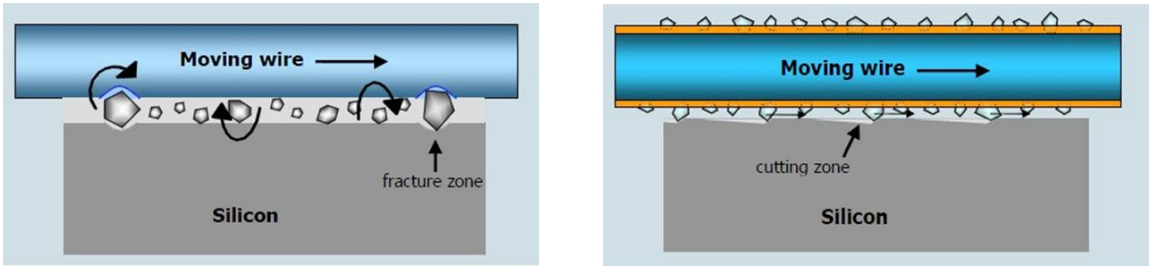

(a) (b)

Figure 1.3: Schematics of the cutting operations in the sawing channel: slurry sawing (a), diamond wire sawing (b) [6].

1.2 Research Goals and Objectives

It has been reported that the sawing costs continue to be high and account for approximately 10-20% of wafer production costs [1, 2]. Therefore, there is an incentive to optimize the sawing process for further cost reduction and wafer quality control. The specific optimization objective in sawing is to enhance productivity with a minimum loss of Si and slurry, and produce high quality wafers in terms of mechanical and electrical properties. However, the sawing performance is determined by many parameters such as the type of Si material (single or multicrystalline), wire tension, wire speed, feed rate, grit size and shape, and the viscosity of cutting fluid or slurry, etc. Due to the many parameters that can be manipulated, optimization of the sawing process is challenging and is mainly guided by experience.

The goal of this research is to develop fundamental knowledge of the cutting action of Si in the diamond wire sawing process. Since material removal is carried out simultaneously by many abrasives of varying shape and size, a fundamental investigation of single grit diamond scribing on silicon is proposed to understand the fundamental cutting mechanisms in wire sawing within particular emphasis on the DWS process.

It is well-known that although silicon is brittle at room temperature, it exhibits ductile behavior when cut at low feed rates [7]. Although considerable work on cutting of semiconductor grade Si using diamond turning and similar methods has been carried out, scientific understanding of cutting of PV silicon materials using either wire sawing process is very limited. In particular, the influence of material anisotropy, abrasive shape and frictional condition on the mode of material removal (ductile vs. brittle) and surface/subsurface condition and properties are not fully understood. This is especially true for mc-Si materials commonly used as the substrate in PV applications [1].

Both monocrystalline and multicrystalline Si are used for the manufacturing of Si solar cells. Monocrystalline/single crystal Si (c-Si) materials used for PV applications are grown using the Czochralski (CZ) method. Multicrystalline Si is grown by a casting technique using a directional solidification process. The direct purification of metallurgical silicon through melting and solidification yields less pure feedstock Si. Compared with c-Si, mc-Si materials contain extended lattice defects, such as dislocations and grain boundaries, precipitates such as oxygen, carbon and metallic elements, as well as hard inclusions such as silicon carbide (SiC) and silicon nitride (Si_3N_4) [8]. Fig. 1.4 shows a pseudo-square 156mm x 156mm c-Si wafer and a square 156mm x 156mm mc-Si wafer.

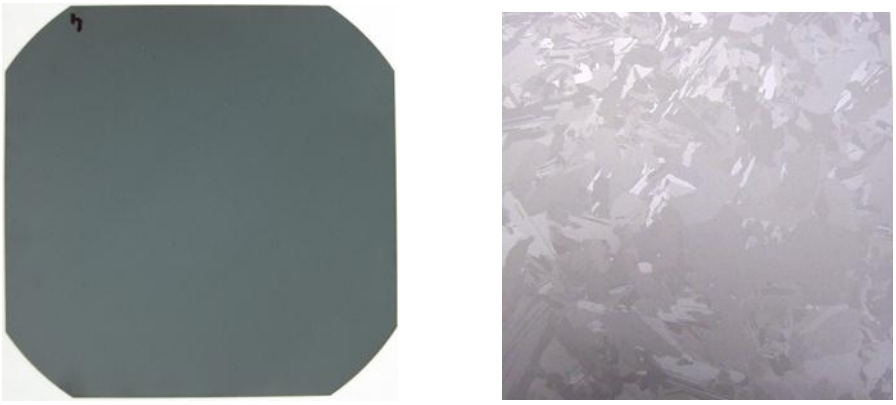

(a) (b)

Figure 1.4: sc-Si wafer (a) vs. mc-Si wafer (b).

Industrial practice has shown that diamond wire sawing of mc-Si ingots is still a challenge while c-Si materials can be successfully sawn by diamond wire sawing. In this study, it is hypothesized that the dislocation clusters in mc-Si can negatively influence the material mechanical property such that the mc-Si substrate is more difficult to cut.

Furthermore, SiC and Si_3N_4 hard inclusions can affect the sawing process and the resulting surface properties and those effects need to be investigated.

The research objectives of this dissertation can be summarized as follows:

- Investigate the characteristics of the silicon wafers cut by both slurry wire sawing and diamond wire sawing.
- Study the effects of material anisotropy (crystallographic orientation), abrasive shape, and frictional conditions generated by different cutting fluids on the mode of cutting of single crystal Si.
- Investigate the interactions of single grit diamond cutting grit and SiC and Si_3N_4 hard inclusions and the implications to diamond wire sawing of mc-Si material.
- Investigate the effects of dislocation density on mechanical properties and cutting performance of mc-Si.

1.3 Dissertation Outline

Chapter 2 of this dissertation provides a thorough literature review on the research of mechanical properties of crystalline silicon, wire sawing technique, fundamental study of abrasive machining of brittle materials, as well as the understanding of the effects of crystal defects (dislocation) and hard inclusions on the mechanical properties and cutting performance of mc-Si.

Chapter 3 presents a comparative study of Si wafers cut by slurry sawing and diamond wire saw techniques. Various metrological properties such as surface

morphology and roughness, thickness variation and the mechanical strength of wafers produced by those the two techniques are analyzed.

Chapter 4 focuses on the effect of crystallographic orientation on the ductile scribing of c-Si. A crystal plasticity based analysis will be given to explain the experimental observations.

Chapter 5 describes the modeling and experimental study of the ductile-to-brittle cutting mode transition in single grit diamond scribing of silicon. The Extended Finite Element (XFEM) method is used to model the effects of diamond scriber tip geometry and frictional conditions on the cutting mode.

An experimental investigation of the influence of SiC and Si_3N_4 inclusions on single grit diamond scribing of mc-Si is presented in Chapter 6. Implications for the actual diamond wire sawing operation are also discussed.

Chapter 7 studies the correlation between the dislocation density in mc-Si materials and the corresponding material mechanical properties which can significantly influence the wire sawing performance.

Chapter 8 summarizes the main conclusions of the dissertation and its implications for optimization of the diamond wire sawing process, and presents recommendations for further research.

CHAPTER 2

LITERATURE REVIEW

This chapter contains a review of prior research in the following areas that are relevant to the proposed work: (1) Mechanical properties of crystalline silicon, (2) Wire sawing methods, (3) Single grit scribing of Si and other brittle materials, (4) Hard inclusions in multicrystalline silicon, and (5) Effects of dislocation and grain boundary on mechanical properties of mc-Si. Based on existing knowledge, research objectives and specific research questions of this dissertation are put forth.

2.1 Mechanical Properties of Crystalline Silicon

The knowledge of mechanical behavior of crystalline silicon materials is essential for the study of cutting of silicon. At room temperature and ambient pressure, silicon has anisotropic elastic properties due to its diamond cubic crystal structure. However, silicon undergoes phase transformation under very high compressive loading conditions. The phase transformation process and the transformed silicon phases demonstrate different mechanical behaviors than the normal diamond cubic silicon. The crystal structure and elastic properties of diamond cubic silicon will be presented in this section, followed by a summary of the phase transformation behavior of silicon.

2.1.1 Crystal Structure and Elastic Constants of Silicon

The crystal structure of Si is diamond cubic, consisting of a face-centered cubic lattice with a two-atom basis of (0, 0, 0) and (1/4, 1/4, 1/4), as shown in Fig 2.1. The atoms

are four-fold coordinated into regular tetrahedrons, reflecting the hybridized sp3 bonding [9]. The {111} planes are the most close packed. The elastic properties of Si single crystals reflect the underlying anisotropy of bonding, yielding direction dependent Young's modulus, shear modulus and Poison's ratio. As an example of anisotropy, the Young's modulus as a function of crystallographic orientation is shown in Fig 2.2. The theoretical elastic modulus varies from 187 GPa in the <111> direction to 130 GPa in the <100> direction, with an intermediate value in the <110> directions of 169 GPa.

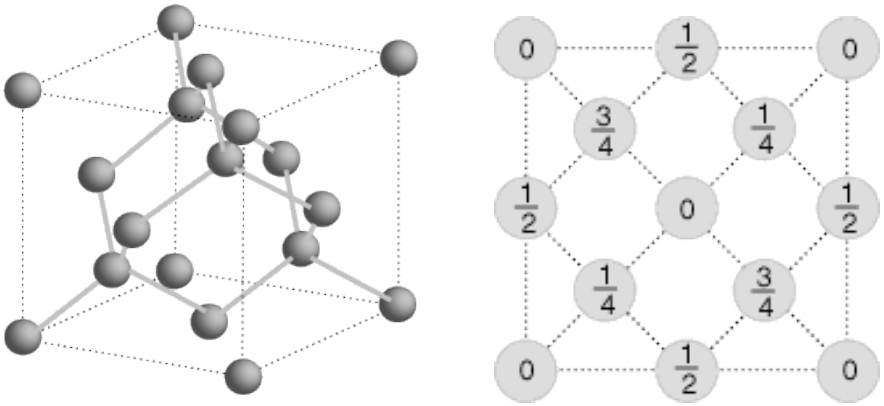

Figure 2.1: Silicon crystal structure in 3D and 2D projection [9].

According to the generalized Hooke's law, for anisotropic materials,

$$\sigma_{ij} = C_{ijkl}\varepsilon_{kl} \text{ or } \varepsilon_{ij} = S_{ijkl}\sigma_{kl}, \tag{2.1}$$

where *C* is the 4 x 4 stiffness matrix and *S* is the 4 x 4 compliance matrix. When the crystal-axis coordinate system is used for a cubic crystal (Ge and Si), the compliance coefficient matrix is known for the [100], [010] and [001] coordinate system [10], through a transformation [11] the stiffness/compliance matrix can be determined for an arbitrary rectangular system, thus the elastic response of the material can be obtained.

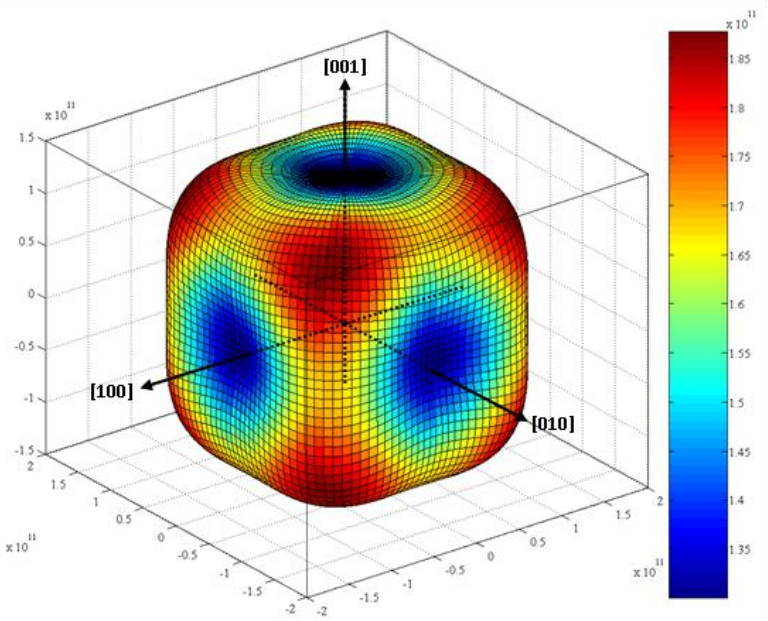

Figure 2.2: Young's modulus as a function of crystallographic orientation (in Pa) [12].

2.1.2 Phase Transformation in Silicon

Silicon crystal has a diamond cubic structure at ambient pressure, but at high pressure the structure can be transformed into other crystalline phases. As many as 12 stable or metastable solid structures of silicon have been observed at different pressure levels. Except for the diamond cubic phase and the Si-IV phase, which are semiconducting, all other phases of Si have metallic conductivity. This section will provide a summary of the different phases of silicon and the transformation behavior reported in literature. Table 2.1 summarize the structures and pressure ranges needed for the formation of each phase [13] .

The high pressure phases of silicon are of interest to this study due to the fact that during wire sawing high contact pressures generated in silicon by the diamond/silicon carbide grits can be large enough to cause phase change, which alters its mechanical

properties. It has been shown that when the cutting depth and tool geometry are controlled, silicon can be machined like a ductile metal [7]. It is generally accepted that ductile cutting of silicon is accompanied by phase transformation from the diamond cubic phase to other phases. Therefore, it is of interest to understand the mechanical properties of different phases of silicon and transformations between them, to aid in the development of a finite element type of model to analyze the fundamental aspects of the wire sawing process.

Table 2.1: Crystalline phases of silicon [13].

Designation	Structure	Space group	Pressure region (GPa)
Si-I	diamond cubic	Fd3m	0–12.5
Si-II	body centred tetragonal (β-Sn)	$I4_1/amd$	8.8–16
Si-III (or BC8)	body centred cubic (basis of 8 atoms)	$Ia\bar{3}$	2.1–0
Si-IV	diamond hexagonal (lonsdaleite)	$P6_3/mmc$	–
Si-V	primitive hexagonal	P6/mmm	14–35
Si-VI	unidentified		34–40
Si-VII	hexagonal close packed	$P6_3/mmc$	40–78.3
Si-VIII	tetragonal (~30 atoms per unit cell)	$P4_12_12$	14.8–0
Si-IX	tetragonal (12 atoms per unit cell)	$P4_22$	12–0
Si-X	face centred cubic	Fm3m	78.3→230
Si-XI (or Imma)	body centred orthorhombic	Imma	13/15
Si-XII (or R8)	trigonal (8 atoms per unit cell)	$R\bar{3}$	12–2.0

With increasing hydrostatic pressure, silicon undergoes various phase transformations. In loading at a pressure of 10–12 GPa [14] the original diamond structure of silicon (Si I) transforms into a denser β-Sn (metallic) phase (Si II), accompanied by a 22% volumetric reduction. A further volumetric decrease of 0.2–0.5% associated with the Imma silicon (Si XI) occurs when the pressure is in the range of 13–16 GPa [15]. More phase changes take place upon further increment of pressure: the primitive hexagonal phase (ph, Si V) forms at 14–16 GPa [14], Cmca (Si VI) forms at above 38 GPa [16] and the

hexagonal close-packed structure (hcp, Si VII) forms at 40-49 GPa [17]. The sequence of high-pressure phase transformations concludes with the face centered cubic silicon phase (fcc, Si X) at around 79 GPa, which is thought to remain stable up to 248 GPa [17].

Upon hydrostatic unloading, the phase change of silicon shows a different process. First, the hexagonal close-packed Si changes to ph Si, and then to β-Sn Si. Upon further unloading, the β-Sn Si phase can undertake several crystalline forms or transform to amorphous Si (a-Si). If crystalline forms are sustained, β-Sn Si changes to a metastable rhombohedral (R8, Si XII) solid structure at 8–10 GPa [18] and to a 1–2% denser body centered cubic silicon phase (bcc, Si III) at 2 GPa [19]. The effect of unloading rate on the phase transformation of Si-II has shown that there exists a critical unloading rate above which there is insufficient time for recrystallization, namely the formation of Si-III or Si-XII phases, and therefore the a-Si phase is formed [20-22].

2.2 Wire Sawing Methods

Although wire sawing has been used for decades to produce semiconductor and PV silicon wafers, research efforts focusing on the topic have been surprisingly limited. Kao et al. [23-30] were one of the first to study the wire sawing system for manufacturing of semiconductor grade Si wafers. Their effort lasted for about a decade and their activities are summarized as shown in Fig 2.3. Their work can be classified into three major aspects: cutting mechanism, material removal rate and saw damage. The yellow modules on the right side of Fig 2.3 present their pertinent work on each aspect.

Li et al. [23] developed a contact stress model of the interactions between the wire, ingot, and abrasives in the multi-wire sawing system (MWSS) process. Abrasives in the

slurry are treated as loose third-body particles caught between the wire and the ingot surface. Material removal is attributed to the simultaneous rolling and indenting action of the abrasives on Si. This is referred to as the rolling-indenting model of material removal. The contact stress induced by a cone-shaped cutting grit was calculated based on superposition of stress fields resulting from the normal and tangential loads applied by the abrasive. It should be noted that their results are only valid for elastic deformation due to application of the linear superposition principle.

Following the rolling-indentation modeling work, the indentation elastic stress fields created in Si by an axisymmetric indenter was solved by Yang and Kao [24]. The elasto-hydrodynamic interactions between the slurry and wire in MWSS were analyzed using the finite element method [25]. The resulting analysis yielded a film thickness profile and pressure distribution as a function of wire speed, slurry viscosity, and slicing conditions. It was shown that slurry-based wire sawing is characterized by "floating" machining conditions where the minimum film thickness is greater than the average abrasive size. In addition to the "rolling-indenting" model, a "scratching-indenting" model was proposed as the cutting mechanism by Yang and Kao [26]. They also proposed a material removal model based on indentation fracture mechanics, which accounts for plastic deformation and cracking of the Si bulk [27, 28].

Bhagavat and Kao [29] presented a finite element model that analyzed temperature variation in the ingot during MWSS. The model uses time-dependent boundary conditions and geometry, which are integral to the slicing process. In addition, a method was proposed to obtain a relatively flat temperature profile during wire sawing via intelligent control of the boundary conditions in order to reduce warp due to heat generated by the process.

Since wire sawing is a dynamic process, Zhu and Kao [30] used Galerkin-based modal analysis to study the vibration characteristics of the wire during sawing. The results of this study suggest that the wire and slurry system dynamics are characterized by real and paired complex eigenvalues, which correspond to the over-damped modes and other vibration modes of the system. The Si material anisotropy was ignored for simplicity in the models proposed by Kao and co-workers.

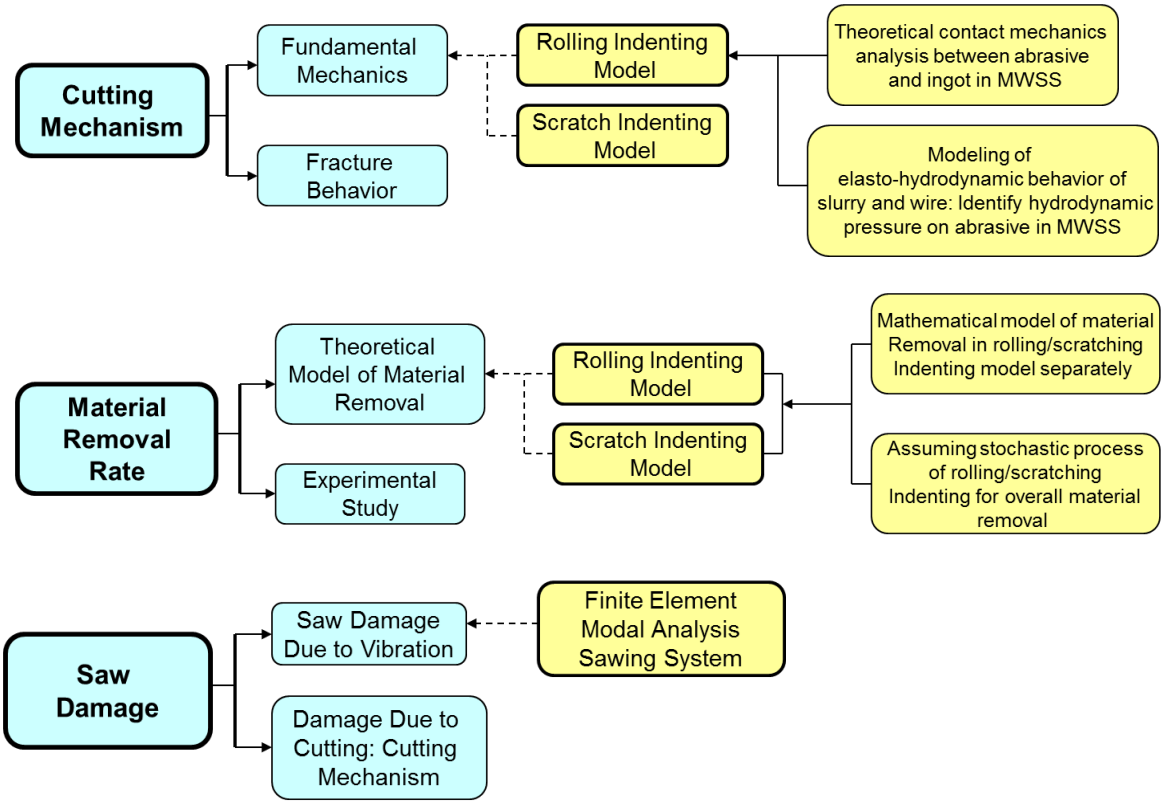

Figure 2.3: Research activities of Kao et al. on wire sawing of semiconductor grade silicon.

Notable work on wire sawing has also been reported by Möller and his co-workers. A 2-dimensional model was proposed to analyze the elasto-hydrodynamic behavior of slurry and wire [31] and a material removal rate model based on indentation fracture mechanics was presented in [31]. Bidiville, et al. [32] studied the surface roughness and

microcrack density of Si wafers cut by MWSS. Recently, Bierwisch, et al. [33] developed a model to study the sawing contact regime using dissipative particle dynamics and discrete element simulations for modeling a suspension of the fluid and abrasive. Zhao, et al. [34] applied a PDE-constrained Gaussian process model to evaluate the change in material removal rate over time. Fig 2.4 shows the variation in silicon wafer thickness due to the dynamically varying material removal rate. Liedke and Kuna [35] presented an analytical model for the macroscopic mechanical conditions in the MWSS process. Based on experimental results, the model described the influence of important process parameters such as wire velocity, feed velocity, and wire tension, as well as geometric parameters such as ingot size and wire length, on the lapping pressure and wire bow.

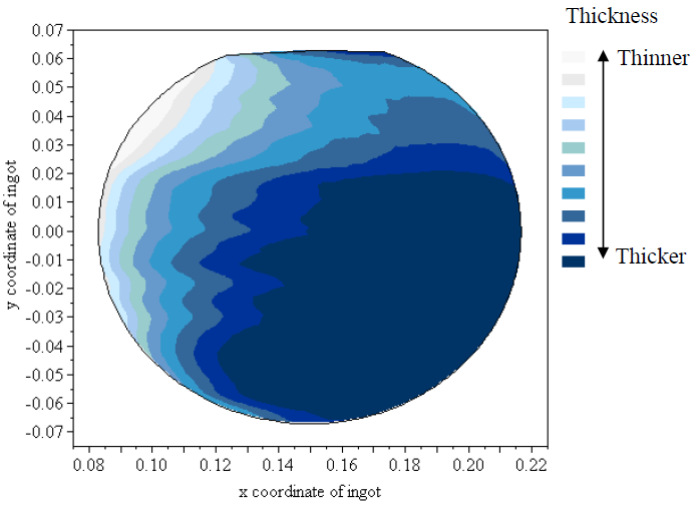

Figure 2.4: Si wafer thickness non-uniformity due to varying material removal rate [34].

2.3 Single Grit Scribing of Si and Other Brittle Materials

In abrasive machining processes such as grinding, polishing, lapping, wire sawing, material removal is achieved by the simultaneous actions of many cutting grits. In order to

understand the fundamental cutting performance, a study of single grit scribing is typically used to investigate the influence of various cutting parameters. In this section, previous studies on single grit scribing of brittle materials, including silicon, are summarized.

2.3.1 Cutting Mode and Effect of Cutting Conditions

Although silicon is brittle at room temperature, it exhibits ductile behavior when cut at low feed rates. A number of studies on ductile mode cutting of Si have been reported [7, 36-44]. Fig 2.5 presents an example of ductile mode diamond turning of silicon. It is widely believed that ductile behavior of Si is due to the transformation of the diamond cubic phase of Si to a metallic (β-Sn) phase under high contact pressures [36-44]. A Transmission Electron Microscope (TEM) image of the amorphous silicon (a-Si) layer on a ductile cut silicon surface and Raman spectroscopy analysis of the a-Si phase are shown in Fig 2.6 [39]. The critical depth of cut is defined as the cutting depth below which ductile mode of cutting is obtained. Cutting experiments on single crystal semiconductor grade Si indicate that the critical depth of cut varies with the cutting tool edge radius [36-38]. As shown in Fig 2.7, it has been found that the following conditions must be satisfied in order to achieve ductile cutting: (1) the cutting tool edge radius r should be less than a critical limit, and (2) the undeformed chip thickness must be smaller than the tool edge radius ($a_c < a_0$) [36]. Note that to date ductile-to-brittle transition studies using scribing have only been carried out on single crystal Si. However, due to the presence of grain boundaries, twin boundaries and impurities, the cutting modetransition in multicrystalline Si is more complicated and requires further study.

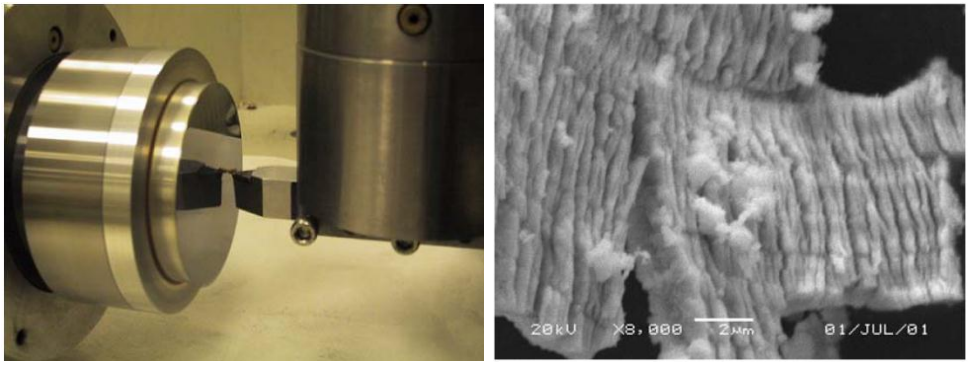

Figure 2.5: Diamond turning of semiconductor grade silicon and the ductile debris generated [36].

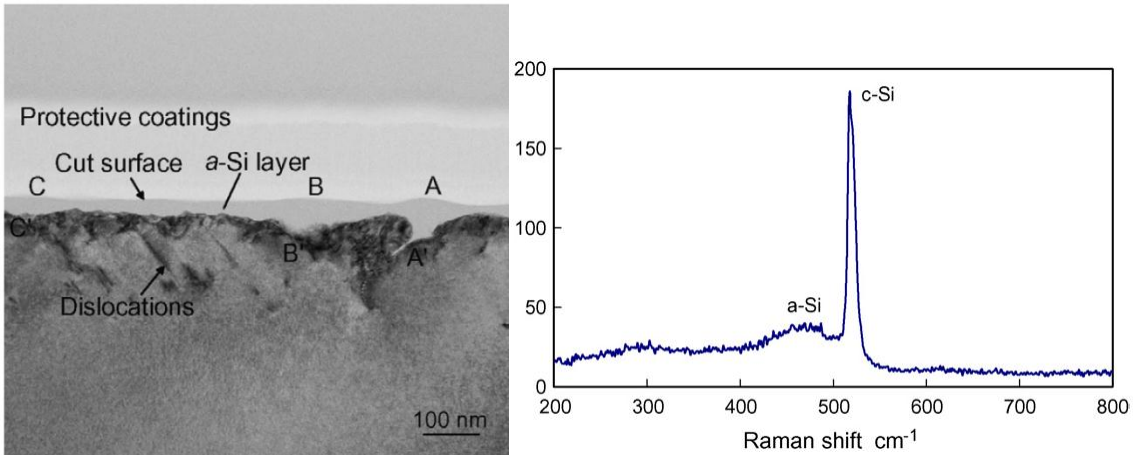

(a) (b)

Figure 2.6: TEM (a) and Raman spectroscopy (b) study of ductile mode turning of silicon [39].

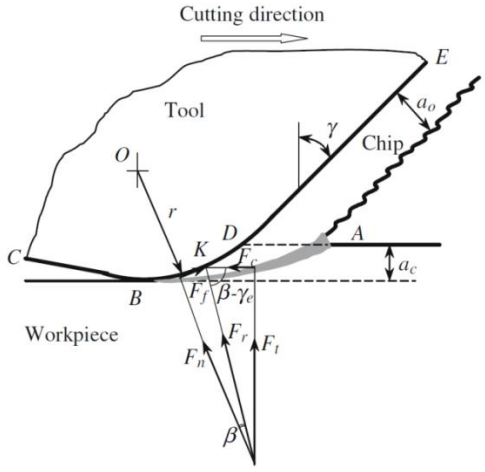

Figure 2.7: Schematic of ductile mode turning of silicon [36].

2.3.2 Effect of Material Anisotropy on Cutting Modes

Since single crystal (or mono) Si is anisotropic, researchers have studied the effects of crystallographic orientation on ductile cutting of this material [41, 45-48]. Shibata, et al. [41] reported results of diamond turning experiments carried out on (111) and (001) crystal planes of at cutting depths of 100 nm and 1μm. A slip orientation factor was proposed to explain the varying degrees of ductile mode cutting observed in different crystallographic orientations. However, this factor alone cannot explain the observations when scribing at a cutting depth of 1 μm. Moreover, their explanation does not take into account the phase transformation of Si, which is believed to accompany ductile mode cutting [44]. Similar observations were also reported in [45-48] when machining (turning) (111) and (001) c-Si. Fig 2.8 shows the critical depth variation of ductile-to-brittle cutting mode transition as a function of crystallographic orientation in single crystal silicon (111) plane. However, no detailed scientific explanations for the observations were given.

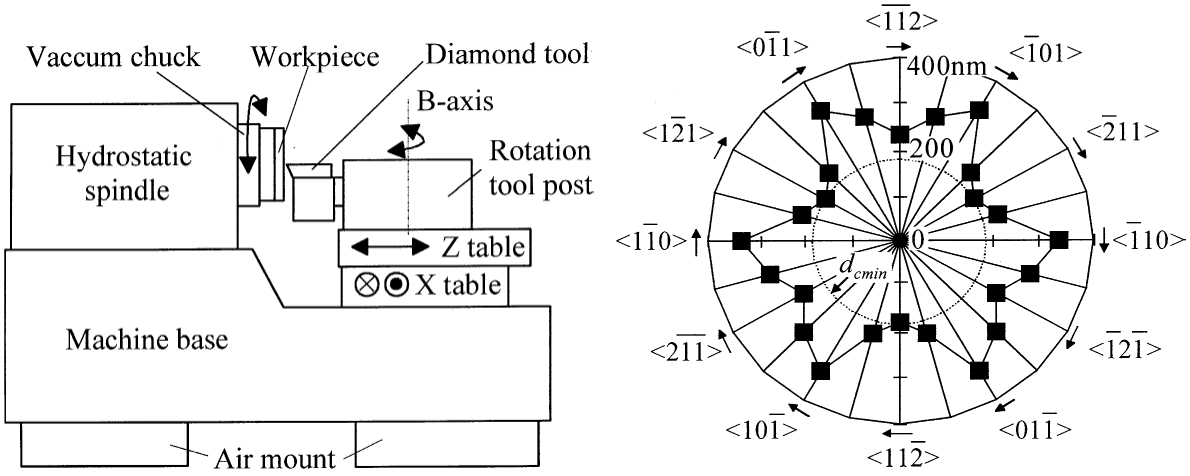

Figure 2.8: Experimental setup for study of silicon cutting mode transition and the critical depth in Si (111) [46].

2.3.3 Material Removal Modeling

The indentation fracture mechanics approach is widely used to model the material removal process during brittle cutting due to similarities of the generated crack systems. The typical model for the deformation pattern and resulting crack systems in indentation of a brittle material are shown in Fig. 2.9. There is a zone of plastic deformation directly under the indenter. Two principal crack systems, namely median/radial and lateral cracks, emerge from the plastic zone [27-28]. This model was originally developed for static loading in pure indentation and was subsequently extended to include the effects of tangential load in scribing processes [49].

The lateral fracture model has been applied to analyze material removal in the scribing/lapping process [50-52]. Material removal is assumed to occur when lateral cracks propagate to the surface. The lateral crack size can be expressed as [28]:

$$c_l = c^L[1-(P_0/P)^{1/4}]^{1/2} \tag{2.2}$$

where,

$$P_0 = \zeta_0(\cot\psi)^{-2/3}(K_c^4/H^3)(E/H),\ c^L = [\zeta_L(\cot\psi)^{5/6}(K_cH)E^{3/4}]^{1/2}P^{5/8} \tag{2.3}$$

ξ_0, ξ_L are constants, P is the normal load, and 2ψ is the included angle of the indenter/scriber. Then, for a total scribing length, l, the volumetric removal is given by [59]:

$$V_l = \alpha(P^{9/8}/K_c^{1/2}H^{5/8})(E/H)^{4/5}l \tag{2.4}$$

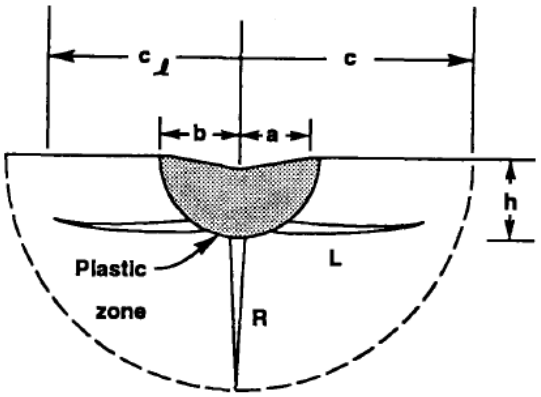

Figure 2.9: Plastic zone, median/radian (R) and lateral cracks (L) for indentation [27-28].

While this expression correlates well with results obtained in lapping of brittle materials such as glass [51, 52], the model cannot be satisfactorily validated for cutting of single/polycrystalline ceramic materials [53-55]. Other material removal models for fracture behavior have also been proposed [56, 57]. The model proposed by Moore and King [56] takes into account both ductile and brittle modes of cutting. The model by Xu and Jahanmir [57] relates the volume removed to grain size, hardness, and fracture toughness. While these models are purported to be generally applicable to all brittle materials, their applicability to silicon scribing has not been established. It is anticipated that phase transformation of Si can complicate the material removal mechanism and potentially render the brittle fracture based models inadequate.

2.3.4 Subsurface Damage Modeling

A large number of researchers have conducted studies to evaluate subsurface damage generated in scribing of brittle materials. Partial cone cracks produced in elastic solids by a sliding spherical indenter were investigated by Lawn [58]. The failure process in elastic-plastic contact (sharp indenter) under tangential loading was studied by Swain

[59]. Bower and Fleck [60] proposed a 2-dimensional fracture model to investigate crack propagation in an elastic stress field generated by a line contact. Jing et al. [61] assumed a sliding blister field model and an expanding cylindrical cavity model to analyze the stress fields produced in scribing, as shown in Fig 2.10. The inelastic and fracture zone size can be determined from the stress distribution, respectively. However, the validity of the blister field model and the expanding cylindrical cavity model has not been verified. Zhang and Subhash developed a Finite Element Modeling (FEM) approach to estimate the damage zone size by Vickers indentation and scratching [62, 63]. Fig 2.11 presents the damage contour map after an indentation. The model employed the crack opening displacement (COD) principle to empirically determine the degradation of modulus during dynamic crack propagation. The validity of the COD principle was not verified and the study was limited to Vickers scriber geometry.

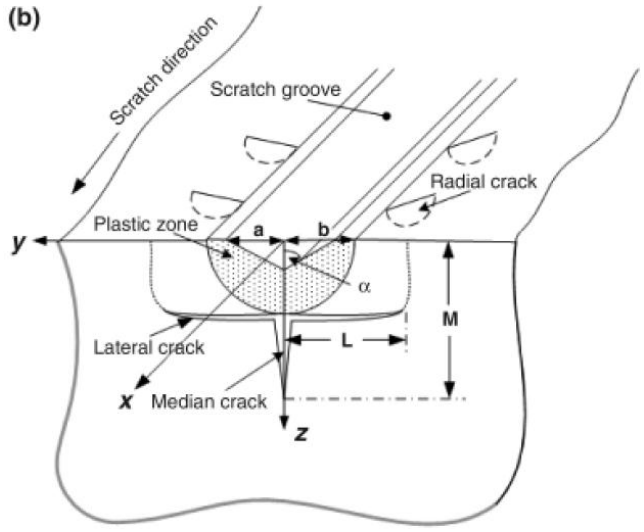

Figure 2.10: Theoretical model for predicting plastic and damage zone size by Jing et al. [61].

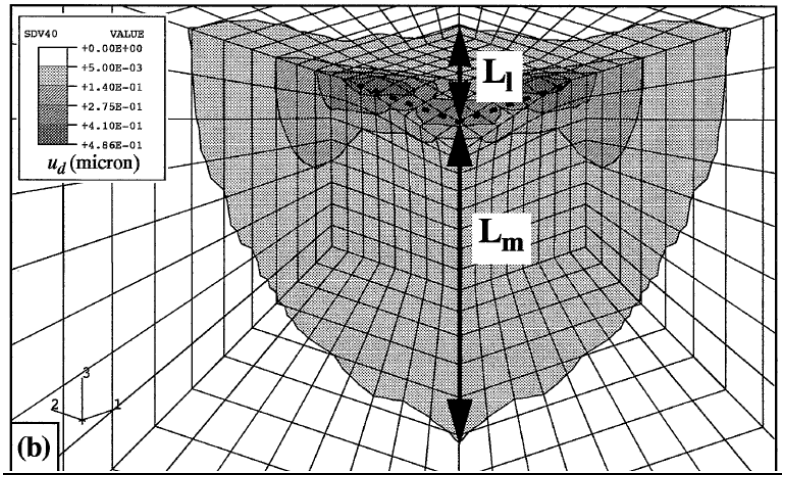

Figure 2.11: Damage contour map prediction of an indentation, by Zhang and Subhash [63].

2.3.5 Effects of Cutting Fluid

It was reported that cutting fluid significantly influences the cutting morphology in single grit diamond scribing of silicon [64]. As shown in Fig 2.12, silicon is more chipped in water, and demonstrates more ductile mode of cutting in ethanol and acetone. Li, et al. [65] experimentally studied the effect of cutting fluid on phase transformation of diamond cubic Si (Si-I) to amorphous silicon (a-Si). It was shown that a lubricant with high viscosity and a weak hydrogen bond facilitates the phase transformation of Si. The influence of polyethylene glycol and/or water-based cutting fluids used in the wire sawing process on the material removal mode still needs scientific investigation.

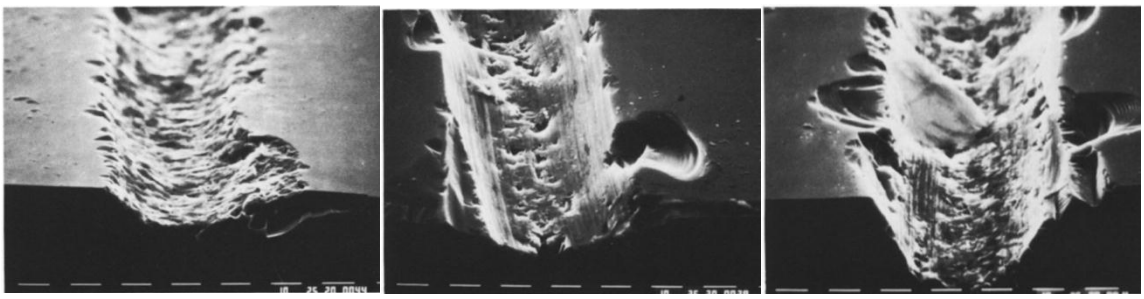

(a) (b) (c)

Figure 2.12: Morphology of silicon scribed in wafer (a), ethanol (b) and acetone (c), by Scott and Danyluk [64].

2.4 Hard Inclusions in Multicrystalline Silicon

More than 80% of mc-Si is grown by either the Bridgman method or related ingot production techniques [66]. The direct purification of metallurgical silicon through melt and solidification processes yields less pure silicon feedstock [66]. In the case of supersaturation of carbon and nitrogen, SiC and Si_3N_4 inclusions form in the mc-Si ingot during solidification. SiC and Si_3N_4 inclusions in mc-Si were first reported by Søiland et al. [67]. Hari Rao, et al. [68] showed that SiC inclusions in edge-defined, film-fed grown (EFG) Si adversely affect the performance of solar cells. However, limited studies of the detrimental effects of these inclusions on wafer sawing have been reported. Du, et al. [8, 69, 70] showed that some SiC particles have smooth surfaces after slurry sawing while others do not (see Fig. 2.13). The smooth surfaces result from mechanical grinding of the SiC powder during sawing. The fact that some SiC particles are not ground or do not possess a smooth surface may suggest that these SiC particles have a higher hardness or have more wear-resistant properties than ground SiC particles. As a result, the wire most likely climbs over the SiC particles without grinding them, which results in the formation

of the ridges seen in Fig. 2.13. It was also shown that the Si_3N_4 particles are not associated with a sawing ridge, suggesting that Si_3N_4 does not play a significant role in the formation of ridges due to its lower hardness than the SiC particles in the cutting slurry.

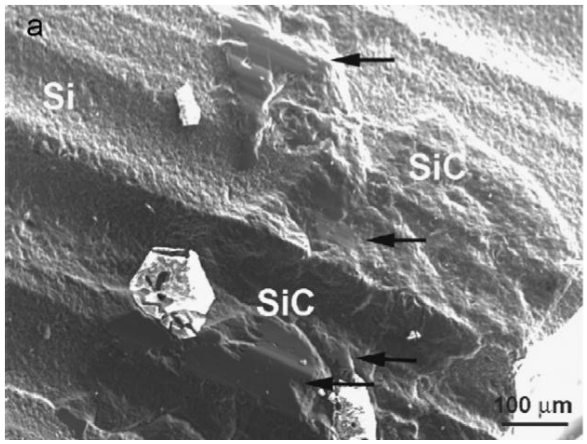

Figure 2.13: SEM images of sawing ridges. Black arrows indicate the ground surfaces of SiC particles (after Du, et al. [8]).

Although the surface morphology resulting from interaction of a cutting grit and a hard inclusion has been studied, the mechanism of interaction is not well understood. Consequently, further study of this interaction is necessary to better understand the role of hard carbide and nitride inclusions on material removal and surface damage induced in wire sawing processes.

2.5 Effects of Dislocation on Mechanical Properties of Silicon

Unlike c-Si materials, mc-Si has a higher density of defects and impurities [1, 66]. As a major type of crystal defect, dislocation clusters are widely known as recombination centers and therefore negatively impact solar cell efficiency [71-72]. While its detrimental effect on electrical properties of silicon are well understood, the influence of dislocations

on the mechanical properties and the resultant cutting performance of mc-Si during wafering are still not clear.

At temperatures above the brittle-to-ductile transition of crystalline silicon [73], it was found that interstitial oxygen and nitrogen atoms can cause the locking of dislocations, which increases the strength of the silicon crystal [74-76]. In addition, crack tip shielding can be induced by crack tip dislocation multiplication in the same temperature range [77-79]. It has been known that dislocations can also be generated in crystalline Si at room temperature under extreme loading conditions such as indentation and scribing [41-44, 80]. Evidence has shown that dislocation plasticity without phase transformation can be generated by nanoindentaition at room temperature [81].

Wire sawing of silicon wafers typically does not involve very high temperatures. Therefore, an understanding of the influence of dislocations on the mechanical properties of mc-Si at room temperature is necessary in order to shed light on its behavior during indentation and scribing processes.

2.6 Summary and Research Questions of This Dissertation

Based on the literature review, it is clear that there is still insufficient understanding of the effects of anisotropic material properties of single crystal Si, abrasive or cutting grit shape and frictional conditions on the ductile-to-brittle transition in cutting of PV Si materials. In addition, there is lack of systematic scientific investigations of the advantages and disadvantages of slurry wire sawing and diamond wire sawing in terms of their mechanical strength and wafer surface quality. Moreover, the influence of hard inclusions

and dislocation clusters on the wire sawing performance of mc-Si has not been systematically investigated. These aspects are addressed in this thesis.

CHAPTER 3

ANALYSIS OF SLURRY AND FIXED ABRASIVE DIAMOND WIRE SAWN SILICON WAFERS

This chapter presents an analysis of slurry and fixed abrasive diamond wire sawn silicon wafers. Various metrological and mechanical characteristics of silicon wafers sliced by slurry and fixed abrasive diamond wire sawing are analyzed through measurements. The analysis of the characteristics of the wafers sawn by both the techniques can not only shed light on the sawing mechanisms in those two techniques, but also provide a comparison of the two techniques in term of the quality of the wafers produced. In general, diamond cut wafers are found to have comparable characteristics as slurry cut wafers, which indicates that fixed abrasive diamond wire sawing may be a viable alternative to slurry wire sawing.

3.1 Introduction

The objective of this study is to quantitatively analyze and compare the characteristics of silicon wafers sliced by the two techniques. As-cut 156mm square cast polycrystalline Si wafers produced by the two sawing techniques were provided by two industrial vendors (denoted as A and B) and are summarized in Table 3.1. The surface morphology, cutting mode (ductile/brittle), thickness variation, surface roughness, surface profile, and residual stresses of the Si wafers are examined. Due to their considerable importance in the solar cell production process, microcrack and fracture strength of silicon wafers produced by the two techniques are analyzed in depth.

Table 3.1. Si wafers used in this study.

Vendor A			Vendor B	
Diamond cut (VAD)	Slurry cut group 1 (VAS1)	Slurry cut group 2 (VAS2)	Diamond cut (VBD)	Slurry cut (VBS)
200 µm thick	160 µm thick *F600 cutting grit	160-200 µm thick *F800 cutting grit	200 µm thick	200 µm thick

***** F600 and F800 are the powder size specifications from the Federation of European Producers of Abrasives (FEPA), the mean grain size are 9.3±1 µm and 6.5±1 µm, respectively.

3.2 Experimental Methods

The surface morphology of silicon wafer surface is characterized using Scanning Electron Microscope (SEM, Hitachi VP-S3700). The phase change of crystalline Si is studied using Raman spectroscopy. Raman spectroscopy is widely used to characterize the appearance of different phases of c-Si [43, 82]. The technique relies on the analysis of Raman scattering of monochromatic light from a laser. The photons emitted by the laser interact with molecular vibrations of the sample, resulting in photon energy being shifted up or down. The shift in energy gives information about the vibration modes and thereby the chemical composition of the sample [83]. Different phases of crystalline Si have corresponding peaks in Raman spectra. The surface roughness is measured using an optical interferometer (Zygo). The back and front wafer surface profiles were measured using a Taylor Hobson Talysurf® profilometer along a 100mm track perpendicular to the saw marks in the wafer center. The maximum in-plane shear residual stresses are analyzed using a near-infrared circular polariscope. The six-step phase stepping method proposed by Patterson and Wang [84] was used to solve for the phase retardation and isoclinic angle of the infrared light passing through the sample, which were then used to calculate the maximum shear stress $\boldsymbol{\tau_{max}}$ via the stress-optic law [85]. The microcracks are identified through Chemical Mechanical Polishing (CMP) and their geometric

characteristics are measured using an optical microscope (Keyence VHX-60). The fracture strength of silicon wafers are studied by both four line and biaxial bending tests.

3.3 Results

3.3.1 Surface Morphology and Cutting Mode

It has been shown that slurry cut wafers typically exhibit a rough surface with random texture [86], as seen in Fig. 3.1(a) whereas diamond cut wafers typically have smooth cutting grooves or saw marks in the cutting velocity direction, and as seen in Fig.3.1(b), there is also some brittle chipping along the smooth cutting traces. It is known that diamond cubic silicon, when subjected to very high pressures (>8GPa), undergoes phase transformation resulting in new crystalline phases (e.g. Si-III, Si-XII) at low unloading rates, or amorphous silicon at high unloading rates [20-22, 82]. It is believed that the ductile cutting mode of silicon is due to formation of the amorphous phase [36-48]. The Raman spectra in Fig. 3.2 clearly show the presence of amorphous silicon in the smooth cutting grooves of the diamond cut wafer. In general, amorphous Si is observed in the ductile cutting regions of diamond cut wafers while it is rarely observed in slurry cut wafers, whose surfaces mostly exhibit the crystalline diamond cubic phase. The presence of amorphous Si in diamond cut wafers is consistent with the literature report.

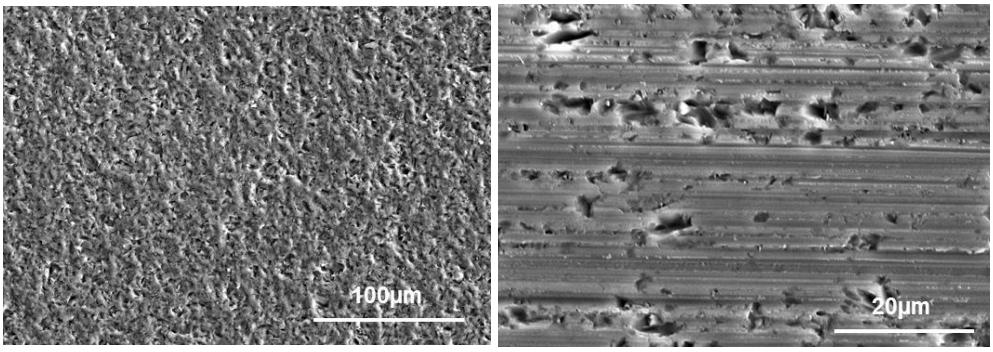

(a) (b)

Figure 3.1: SEM image of wafer surface: slurry cut (a), diamond cut (b).

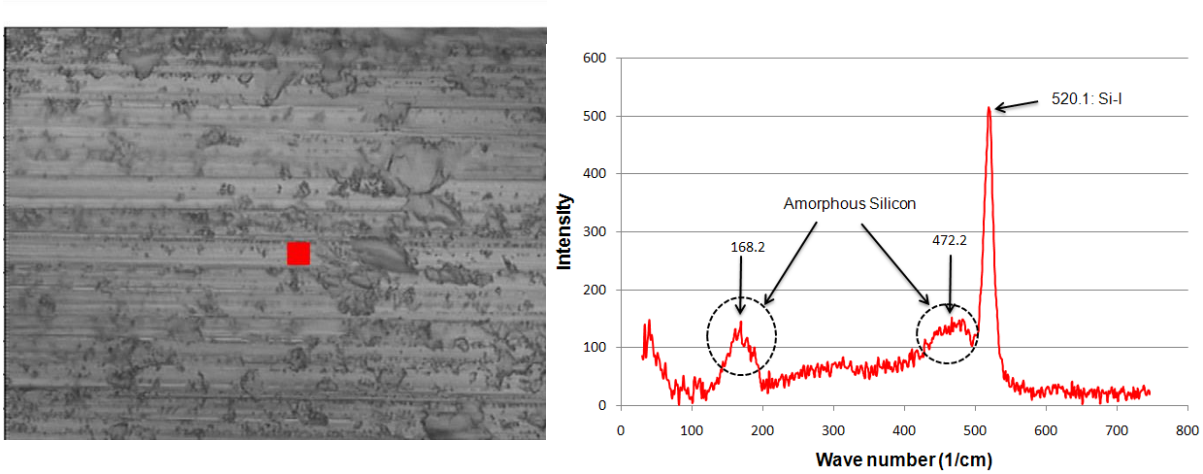

(a) (b)

Figure 3.2: Appearance of a-Si in diamond cut silicon wafer: Raman spectra (b) of marked region in (a).

3.3.2 Thickness Variation

The thickness of slurry cut wafers was observed to vary as a function of location in the wafer. Specifically, along the wire speed direction (see Fig. 3.3(a)) the right edge (T2,T4) is generally thicker than the left edge (T1,T3), and along the wire feed direction the bottom edge (T3,T4) is thicker than the top edge (T1,T2). The thickness variation as a function of wafer location is shown in Fig. 3.3(b). The thickness variation pattern

identified in this study agrees with literature report [32]. In contrast, the diamond cut wafers showed random thickness variation of about 20µm.

3.3.3 Surface Roughness

Fig. 3.4 shows the surface roughness variation along the wire speed direction measured using the optical interferometer. The roughness of slurry cut wafers decreases significantly from wire entry (left edge) to exit (right edge). However, the roughness remains nearly constant along the wire feed direction. Representative surface roughness measurements perpendicular to the saw marks along the center lines of the Vendor B wafer surface are shown in Fig. 3.5. Bidville et al. [32, 86] also reported the same surface roughness patterns in slurry cut wafers. In contrast, the measured roughness of the diamond cut wafers appears to depend on local cutting conditions and can have large random variations, especially when measured along the wire speed direction.

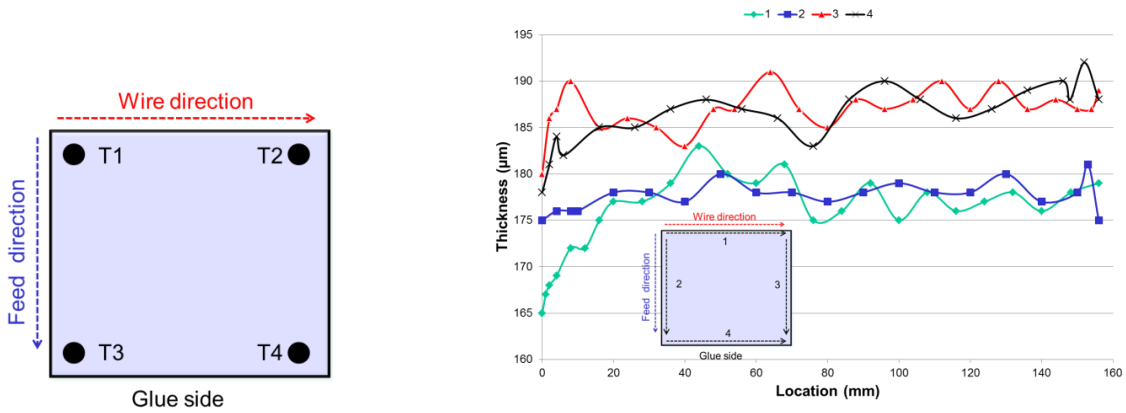

(a) (b)

Figure 3.3: Slurry cut wafer cutting schematic (a) and thickness variation (b).

3.3.4 Surface Profile

Representative profiles of slurry and diamond cut wafers are shown in Fig. 3.6. Note that the surface profiles are plotted such that the difference between the back and

front surface profiles represents the thickness variation. It can be seen that diamond cut wafers generally have a larger surface profile variation. There appears to be a strong correlation between the profile variation between the back and front surfaces of both slurry and diamond cut wafers. This may be due to the synchronous displacement of the ganged cutting wires. Note also that slurry cut wafers exhibit smaller thickness variation than diamond cut wafers.

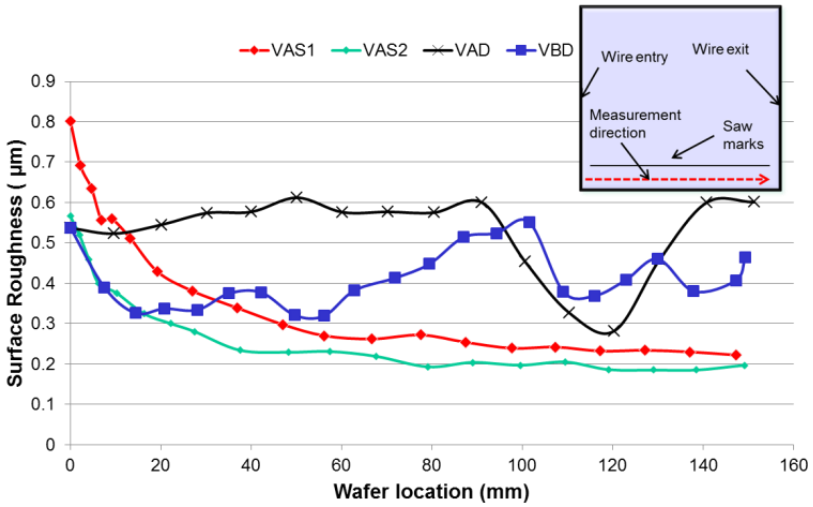

Figure 3.4: Surface roughness as a function of location along saw marks.

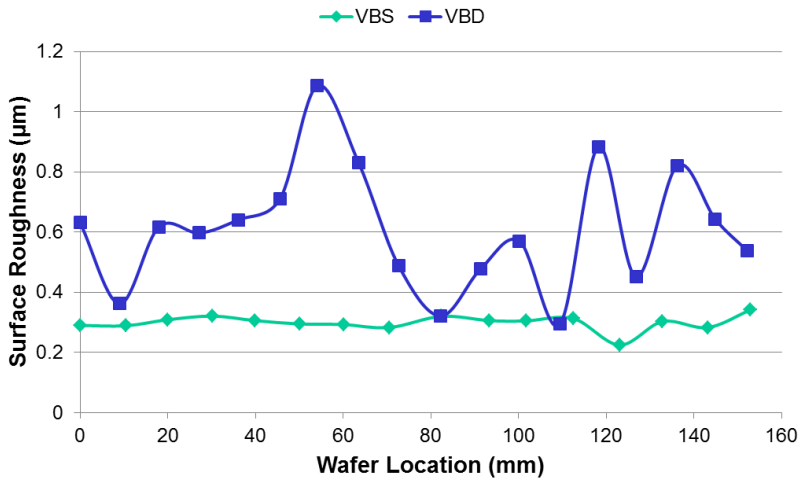

Figure 3.5: Surface roughness perpendicular to the saw marks along the wafer surface center line.

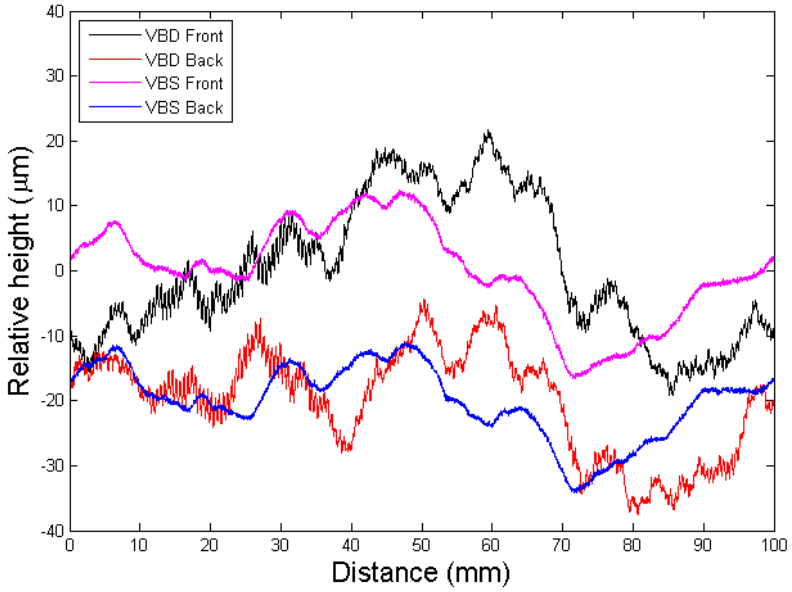

Figure 3.6: Surface profile measurement.

3.2.5 Residual Stress

The maximum in-plane shear residual stresses in the wafers from the each group provided by Vendor A were analyzed. The average maximum shear stresses for wafer groups VAS1 and VAS2 were observed to be in the range 1.5 – 3.3 MPa, whereas the VAD group yielded an average value of 2.4 MPa (see Fig. 3.7). The diamond cut wafers reveal a noticeable vertical stress pattern along the wire feed direction.

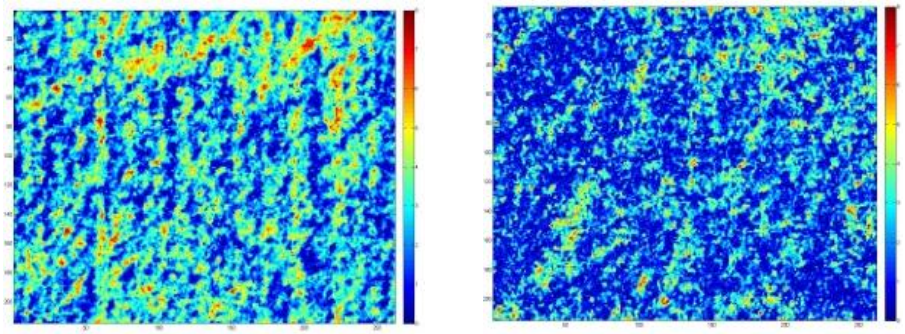

Figure 3.7: τ_{max} in VAD wafer (left) and VAS2 wafer (right); each figure represents a 225 mm^2 section of the wafer.

3.3.6 Microcracks and Fracture Strength

The mechanical integrity of the Si wafers is of considerable importance in the solar cell production process since fracture during processing can raise the costs significantly. Si is a brittle material and its breakage occurs by elastic fracture [87]. With increasing use of thinner wafers to lower material costs [88], wafer breakage due to fracture during handling and processing of solar cells is a major issue.

Wafer breakage is believed to be related to microcracks created in the sawing operation. However, there are few studies that discuss the mechanical characteristics of diamond cut wafers relative to slurry cut wafers. The objective here was to compare the mechanical strengths of multicrystalline silicon wafers cut by both loose abrasive slurry and diamond wire sawing methods and evaluate the differences in wafer strengths obtained using two different wafer bending tests, namely, four line bending and biaxial flexure.

Fundamentally, breakage of Si wafers is due to the presence of microcracks in the wafer and applied stresses arising from wafer handling/processing operations that exceed a critical value necessary for wafer failure [89]. Knowledge of the microcrack population, location and geometry as well as distribution of the applied stresses is required to predict and/or prevent wafer breakage. It is believed that microcracks extend from the wafer surface into the material and have a typical length of up to 10-15 μm while edge cracks are usually longer [1]. However, no statistical measurement of crack lengths exists to prove/disprove the foregoing belief. Monte Carlo simulation was employed by Rupnowski and Sopori [90] to investigate the fracture strength of Si wafers with surface, edge and bulk flaws under uniaxial tensile loading. However, the actual stress state

during wafer/cell processing and handling is more complex than uniaxial tension. Additionally, there are nonlinear effects arising from large wafer deflection, especially for thin wafers, that impact the stress state and hence wafer fracture.

In order to avoid the complexity in stress analysis, Si wafer strength is typically evaluated by standard bending tests [91]. Four-line bending, which generates uniform stresses in the wafer between the lines of load application, is sensitive to edge cracks because it is usually the longer cracks at the wafer edge that lead to breakage. The biaxial flexure strength test eliminates the influence of edge cracks by producing the largest stress in the wafer center while the edges are almost stress free. Therefore, wafer breakage in the biaxial test results mainly from the propagation of cracks in the wafer center.

In this section, four line bending and biaxial flexure tests are used to evaluate the strength of multicrystalline Si wafers produced by loose abrasive slurry and fixed abrasive diamond wire sawing processes, as well as to establish the effect of edge cracks (in the four line bending test) and center cracks (in the biaxial bending test) on the mechanical strength of similarly cut wafers. In order to achieve this goal, the typical statistics of microcracks generated by the two wafer cutting processes are established through measurement.

3.2.6.1 Measurements of Microcracks

Knowledge of microcrack density, length and geometry is essential for evaluating the wafer strength. In this study, microcracks at the wafer edge and subsurface cracks in the wafer center were measured under an optical microscope after polishing of the wafer cross section. Specifically, a small portion of the wafer edge of interest was polished to

observe the edge cracks. For center cracks, a small portion of the center of the Si wafer was cut and used. The piece of Si containing the region of interest (wafer edge or center) was sandwiched between two rigid PVC blocks that serve as a fixture during polishing. The sandwiched wafer edge and PVC block assembly was then polished on a Logitech® PM5 polisher using colloidal silica suspension of 60 nm nominal grit size. The silica grits are so small that no micrometer length scale microcracks can be generated by them in the wafer. Polishing was carried out till microcracks in the polished cross section were observed when viewed in a Keyence® VHX-600 digital optical microscope. A representative image of the polished surface of the wafer edge indicating edge cracks is shown in Fig. 3.8.

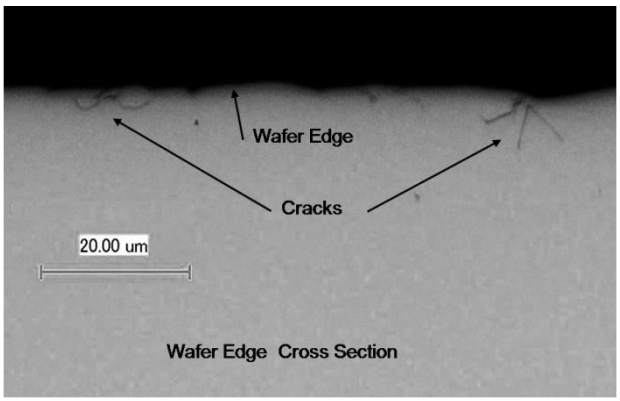

Figure 3.8: Edge cracks in VAD wafer.

Edges of wafers of each type were polished using the procedure described above and the number of cracks in a fixed length of the wafer edge were counted and their lengths measured. At least 200 cracks were counted in each case thereby yielding a sufficiently large sample size for statistical analysis. Microcracks less than 1 μm in length were not counted as they were assumed not to play a major role in determining the wafer fracture strength. The distribution of crack length *L* thus obtained was fitted to the Weibull distribution [92] as follows:

$$L(l) = \frac{k}{\lambda}\left(\frac{l}{\lambda}\right)^{k-1} e^{-(l/\lambda)^k} \tag{3.1}$$

where l is the measured crack length, k is the shape parameter and λ is the scale parameter. Fig. 3.9 shows a comparison of the fitted crack length distribution and the measured crack length data for VBS wafers.

The Weibull distribution has an expected value (or mean) given by

$$E(l) = \frac{1}{\lambda}\Gamma\left(1+\frac{1}{k}\right) \tag{3.2}$$

and a variance given by

$$Var(l) = \frac{1}{\lambda^2}\left\{\Gamma\left(1+\frac{2}{k}\right) - \Gamma\left(1+\frac{1}{k}\right)^2\right\} \tag{3.3}$$

where Γ() is the gamma function. The crack length measurements and data fitting were carried out for both slurry cut and diamond cut wafers and the results are summarized in Table 3.2.

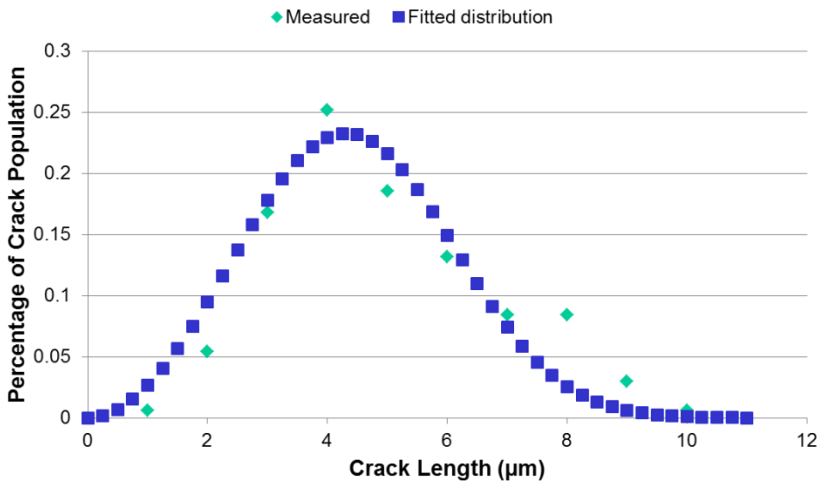

Figure 3.9: Representative fit of the Weibull distribution to the measured crack lengths for VBS wafers.

In the table, crack density refers to the number of microcracks per millimeter of wafer edge. It can be seen that the crack density in diamond cut wafers is about twice that in slurry cut wafers, while the expected crack length for diamond cut wafers is smaller than for slurry cut wafers. Since longer cracks are more likely to cause wafer breakage, the maximum crack length is also listed for comparison. Note that the maximum crack length does not represent the maximum crack length in the entire wafer but only in the section of the wafer edge analyzed.

Table 3.2: Wafer edge crack measurement summary.

	VAD	VBD	VAS1	VAS2	VBS
Crack Density (/mm/edge)	19.0	21.4	7.7	6.7	11.5
Max Length (μm)	8.5	6.3	10.3	7.8	9.7
Expected Length (μm)	3.0	2.5	4.8	3.3	4.4
Standard Deviation (μm)	1.2	1.0	2.2	1.0	1.6

Microcracks in the wafer center were also measured. Wafers were cut through the center, and the edges produced were polished as before to reveal subsurface microcracks. These results are summarized in Table 3.3.

Table 3.3: Wafer center crack measurement summary.

	VAD	VBD	VAS1	VAS2	VBS
Crack Density (/mm/edge)	15.0	17.3	6.6	4.9	8.9
Max. Length (μm)	5.0	5.4	5.6	5.3	5.5
Expected Length (μm)	2.2	2.2	3.1	2.4	3.0
Standard Deviation (μm)	0.7	0.7	0.8	0.9	1.0

It can be seen from the two tables that the crack density and the expected length of center cracks are smaller than for edge cracks. This may be due to the different geometric boundary conditions present during sawing of the wafer edges compared to sawing of the wafer center. Moreover, before wire sawing, the multicrystalline Si ingots

are ground, which can also induce microcracks in the wafer edges. Note that diamond cut wafers have larger crack density and shorter expected crack length than the slurry cut wafers.

3.2.6.2 Wafer Strength Evaluation

The fracture strength of wafers produced by the two sawing processes was evaluated using four line bending and biaxial flexure tests. Schematics of the test setups used for the two bending tests are shown in Fig. 3.10.

Four line bending

Four line bending generates the maximum stress on the back surface of the sample in the region between the two load application lines. Because the edge crack length is greater than the length of cracks in the wafer center, an edge crack propagates at a lower stress level and consequently the four line bending test is ideal for studying the effects of edge cracks on fracture strength [91, 93]. The small-strain linear elastic theory, which is commonly used in the literature, gives the maximum tensile stress generated in the wafer during four line bending as:

$$\sigma_m = \frac{3F(L-l)}{2dt^2} \tag{3.4}$$

where t is the wafer thickness, F is the applied load, and d and L are as indicated in Fig. 3.10. However, it is observed that the deflection of Si wafers prior to breakage can be in excess of 10 mm. The large elastic deformation of the wafer invalidates the small-strain linear elastic theory and necessitates the use of nonlinear large strain elastic theory to accurately determine the applied stresses.

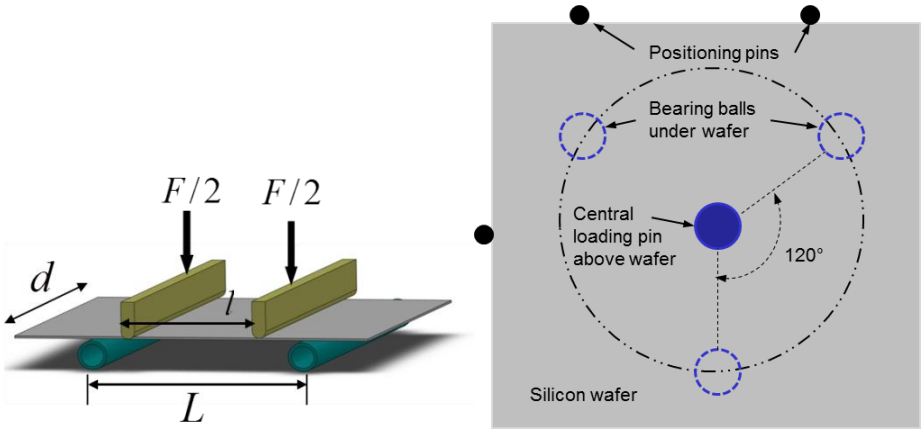

Figure 3.10: Schematics of the four line (left) and biaxial bending (right) tests.

Fig. 3.11 shows a comparison of the maximum tensile stress calculated using the small-strain linear model in Eq. (3.4) and a large strain model solved using the finite element method (FEM). It can be seen that as the applied force increases, the resultant nonlinearity can lead to stress discrepancies as large as 50 MPa. Therefore, nonlinear FEM models are used in this study to analyze the fracture strength.

The typical maximum principal stress distribution in the wafer computed using the nonlinear model is shown in Fig. 3.12. As expected, large tensile stresses are generated between the two lines of load application. Due to the large deflection and contact between the loading lines and the wafer, the edges of the wafer experience the largest stress, thereby increasing the probability of wafer failure due to propagation of edge cracks. It can also be seen that stresses directly below the loading lines are slightly larger (<5 MPa) than in the wafer center.

As noted earlier, wafer breakage occurs due to the existence of microcracks and applied stresses that exceed a critical limit. According to Linear Elastic Fracture

Mechanics (LEFM), a crack will propagate if the stress intensity factor exceeds the fracture toughness of the material [94]:

$$K_{(I,II)} = Y\sigma\sqrt{\pi a} \geq K_{(I,II)c} \tag{3.5}$$

where σ is the applied stress, a is the crack length and Y is a dimensionless constant that depends on the crack geometry and loading mode; K_I and K_{II} are the stress intensity factors for mode I (crack opening mode) and mode II (in-plane shear mode) failure. Note that for thin Si wafers the out-of-plane stress is negligible and therefore mode III failure (out-of-plane shear) is not considered.

It is evident from Eq. (3.5) that crack length plays a significant role in determining fracture strength. Meanwhile, the geometry/orientation of the cracks determines Y, which has a significant effect when both fracture modes are in effect as discussed in the following.

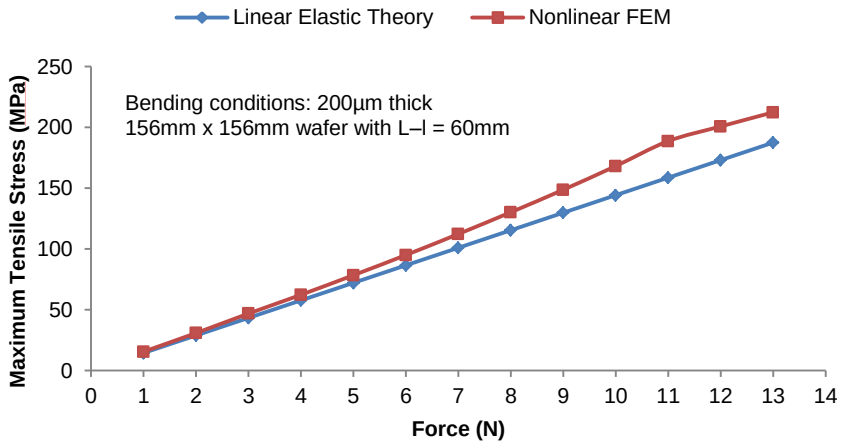

Figure 3.11: Comparison of linear and nonlinear elastic models for calculating the tensile stress produced in the wafer.

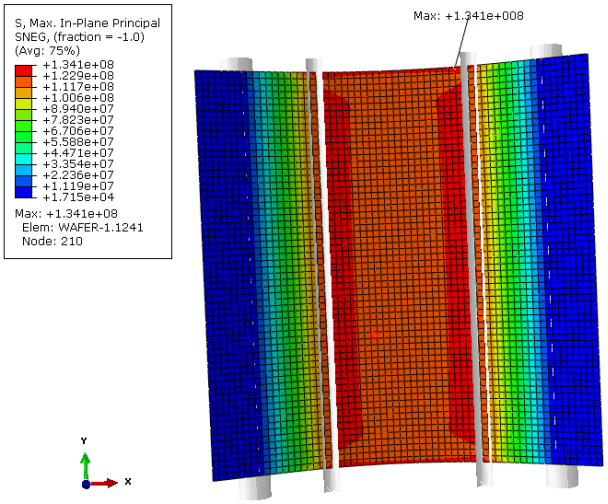

Figure 3.12: Maximum principal stress distribution in four line bending.

Since the length of the microcrack is much smaller than the wafer thickness, the wafer edge can be assumed to be in uniaxial tension, as indicated by the FEM results. An angled crack on the wafer edge is shown in Fig. 3.13. When $\beta \neq 0$, both mode I and mode II failures take place and the stress intensity factors are given by [94]:

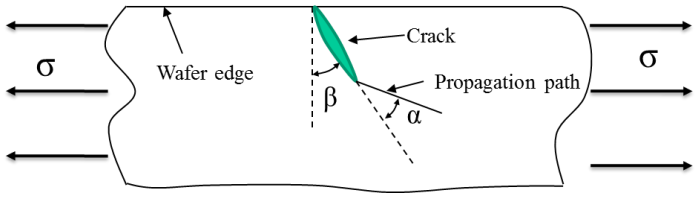

Figure 3.13: Angled wafer edge crack.

$$K_I = K_{I(0)} \cos^2 \beta \tag{3.6}$$

$$K_{II} = K_{I(0)} \cos \beta \sin \beta \tag{3.7}$$

Suppose the crack propagates at an angle α from the crack plane, the local Mode I and Mode II stress intensity factors at the crack tip are given by [94]:

$$k_I(\alpha) = C_{11}K_I + C_{12}K_{II} \tag{3.8}$$

$$k_{II}(\alpha) = C_{21}K_I + C_{12}K_{II} \tag{3.9}$$

where the coefficients are given by

$$C_{11} = \frac{3}{4}\cos(\frac{\alpha}{2}) + \frac{1}{4}\cos(\frac{3\alpha}{2}) \tag{3.10}$$

$$C_{12} = -\frac{3}{4}[\sin(\frac{\alpha}{2}) + \sin(\frac{3\alpha}{2})] \tag{3.11}$$

$$C_{21} = \frac{1}{4}[\sin(\frac{\alpha}{2}) + \sin(\frac{3\alpha}{2})] \tag{3.12}$$

$$C_{22} = \frac{1}{4}\cos(\frac{\alpha}{2}) + \frac{3}{4}\cos(\frac{3\alpha}{2}) \tag{3.13}$$

The crack will propagate if the energy release rate exceeds the fracture toughness:

$$G(\alpha) = \frac{K_I^2(\alpha) + K_{II}^2(\alpha)}{E} \geq G_c \tag{3.14}$$

By maximizing $G(\alpha)$ for a given orientation β, the crack propagation direction α^* can be determined.

For a given crack propagation direction, the critical crack length for a given applied stress can be calculated based on the critical energy release rate principle. The critical crack length ratio $a_{c\beta}/a_{c0}$ is defined as the ratio of the critical length of an angled crack with orientation β divided by the critical length of a pure mode I crack (β = 0) for the same applied stress. Fig. 3.14 shows that for $\beta < 40°$ the angle does not have a significant effect on the critical crack length. Cracks with an orientation of $\beta = 21.9°$ are easiest to propagate with a minimum critical crack length ratio of 0.94.

Wafer breakage tests were carried out using wafers from different sawing conditions. The Weibull distribution, which is commonly used for the analysis of fracture

strength of brittle materials [95], describes the probability of fracture at a given stress level as:

$$P_f = 1 - \exp[-(\frac{\sigma}{\sigma_\theta})^m] \tag{3.15}$$

where σ is the fracture stress, σ_θ is the characteristic stress at which the possibility of fracture is 63.2%; the Weibull modulus, m , describes the strength distribution (higher the value of m, lower the strength variation) [96]. Fig. 3.15 shows the Weibull plots for the wafer groups examined in this study and Table 3.4 summarizes the Weibull parameters and relevant statistics. Note the four line bending is carried out in a way such that the four bending lines are perpendicular to the saw marks.

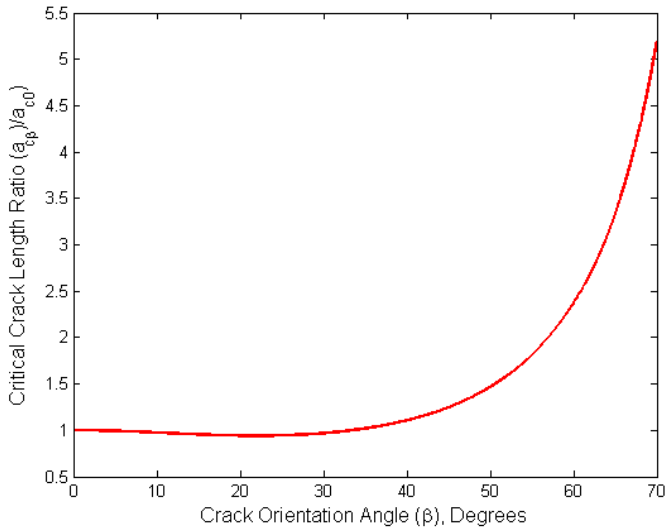

Figure 3.14: Critical crack length ratio in four line bending.

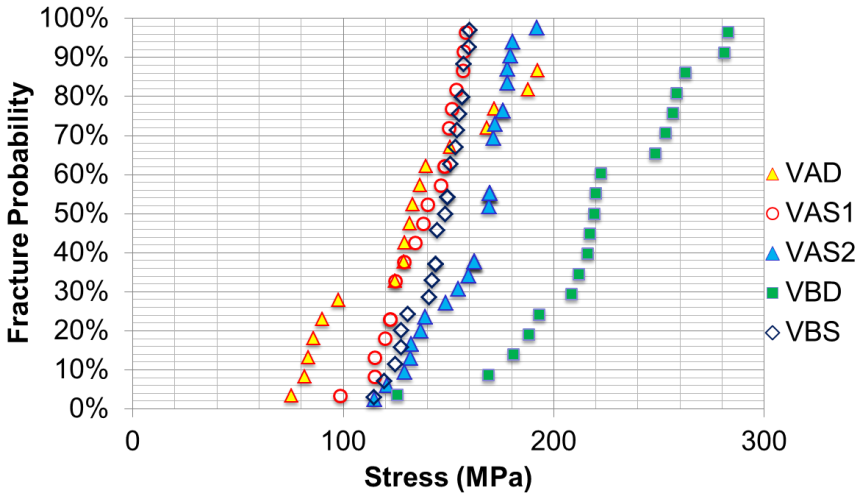

Figure 3.15: Weibull plots for wafer fracture strength in four line bending.

Table 3.4: Four line bending wafer strength statistics.

	VAD	VBD	VAS1	VAS2	VBS
m	3.5	5.8	8.8	8.5	11.7
σ_θ **(MPa)**	151.3	239.4	144.2	169.8	150.2
Expected Strength (MPa)	136.2	221.7	136.4	160.4	143.9
Standard Deviation (MPa)	43.1	44.3	18.6	22.4	14.9

It can be seen that diamond cut wafers have fracture strengths that are at least comparable to slurry cut wafers, although they exhibit larger variation. Note that one group of diamond cut wafers (VBD) has a much higher fracture strength than the others and may have a bimodal fracture probability. Note also that slurry cut wafers sawn using a larger grit size (VAS1, F600) yield a smaller fracture strength than those cut with a smaller grit size (VAS2, F800).

From the LEFM theory, assuming the edge crack to be a quarter-circular crack in a quarter-infinite body as shown in Fig.3.16, the mode I stress intensity factor under a far-field tensile stress σ is given by [97]:

$$K_I = 1.2735\sigma\sqrt{\pi a} \tag{3.16}$$

A crack will propagate under mode I loading condition if the stress intensity factor equals the fracture toughness. The corresponding critical crack length under tensile loading is then given by:

$$a_c = \frac{1}{\pi}\left(\frac{1.2735\sigma_f}{K_{IC}}\right)^2 \tag{3.17}$$

where σ_f is the fracture strength and K_{IC} is the mode I fracture toughness. In the four line bending case, due to the fact that wafer edge cracks are of larger length and the tensile stresses in the large stress region are almost of the same magnitude, wafer breakage is due to the propagation of an edge crack with length equal to the critical crack length.

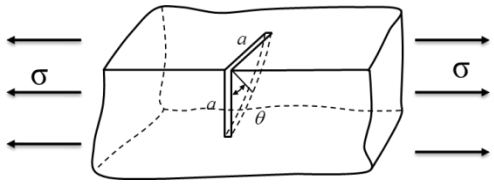

Figure 3.16: Edge crack idealization in four line bending.

The mode I fracture toughness of multicrystalline silicon reported in the literature has relatively large variation (0.86~1.1MPa$\sqrt{\text{m}}$) [98-100]. Using fracture toughness values ranging from 0.86 ~ 1.1 MPa$\sqrt{\text{m}}$ and the four line bending fracture strengths listed in Table 3.4, the corresponding mode I critical crack lengths $a_c$were estimated and are given in Table 3.5. The largest measured crack length is also listed for comparison.

It can be seen that the measured data is in good agreement with the predicted critical crack lengths. However, caution should be applied in making the comparison for three reasons. First, the measured cracks are not necessarily those which lead to fracture,

although they are from the same sawing condition and are therefore supposed to follow the same statistics. Second, as noted earlier, in addition to crack length the crack orientation also plays an important role in wafer failure. Finally, the occurrence of the largest crack in the measurements reported here is a stochastic process. Nevertheless, the measured maximum crack length can still be used as a rough estimate for calculating the wafer fracture strength.

Table 3.5: Fracture strength vs. critical crack length in four line bending.

	VAD	VBD	VAS1	VAS2	VBS
Expected Fracture Stress (MPa)	136.2	221.7	136.4	160.4	143.9
Calculated mode I a_c (μm) (LEFM)	7.8-12.8	3.0-4.8	7.8-12.8	5.6-9.2	7.0-11.5
Measured Largest Edge Crack Length (μm)	8.5	6.3	10.3	7.8	9.7

Biaxial flexure

In order to eliminate the effect of the wafer edges on fracture strength, the biaxial flexure test, which was originally designed for evaluating the strength of ceramics (ASTM F394-74T) [101], was employed to evaluate the mechanical strength of some of the slurry cut Si wafers [102]. The design of the setup is similar to that reported elsewhere [103]. A central cylindrical loading pin pushes on the wafer, which is supported by three smooth steel ball bearings. The three ball bearings are located 120° apart from each other on the edge of an adjustable-radius circle. The centers of the circle, loading pin and the wafer are coincident, as shown in Fig. 3.10.

When loaded, tensile stresses are generated in the wafer surface opposite the locations where the central loading pin and the three support ball bearings contact the wafer. Due to the large deflection, complex loading and boundary conditions, nonlinear FEM modeling is used to compute the stresses. The radius of the circle where the three

supporting bearing balls are located is chosen such that the maximum tensile stress always occurs on the opposite side of the loading pin. A representative maximum principal stress distribution in the wafer back surface is shown in Fig. 3.17.

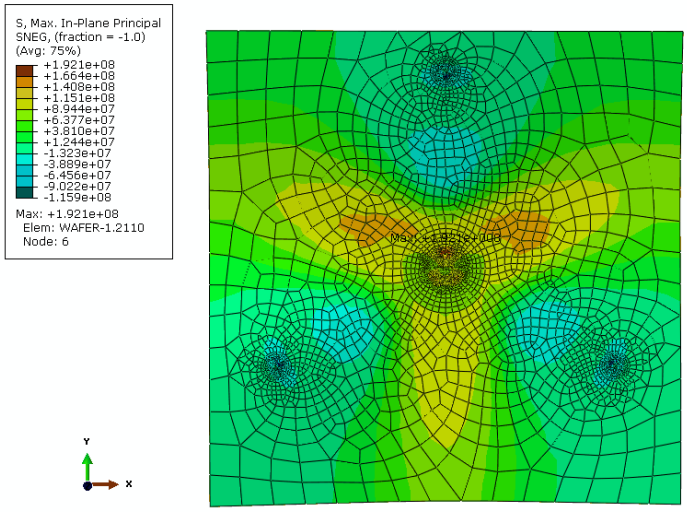

Figure 3.17: Maximum in-plane principal stress distribution in wafer back surface during biaxial bending.

In the biaxial test, the largest stress area is subject to principal stresses σ_1 and σ_2, where σ_1 is greater than σ_2. Fig.3.18 illustrates an angled crack under biaxial loading, for which the mixed mode stress intensity factors are given by [94]:

$$K_I = K_{I(0)}(\cos^2\beta + B\sin^2\beta) \tag{3.18}$$

$$K_{II} = K_{I(0)}\cos\beta\sin\beta(1-B) \tag{3.19}$$

Note that B = 0.8 in this study. Following mixed mode fracture analysis, the critical crack length ratio $a_{c\beta}/a_{c0}$ for angled cracks is shown in Fig. 3.19. Unlike four line bending, the crack orientation does not have a significant effect on the critical crack length as the maximum critical crack length ratio is less than 1.6 at $\beta = 90°$.

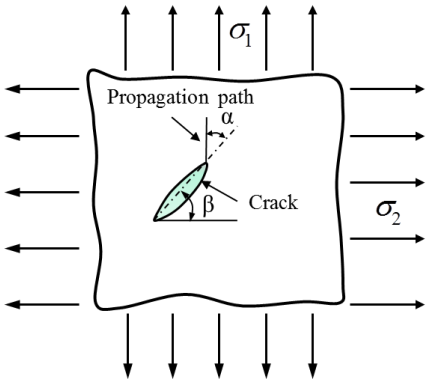

Figure 3.18: Wafer with angled crack subject to biaxial loading.

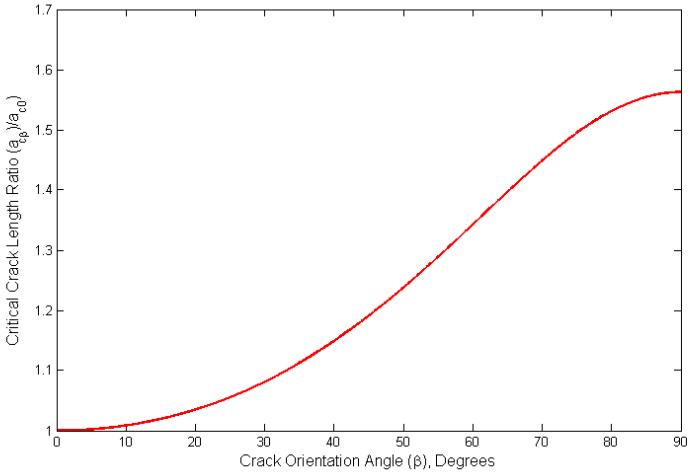

Figure 3.19: Critical crack length ratio for angled cracks.

Biaxial fracture tests were carried out on only the VAS1 and VAS2 wafers in order to compare the fracture strengths obtained in the two testing approaches. Weibull plots of both four line and biaxial test data are shown in Fig. 3.20 and the corresponding statistics are summarized in Table 3.6. It can be seen that the biaxial fracture strength is greater than the four line fracture strength for wafers of the same cutting condition. Also, for the same testing conditions, the fracture strength of VAS1 is always less than VAS2.

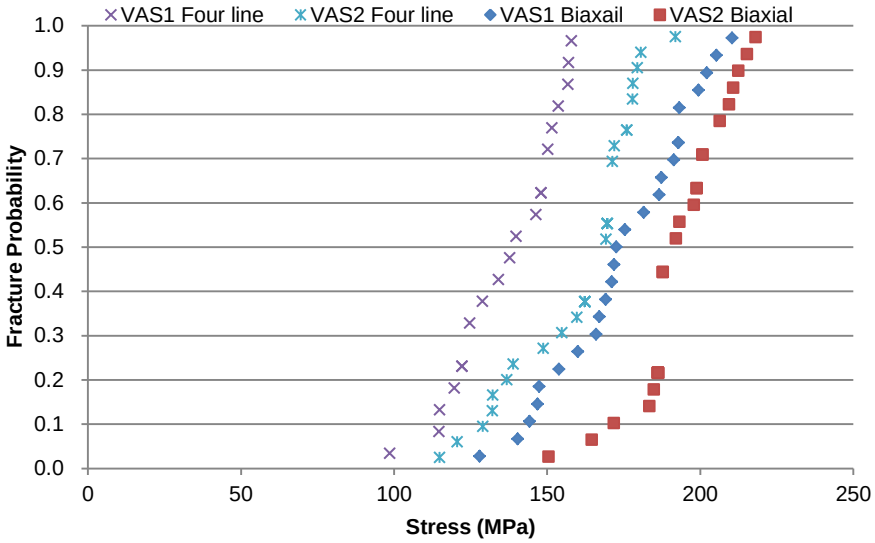

Figure 3.20: Weibull plots for both four line and biaxial bending.

Table 3.6: Four line vs. biaxial line fracture strength statistics.

	VAS1 4 Line	VAS1 Biaxial	VAS2 4 Line	VAS2 Biaxial
m	8.8	8.9	8.5	14.2
σ_θ **(MPa)**	144.2	184.0	169.8	200.9
Expected Strength (MPa)	136.4	176.2	160.4	193.7
Standard Deviation (MPa)	18.6	23.4	22.4	14.7

Assuming that the cracks leading to wafer fracture are half-circular surface cracks (see Fig.3.21), LEFM gives the mode I stress intensity factor as [97]:

$$K_I = 1.1942\sigma\sqrt{\pi a} \tag{3.20}$$

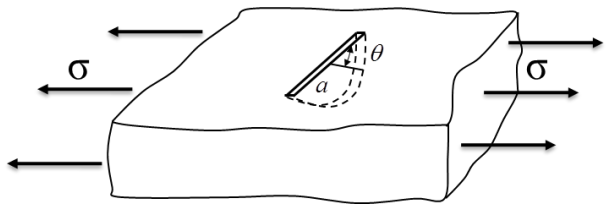

Figure 3.21: Half-circular surface crack in wafer center.

Assuming mode I fracture toughness values from 0.86 ~ 1.1 MPa$\sqrt{m}$, the fracture strengths for the two testing approaches and the corresponding mode I fracture critical crack lengths are compared in Tables 3.6 and 3.7, respectively. The largest measured crack length is also listed for comparison.

It can be seen that the LEFM calculated mode I critical crack length agrees well with the largest measured value. In addition, the table shows that the calculated and measured ratios of the mode I critical crack length for edge cracks to center cracks are also in reasonable agreement.

Table 3.7: Four line vs. biaxial critical crack length analysis.

	VAS1 4 Line	VAS1 Biaxial	VAS2 4 Line	VAS2 Biaxial
Calculated Mode I a_c (μm)	7.8 - 12.8	5.3 - 8.7	5.6 - 9.2	3.9 - 6.3
Measured largest Crack Length (μm)	10.3	5.6	7.8	5.3
Calculated Edge/Center Length Ratio	1.47		1.28	
Measured Edge/Center Length Ratio	1.84		1.47	

3.4 Discussion and Summary

Material removal in slurry sawing of Si wafers is primarily due to three body abrasion between the wire, cutting grits (typically silicon carbide), and silicon ingot in the presence of a cutting fluid. On the other hand, diamond wire sawing is primarily due to two-body abrasion (or scratching) between the diamond grits embedded in the cutting wire and the silicon ingot in the presence of a cutting fluid. The ductile mode cutting grooves (saw marks) observed on diamond cut wafers (see Fig. 3.1) are generated by two-body abrasion.

The variation in wafer thickness and surface roughness observed in slurry cut wafers is attributed to the complex interaction of the wire, abrasive and silicon ingot. For slurry cut wafers, it is believed that the cutting action during wire entry is dominated by the large grits in the slurry while the smaller grits are entrained in the slurry and play a smaller role in the material removal process. The larger grits lead to a rougher surface and wider kerf (thus thinner wafer) where the wire enters the ingot. As the wire moves through the ingot, the larger grits tend to fragment because of their friability and a greater number of smaller grits begin to participate in the three-body abrasion process leading to lower surface roughness and smaller kerf width (i.e. thicker wafer) at wire exit. In addition, the wires are much less confined during entry than inside the sawing channel or during exit from the ingot. The reduced confinement leads to greater vibration perpendicular to the wire speed and feed directions. The vibration of the wire causes the wafer thickness to be smaller at entry than at exit. In the two-body cutting mechanism of diamond wire sawing, hydrodynamic forces play a smaller role and cutting is achieved by the scratching action of diamond grits of random shape and size embedded in the steel wire. Therefore, variations in thickness and roughness tend to be generally more random.

Microcrack measurements showed that edge cracks are longer than center cracks for wafers produced under the same conditions. Diamond cut wafers were found to have a higher crack density while their expected crack length is smaller than for slurry cut wafers. It was also shown that cracks are longer in wafers cut by larger grits in slurry sawing (VAS1 vs. VAS2).

Through the LEFM analysis, it was shown that in addition to crack length the crack orientation plays an important role in crack propagation due to the mixed mode

fracture conditions present in the strength testing methods employed. In four line bending, only cracks oriented at a small angle to the applied tensile stress can cause fracture. In contrast, crack orientation does not have a significant effect on the critical crack length in biaxial flexure tests.

The fracture strength obtained in four line bending tests was found to be directly correlated to wafer edge cracks while the biaxial test results were influenced by cracks in the wafer center. Due to the larger geometric factor in stress intensity calculations and longer cracks in the wafer edge, the four line bending fracture strength was lower than the biaxial strength obtained for wafers cut under the same conditions.

The four line bending tests also revealed that diamond cut wafers have fracture strengths that are comparable to or superior to slurry cut wafers examined in this study. Consequently, from the standpoint of mechanical strength, the fixed abrasive diamond wire sawing technique can be an effective substitute for slurry wire sawing.

These results suggest that fixed abrasive diamond wire sawing of silicon ingots can be a viable alternative to slurry sawing from the standpoint of wafer production [104, 105]. Coupled with higher throughput, this may make fixed abrasive diamond wire sawing the process of choice in the future. Prior to the use of fixed abrasive cutting systems in production, additional investigation is required for the effective removal of the amorphous Si layer produced by ductile mode of cutting. This might be achieved by changing the etching protocol or increasing the etching time [106].

CHAPTER 4

EFFECT OF CRYSTALLOGRAPHIC ORIENTATION ON DUCTILE SCRIBING OF CRYSTALLINE SILICON

This chapter investigates the effect of crystallographic orientation on the mode of material removal (ductile vs. brittle) in diamond scribing of single crystal silicon (sc-Si) and offers an explanation for the observed effects based on the combined role of phase transformation and slip generation.

4.1 Introduction

Although Si is brittle at room temperature, it is well known that brittle materials such as Si, alumina, silicon carbide, fused silica, etc, can undergo ductile mode deformation during cutting [7, 36-48]. Ductile mode cutting of single crystal silicon (sc-Si) is known to take place when the tool feed rate is less than a critical value determined by the material property [7]. Experiments have shown that ductile cutting of sc-Si can be achieved by suitably controlling the tool tip radius and/or the undeformed chip thickness [36]. Analysis of stresses produced in silicon during cutting has shown that ductile removal is a result of the large compressive stress state immediately in front of the cutting tool, which suppresses the growth of pre-existing structural flaws in the material [37-38].

Under ordinary pressures, sc-Si has a diamond cubic crystal structure, which consists of two interpenetrating face-centered cubic (FCC) sub-cubes with the origin of

one displaced $(\frac{1}{4}\frac{1}{4}\frac{1}{4})$ from the other. In other words, one atom of the second sub-cube occupies the site at one-fourth of the distance along a major diagonal of the first sub-cube [9]. Because of the asymmetric and non-uniform lattice distance between atoms, sc-Si has anisotropic properties. In sc-Si, there are preferred slip planes and slip directions along which dislocation motion tends to occur. Slip takes place predominantly on crystallographic planes of maximum atomic density in the closest-packed direction; sc-Si has 12 slip systems in the {111} plane along the <110> direction [9, 107].

It is well-established that even though sc-Si retains its diamond cubic structure at atmospheric pressure, it can be transformed into other phases (crystalline and amorphous) at higher pressures. Note that Si-III, Si-XII and amorphous silicon (a-Si) phases are observed mostly in areas where ductile mode of deformation is observed [43]. Raman spectroscopy is widely used to characterize the appearance of different phases of sc-Si [43, 82]. The technique relies on analysis of Raman scattering of monochromatic light from a laser. The photons emitted by the laser interact with molecular vibrations of the sample, resulting in photon energy being shifted up or down. The shift in energy gives information about the vibration modes and thereby the chemical composition of the sample [83].

Given that sc-Si is anisotropic, the effects of crystallographic orientation on ductile cutting have been studied by others [41, 45-48]. However no detailed scientific explanations for the observations were given. In this study, diamond scribing tests are carried out on the (111), (001) and (110) planes of c-Si along the <111>, <110>, <100> and <112> directions to investigate the effects of crystallographic orientation on the mode of material removal. In particular, the observed differences in the cutting mode

along the different crystallographic planes/directions is explained in terms of the effects of phase transformation and slip generation in sc-Si during scribing [108].

4.2 Experiments

A single crystal cone shaped diamond scriber with 90° included angle was used in the scribing experiments reported here (Fig. 4.1). The tip radius was measured to be ~8μm. In the experimental setup, a semiconductor grade Czochralski (CZ) c-Si wafer was mounted on stacked X-Y-Z motion stages (Aerotech ANT-4V) and a Kistler 9257B 3-component piezoelectric cutting force dynamometer was used to measure the dynamic scribing forces (Fig. 4.2). The X-Y-Z stages have a positioning resolution of 1nm in the Z direction, thus permitting sub-micron depth experiments. The dry scribing experiments were depth controlled where the depth was increased linearly from 0 to 2μm along a 5mm long track. In addition, three scribing speeds of 1, 5 and 10 mm/min per crystal plane-direction combination were used.

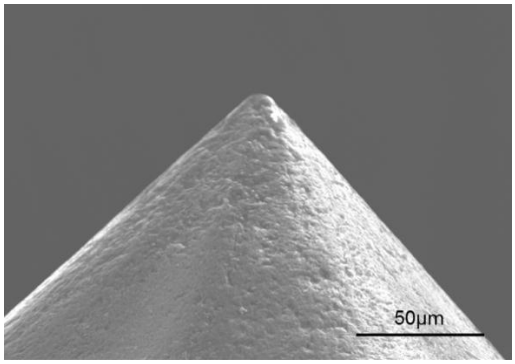

Figure 4.1: SEM image of diamond scriber used in the tests.

In the experiments, polished (111), (001) and (110) Cz-Si wafers were used. The scribing orientations are summarized in Table 1. Note that there is no data in the literature on the mode of material removal in diamond scribing of a (110) sc-Si wafer.

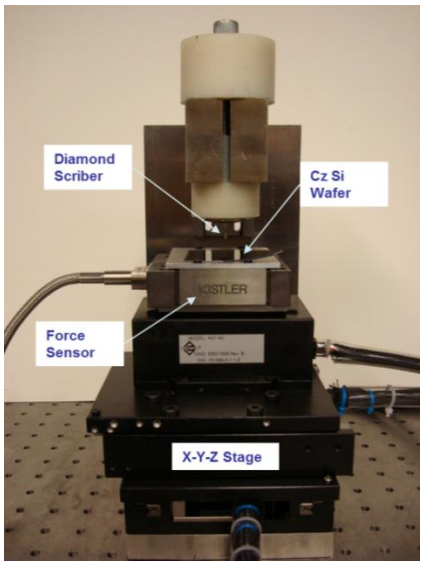

Figure 4.2: Scribing test setup.

Table 4.1: Scribing directions and critical depth as a function of scribing speed (V).

Plane	Scribing Direction	$d_c\,(\mu m)$			
		V1 (1 mm/min)	V2 (5 mm/min)	V3 (10 mm/min)	Average
(111)	$[\bar{1}10]$	1.04	0.82	0.88	0.92
	$[\bar{1}\bar{1}2]$	0.34	0.31	0.52	0.39
(001)	[010]	0.10	0.15	0.12	0.12
	[110]	0.17	0.19	0.15	0.17
(110)	$[\bar{1}10]$	0.69	0.87	0.80	0.79
	[001]	0.23	0.20	0.22	0.22
	$[1\bar{1}\bar{1}]$	1.21	1.24	1.37	1.27

4.3 Results

The mode of material removal in all tests was observed to change from completely ductile, to a combination of ductile and brittle, to completely brittle fracture as the cutting depth was increased. Representative Scanning Electron Microscope (SEM) images of the tracks generated in the (111)$[\bar{1}\bar{1}2]$ orientation shown in Fig. 4.3 clearly reveal this trend. When the scribing depth is small, ductile mode cutting is observed and the track is very smooth and has no cracks. With increasing depth, surface cracks are observed at the edges of the track while evidence of plastic flow can still be observed within the track. The image in the middle (Fig. 4.3) is taken at the location where the first crack was observed. As the depth is increased further, significant evidence of brittle fracture is observed with little or no evidence of ductile cutting.

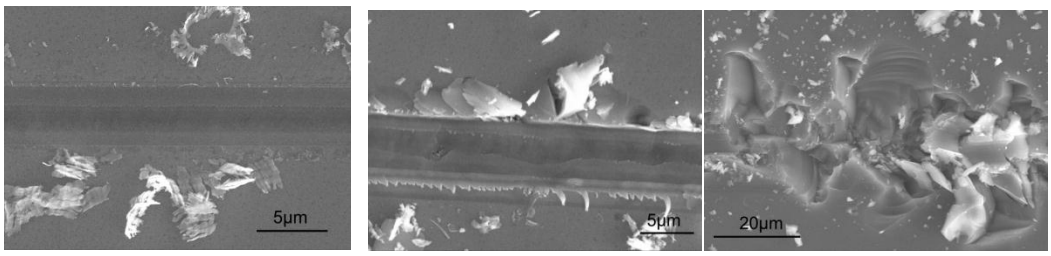

Figure 4.3: Surface morphology of diamond scribed track in (111)$[\bar{1}\bar{1}2]$ c-Si at 1mm/min scribing speed and scribing depths of 0.12 μm (left), 0.34 μm (middle), and 1.22 μm (right), scribing direction is left to right.

While the surface morphology trends are similar in all the tests, certain crystallographic orientations exhibit greater ductile mode behavior than others. Similar to previous work [7, 36-39], a critical depth of cut d_c is used here to quantitatively compare the different test cases. The critical depth is defined as the cutting depth at the location

along the track where brittle fracture is first observed. A large value of d_c implies good ductile cutting behavior of the material. The critical depth location was first observed in a SEM and then the depth was measured by a confocal microscope (LEXT 3D). The confocal microscope enables the reconstruction of the three-dimensional topography from images taken at different focal lengths. Fig. 4.4 shows a sample optical image and the procedure used to determine the critical depth. The depth profile in the cross section of the first crack location is measured as shown in the image on the right in Fig. 4.4. The critical depth d_c can then be obtained by measuring the distance between the wafer surface and the track bottom. The vertical height resolution of the measurement system is 10 nm.

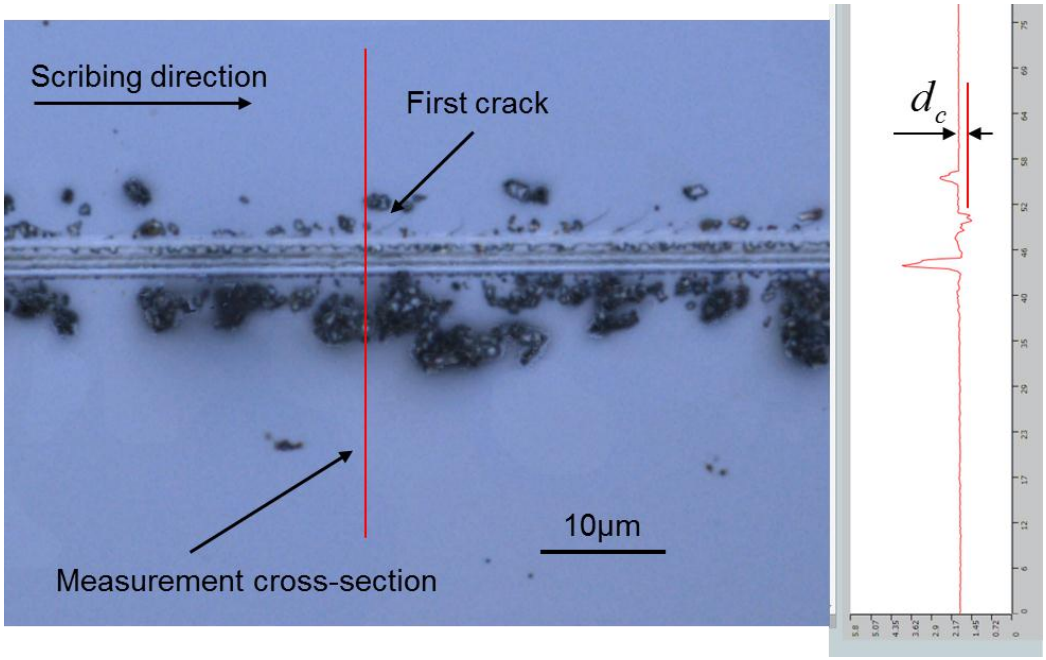

Figure 4.4: Measurement of critical depth of cut d_c.

The critical depths obtained in the scribing tests are summarized in Table 4.1. It can be seen that the critical depths for scribing in the (001) plane are much smaller than

in the other planes, which implies significantly reduced ductile cutting. For tests in the same plane, scribing in the <111> family of directions exhibits greater ductile behavior than in the <110> direction, while scribing in the <100> family of directions has the smallest critical depth. For instance, in the (110) plane, scribing in the $[1\bar{1}\bar{1}]$ direction has the largest critical depth and while scribing in the [001] direction yields the smallest critical depth. For the range of scribing speeds tested, the effect of speed on the critical depth does not appear to be significant.

Figure 4.5 summarizes other interesting surface features seen in the SEM images taken at the critical depth location. Parallel chevron cracks are observed along the edges of the $(111)[\bar{1}10]$ track and they tend to propagate in the $(111)[01\bar{1}]$ direction. Severe cracking is observed immediately following ductile mode cutting when scribing in the (001) wafer. Large pits due to cracking are clearly visible in the (001) [010] track even at small depths of cut. In contrast, ductile mode cutting is observed in the $(110)[1\bar{1}\bar{1}]$ track at scribing depths greater than 1 μm. Note that scribing in the <111> orientation is only possible in the (110) wafer.

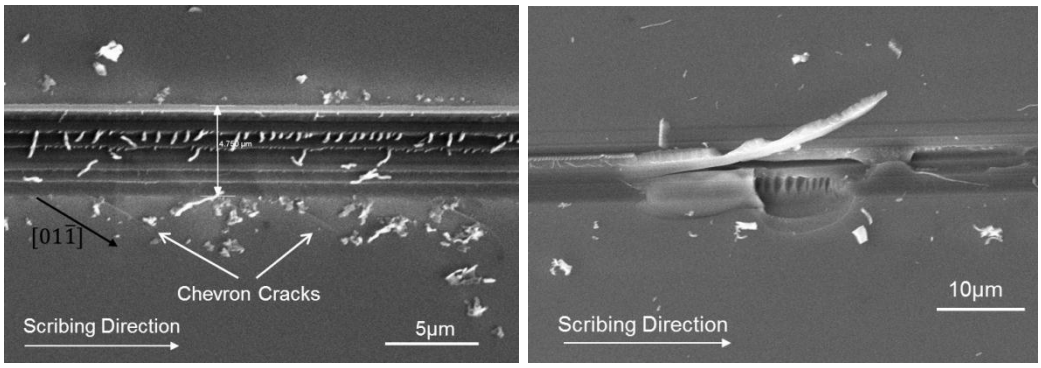

$(111)[\bar{1}10]$ track, 1mm/min $(001)[110]$ track, 1mm/min

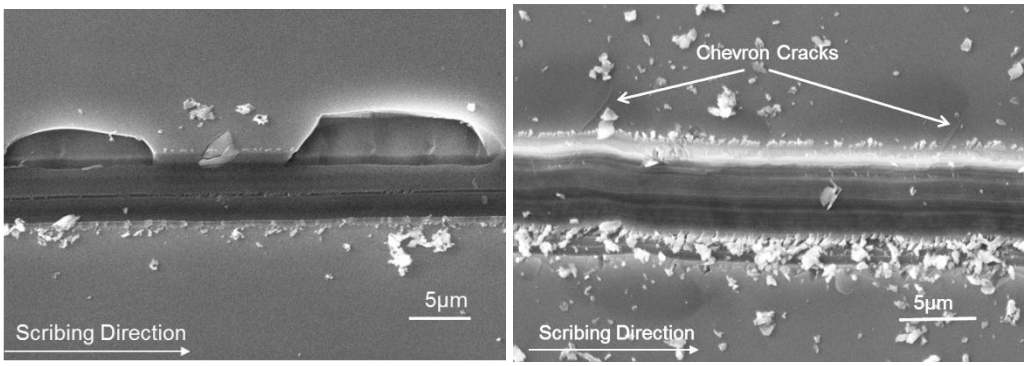

(001)[010] track, 1 mm/min (110)[$1\bar{1}\bar{1}$] track, 1 mm/min

Figure 4.5: Morphology of the scribing tracks.

4.4 Discussion

4.4.1 Phase Transformation of Si during Scribing

Raman spectra obtained from the ductile portion of the track show no evidence of the diamond cubic phase of c-Si, and in most cases reveal only a-Si. It is interesting to note that the Si-XII and Si-III metastable phases were observed only in the 1 mm/min test in the (110) [001] direction, while Raman spectra for the other scribing conditions show only a-Si in the ductile portions of the tracks. The low scribing speed corresponds to a low unloading rate, which likely leads to the formation of the crystalline phases. Representative Raman spectra of the track with only a-Si phase is shown in Fig. 4.6; the black square in the SEM image indicates the area analyzed. It can be seen that the broad peaks at 480 and 170 cm^{-1}correspond to a-Si [109]. Fig. 4.7 shows peaks at Raman shifts of 430 and 350 cm^{-1}, which indicate the presence of Si-XII and Si-III phases, respectively [43,82].

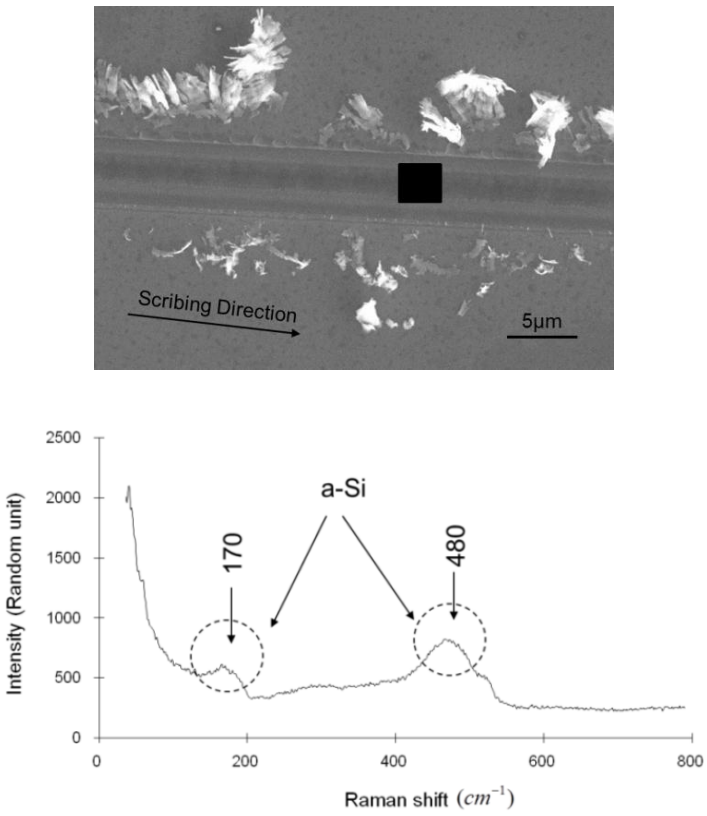

Figure 4.6: Raman spectra of (110) [001] track scribed at 5 mm/min.

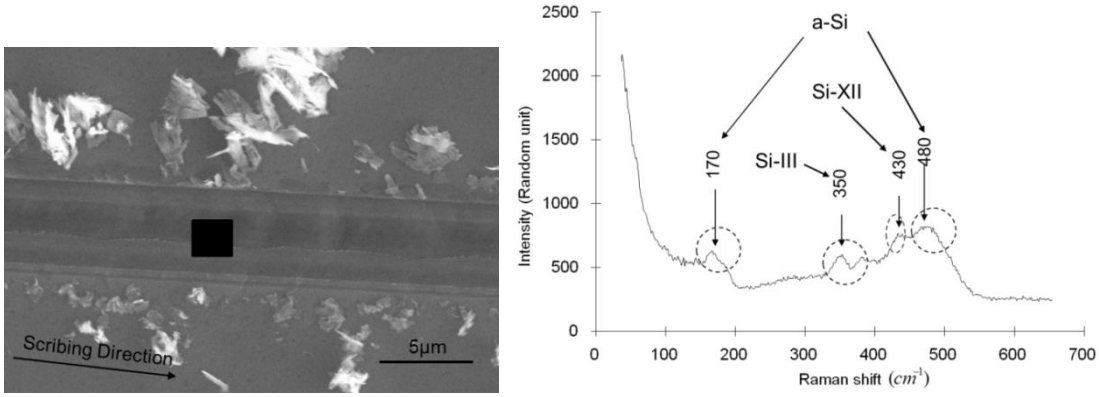

Figure 4.7: Raman spectra of (110) [001] track scribed at 1mm/min.

In regions where both cracking and ductile flow are observed, both diamond cubic and a-Si phases are present, whereas only the diamond cubic Si phase is present in areas

of brittle fracture. This confirms that the ductile flow behavior observed in the scribing tests is characterized by phase transformation of sc-Si.

4.4.2 Dislocation Generation in Scribing of Silicon

Prior studies on deformation of sc-Si suggest that there is no dislocation generation in conventional mechanical testing at temperatures below 450° [110]. However, evidence of slip due to dislocation motion in silicon has been widely observed under extreme loading conditions such as in indentation and scribing [80-82, 111- 112] where localized stresses approach the theoretical shear strength of silicon. In fact, evidence of slip has been shown in micro-indentation tests under all loading conditions, irrespective of whether the maximum load exceeds the required load for phase transformation or not [111]. The high localized hydrostatic stress directly underneath a sharp indenter is believed to be the cause of phase transformation, while the shear stress on the {111} slip planes of sc-Si is believed to provide the driving force for slip [42, 80]. It has been shown in previous studies that dislocations travel in the {111} plane after nucleation until their progress is halted by intersection with other dislocations or by intersection with the free surface. This produces the characteristic "V" shape of the dislocation slip bands reported in literature (see Fig. 4.8). Moreover, when indenting sc-Si, the sequence of deformation consists of initial deformation via slip followed by phase transformation when the critical pressure for transformation is reached [111].

The hydrostatic and shear stresses generated in scribing can be as high as in indentation. Therefore, a similar material response under load, i.e. slip generation and phase transformation, is expected. In fact, cross-sectional TEM images of diamond turned

silicon show evidence of dislocations in the {111} plane and <110> direction, as well as a-Si on the surface [42].

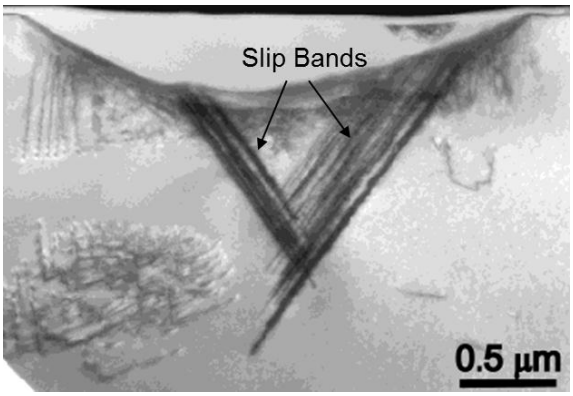

Figure 4.8: TEM image of indentation in sc-Si made using a spherical indenter (after Bradby et al. [112]); clear evidence of slip bands can be seen.

While the experimental evidence presented in this work confirms the role of phase transformation in ductile mode scribing, the reason for the orientation dependence of the scribing mode is not that obvious and requires further scrutiny. It is hypothesized that the dependence of the mode of cutting on crystallographic orientation is due to differences in the ease of activating slip systems in sc-Si. The Schmid factor is commonly used to evaluate the likelihood of activating slip systems in a particular orientation and is given by $\cos\varphi \times \cos\lambda$, where φ is the angle between the loading direction and the direction normal to the slip plane, and λ is the angle between the loading and slip directions. For a given load, a large Schmid factor indicates a large magnitude of the resolved shear stress and therefore a higher likelihood for slip in that direction. Table 4.2 lists the Schmid factors for all twelve {111} <110> possible slip systems ($[\bar{1}0\bar{1}]$, $[0\bar{1}\bar{1}]$, $\left[\bar{1}10\right]$ directions in the $(\bar{1}\bar{1}1)$ plane, $[0\bar{1}\bar{1}]$, $[10\bar{1}]$, [110] directions in the $(1\bar{1}1)$ plane, $[\bar{1}0\bar{1}]$, $[01\bar{1}]$, [110]

directions in the $(\bar{1}11)$ plane, $[01\bar{1}]$, $[10\bar{1}]$, $[\bar{1}10]$ directions in the (111) plane) in diamond cubic silicon for the loading directions used in the current work. Note that the $[\bar{1}\bar{1}2]$ scribing direction belongs to the <112> family, etc. Also that there are two major loading directions in the scribing tests reported here, one normal to the wafer surface and the other along the scribing direction. The third scribing force component, which is perpendicular to both the normal and scribing directions, is negligible.

Table 4.2: Schmid factors for loading directions used in the experiment.

Slip Plane	Burgers Vector	Schmid Factor			
		Load Direction $[\bar{1}\bar{1}2]$ (<112>)	**Load Direction $[\bar{1}10]$ (<110>)**	**Load Direction [010] (<100>)**	**Load Direction $[1\bar{1}\bar{1}]$ (<111>)**
$(\bar{1}\bar{1}1)$	**$[\bar{1}0\bar{1}]$**	0.2722	0.4082	0	0
	$[0\bar{1}\bar{1}]$	0.2722	0.4082	0.4082	0.2722
	$[\bar{1}10]$	0	0	0.4082	0.2722
$(1\bar{1}1)$	**$[0\bar{1}\bar{1}]$**	0.1361	0	0.4082	0.2722
	$[10\bar{1}]$	0.4082	0	0	0.2722
	[110]	0.2722	0	0.4082	0
$(\bar{1}11)$	**$[\bar{1}0\bar{1}]$**	0.1361	0	0	0
	$[01\bar{1}]$	0.4082	0	0.4082	0
	[110]	0.2722	0	0.4082	0
(111)	**$[01\bar{1}]$**	0	0.4082	0.4082	0
	$[10\bar{1}]$	0	0.4082	0	0.2722
	$[\bar{1}10]$	0	0	0.4082	0.2722

It can be seen that loading in the <111> family of directions yields small non-zero Schmid factors for six slip systems, which implies that only these six slip systems will be activated, while loads in the <100> family of directions have the largest Schmid factors for eight slip systems leading to the activation of eight out of the twelve slip systems. The Schmid factors are also large for loading in the <110> family of directions but will

activate only four out of the twelve slip systems. Scribing tests with larger non-zero Schmid factors will activate more slip systems and will therefore induce more slip.

It is well known that dislocation entanglement arising from slip can lead to strengthening of crystalline materials [114]. In sc-Si, it has been confirmed that interlocking of dislocations can cause hardening [74-76]. This implies that a higher load will be required to produce the same scribing depth in a material that exhibits greater slip. Therefore, crystallographic directions that have larger Schmid factors require higher loads to generate the same scribing depth. Hence, for a given scribing depth, scribing in the <100> direction requires a higher load than scribing in the <111> direction. Note that although the Schmid factors for <100> and <110> are the same, the number of slip systems that can be activated when scribing in the <100> direction is higher (8) than for scribing in the <110> direction (4). While the compressive stress produced by the applied load may induce phase transformation, the corresponding tensile stress in the material will cause fracture if the stress intensity factor exceeds the material's fracture toughness. Details of the theoretical analysis of stresses generated by scribing can be found in [61]. For the three possible modes of crack propagation, namely the crack opening mode (mode I), the in-plane shear mode (mode II), and the out-of-plane shear mode (mode III), the stress intensity factors can be expressed as [94]:

$$K_{(I,II,III)} = Y\sigma\sqrt{\pi a} \tag{4.1}$$

where σ is the applied tensile stress, a is the characteristic crack dimension and Y is a dimensionless constant that depends on the geometry and loading mode. As the applied stress σ increases, the value of K also increases, and when K exceeds the fracture toughness (K_c) of the material, the crack propagates and fracture occurs. In scribing tests

along different directions but the same scribing depth, the direction requiring a higher load will more easily cause the stress intensity factor to exceed the facture toughness and will therefore generate more fracture. Thus, scribing in the <100> direction, which has larger Schmid factors and therefore more slip and material strengthening, will exhibit greater fracture than scribing in the <110> direction, whereas scribing in the <111> direction will exhibit the least fracture (and therefore the greatest ductile flow).

Table 4.3 confirms the foregoing analysis by comparing the measured critical depths of cut for scribing in the (110) plane in different directions. Specifically, the critical depth d_c is largest along $[1\bar{1}\bar{1}]$ (smallest Schmid factor per Table 4.2), and is somewhat smaller along $[\bar{1}10]$ (fewer activated slip systems), and is the least in the [001] direction (highest number of slip systems activated), as shown in Table 4.3. For scribing in the same family of directions but in different crystallographic planes, differences in ductile cutting are determined by the ease of dislocation generation in orientations normal to the planes. Comparing the scribing tests along $(111)[\bar{1}10]$ and $(001)[110]$ (see Table 4.1), although the tangential forces act in the <110> family of directions, the normal load acting along <111> will induce less cracking than when acting along <100>. Thus, scribing in $(111)[\bar{1}10]$ is expected to produce more ductile behavior than scribing in $(001)[110]$. This is confirmed by the higher value of d_c for $(111)[\bar{1}10]$ (see Table 4.1).

Table 4.3: Schmid factor vs. d_c in (110) plane, along [001], $[\bar{1}10]$ and $[1\bar{1}\bar{1}]$ directions.

	[001]	**$[\bar{1}10]$**	**$[1\bar{1}\bar{1}]$**
Number of non-zero Schmid factors	8	4	6
Schmid factor value	0.4082	0.4082	0.2722
Average d_c in (110) plane (μm)	0.22	0.79	1.27

Based on the above analysis, it can be concluded that, for a given depth of cut, scribing along an orientation with large Schmid factors will activate more slip systems, which increases the material strength and therefore the tensile stress generated in the material, leading to increased brittle fracture. In contrast, orientations with fewer activated slip systems and smaller Schmid factors exhibit more ductile behavior.

4.5 Summary

The crystallographic orientation dependence of ductile mode scribing in sc-Si was investigated via increasing depth diamond scribing experiments. It was found that scribing in the (111) plane exhibits more ductile cutting than in the (110) plane, while the greatest amount of brittle fracture was found when scribing in the (001) plane. For scribing in the same plane, the <111> direction exhibits more ductile cutting than the <100> direction. Raman spectra-based phase analysis of the scribed tracks indicated that ductile mode behavior of c-Si is achieved through phase transformation from Si-I to Si-II during loading and, depending on the unloading rate, to a-Si or Si-XII and Si-III phases. It is concluded that loading in an orientation with the largest Schmid factor tends to activate more slip systems through generation and motion of dislocations, which trap each other and thereby strengthen the material. This strengthening in turn implies that a higher tensile stress is generated in the material for the same depth of scribing. The higher stress in turn results in more brittle fracture, which yields a smaller critical depth of cut.

CHAPTER 5

MODELING AND ANALYSIS OF DUCTILE-TO-BRITTLE TRANSITION IN DIAMOND SCRIBING OF SILICON

The effects of scriber tip geometry, coefficient of friction and external hydrostatic pressure on the critical depth of cut associated with ductile-to-brittle transition and crack generation in diamond scribing of single crystal silicon (sc-Si) are analyzed via an eXtended Finite Element Method (XFEM) based model, which is experimentally validated.

5.1 Introduction

In order to understand the basic cutting mechanisms involved in the diamond wire sawing process and their effect on surface integrity of silicon wafers, a fundamental study of the mechanics of interaction between a diamond scriber and silicon is necessary and discussed in this chapter.

It has been shown in Chapter 4 that crystalline silicon (c-Si) exhibits ductile behavior when cut at low feed rates and it is widely believed that ductile behavior of silicon is due to transformation of the diamond cubic phase of silicon to a metallic phase under high contact pressures [36-48]. With increase in scribing depth, there is transition from purely ductile mode cutting, which yields a smooth crack-free surface, to a mix of ductile and brittle fracture and then to complete brittle fracture.

Prior work has shown that the critical depth for transition from ductile to brittle mode of cutting is given by [7]:

$$d_c = 0.15(\frac{E}{H})(\frac{K_c}{H})^2 \quad (5.1)$$

where K_c is the fracture toughness, H is the hardness and E the elastic modulus. This expression, while useful, does not explicitly account for the effects of scriber tip geometry, friction, etc. Cutting experiments on silicon indicate that the critical depth varies with changing tip radius [36-38].

Prior work on ductile cutting of silicon is limited to single point turning or scribing experiments with a diamond tool of specific tip geometry [36-39]. In contrast, fixed abrasive diamond wire sawing is characterized by a wide distribution of grit shapes, sizes, tip radii and cutting conditions, whose effects are not well-understood. Consequently, this chapter investigates the effects of diamond grit shape, coefficient of friction and cutting depth on the ductile-to-brittle transition in diamond scribing of monocrystalline silicon using the eXtended Finite Element Method (XFEM) to model crack initiation and propagation during the scribing process.

5.2 Modeling

5.2.1 XFEM Overview

The XFEM is an extension of the conventional finite element method for structural analysis and allows modeling of 3D nucleation of discontinuities (e.g. cracks) in the material without requiring explicit remeshing of the crack surfaces [115-116]. A discontinuous jump function and asymptotic crack-tip displacement fields are added to the finite element approximation to account for the crack using the notion of partition of unity. The presence of discontinuity in the material is modeled via special enrichment

functions in conjunction with additional degrees of freedom. This is accomplished using the displacement vector function u as follows [117]:

$$u = \sum_{I=1}^{N} N_I(x)[u_I + H(x)a_I + \sum_{\alpha=1}^{4} F_\alpha(x)b_I^\alpha] \quad (5.2)$$

where $N_I(x)$ are the nodal shape functions; u_I is the nodal displacement vector for the continuous part of the finite element solution; the second term is the product of the nodal enriched degree of freedom vector, a_I, and the discontinuous jump function $H(x)$ across the crack surfaces; the third term is the product of the nodal enriched degree of freedom vector, b_I^α, and the elastic asymptotic crack-tip functions, $F_\alpha(x)$. Additional details of the XFEM approach can be found in [117]. The first term on the right-hand side of Eq. (2) is applicable to all the nodes in the model; the second term is valid for nodes of elements that are intersected by the crack; and the third term is used only for nodes of the element that contains the crack tip. In the present work, the XFEM formulation available in the commercial finite element code ABAQUS/Standard 6.10 is used to build the model.

Note that damage (crack) modeling is achieved via a traction-separation law and follows the general damage modeling framework in ABAQUS 6.10, including specification of a damage initiation criterion and damage evolution law, which are defined as material properties.

5.2.2 Material Properties

In order to simulate the mechanical interaction of a diamond scriber with silicon using XFEM, a constitutive model for the material behavior must be defined. Under tensile load, silicon typically undergoes elastic deformation till fracture occurs. However,

it undergoes phase transformation when subjected to a sufficiently high hydrostatic stress. Therefore, the constitutive model must account for both phase transformation and elastic-fracture characteristics.

Under tensile load, the anisotropic elastic property of silicon is defined as:

$$\sigma_{ij} = C_{ijkl}\varepsilon_{kl} \text{ or } \varepsilon_{ij} = S_{ijkl}\sigma_{kl} \tag{5.3}$$

where *C* is the stiffness matrix and *S* is the compliance matrix. Since it is of interest here to model the scribing process in (111) silicon in the <110> orientation, the elements of *C* and *S* can be identified through crystallographic transformation [11].

Since transformations from the metallic Si-II phase to higher pressure phases are reversible [14-17], only the property of Si-II is included in the material model. The general behavior of silicon in compression is modeled as elastic-plastic. As shown in Fig. 5.1, silicon exhibits anisotropic elastic behavior below point 1, while it behaves plastically after point 1. The region between point 1 (corresponding to the lowest pressure needed for Si-I to Si-II transformation [118]) and point 2 (corresponding to the highest pressure needed for Si-I to Si-II transformation [14]) represents the region of phase transformation to Si-II. Between points 2 and 3 (where Si-II to Si-V transformation occurs [14]), Si-II is assumed to exhibit linear hardening behavior under uniaxial loading. The material constants for phase transformation are calculated from the transformation pressure data reported in literature and are reproduced in Table 5.1.

The fracture strength of (111) silicon is used as the crack initiation criterion. Since there is a wide variation in fracture strength data reported in the literature, a fracture strength of 4 GPa derived from surface acoustic wave pulse tests on monocrystalline

silicon without any pre-crack or notch [119] is used in this work. The crack propagation criterion is defined in terms of the energy release rate as follows:

$$G \geq G_c = 2w_f \tag{5.4}$$

where $G$is the energy release rate, $G_c$is the fracture toughness, w_f is the energy needed to create a new surface and is equal to 1.15 $\mathrm{J/m^2}$ for {111} cleavage plane [120].

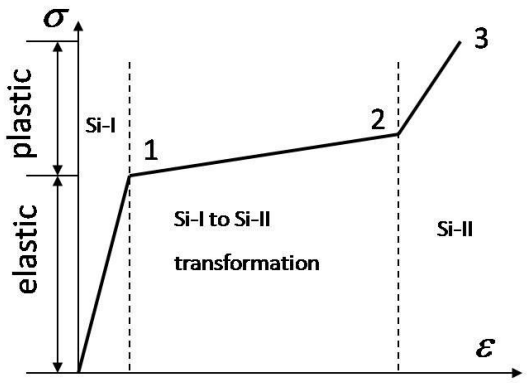

Figure 5.1: Constitutive material model for silicon.

Table 5.1: Material property constants used for phase transformation model.

Point	Stress (GPa)	True Strain	Effective Plastic Strain
1	8.8 [118]	0.05	0
2	11.2 [14]	0.42	0.35
3	16.4 [14]	0.46	0.36

5.2.3 Scriber Geometry and Scribing Process

Initially, only two scriber tip shapes are modeled and compared with experimental results. Scriber I has a truncated conical shape with 60° included angle and a flat top of 10 μm diameter (see Fig. 5.2). Scriber II (see Fig. 5.3) is conical with a 120° included angle and a tip radius of 3 μm. Frictional contact between the scriber surfaces and silicon

is modeled with friction coefficients of 0.1 and 0.2 used for the two scribing conditions, respectively. These values are estimated from force measurements made in scribing tests performed in air. Note that the coefficient of friction variation is intended to simulate variation in the cutting fluid properties used in the diamond wire sawing process.

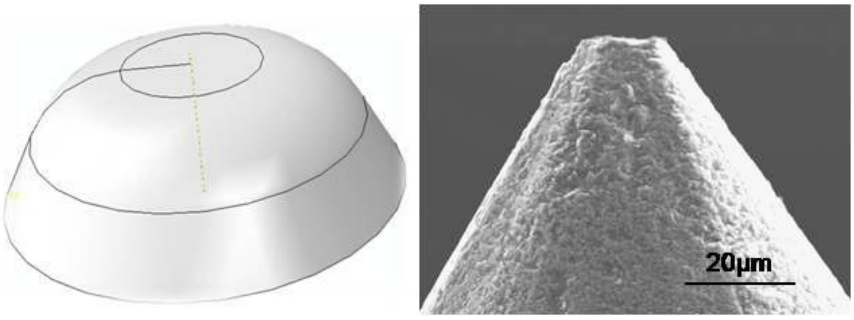

Figure 5.2: Scriber I geometry (sketch on left is model of scriber tip only).

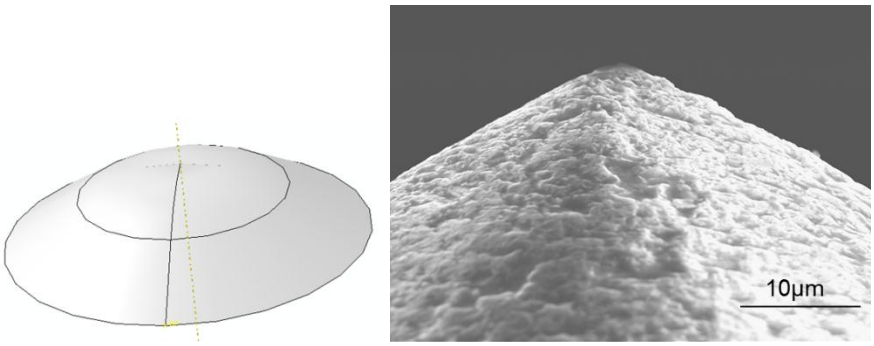

Figure 5.3: Scriber II geometry (sketch on left is model of scriber tip only).

A gradually increasing depth of cut is used to simulate the scribing process. Also, due to symmetry in the scribing geometry, only a one-half 3D model of the scribing process is built and solved. Note that preliminary simulations showed that no cracks nucleate in the plane of symmetry. Finally, it should be noted that the model does not consider removal of material during scribing.

5.3 Results

5.3.1 Model Simulations

The principal stress contours for the two scriber geometries have similar features and the maximum principal stress map before the crack generation for Scriber I is shown in Fig. 5.4. And the stress map and crack generation and propagation results for Scriber II are shown in Fig. 5.5. It can be seen that as the scribing depth increases, the compressive stress field directly under the scriber and the tensile stress field behind the scriber tip increase in magnitude. At a certain location along the scribing direction, the tensile stress exceeds the fracture strength criterion and surface cracks nucleate and propagate when the energy release rate exceeds the fracture toughness of the material. Note that the semi-circular crack path follows the tensile stress contours.

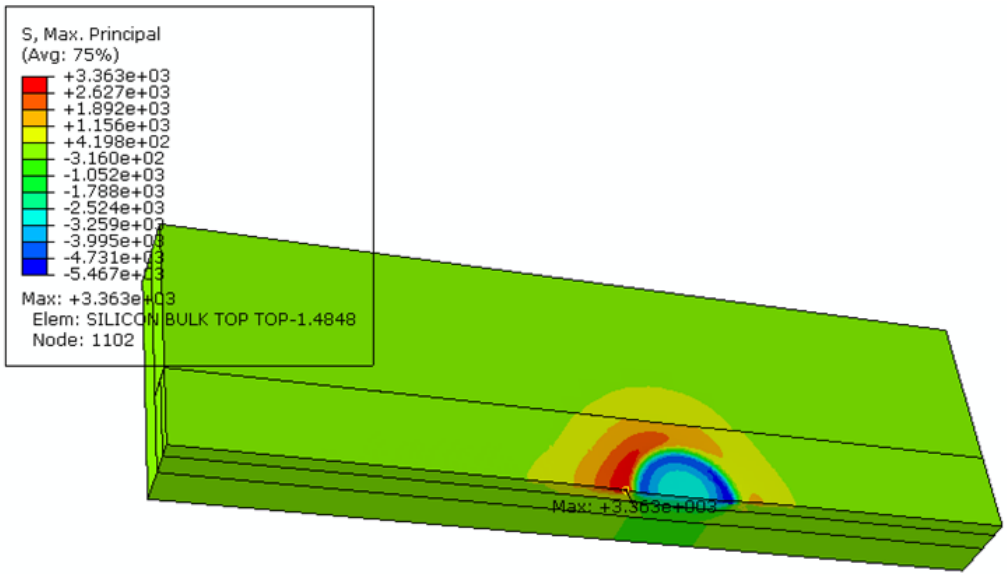

Figure 5.4: Principal stress before crack generation for Scriber I (scriber not shown).

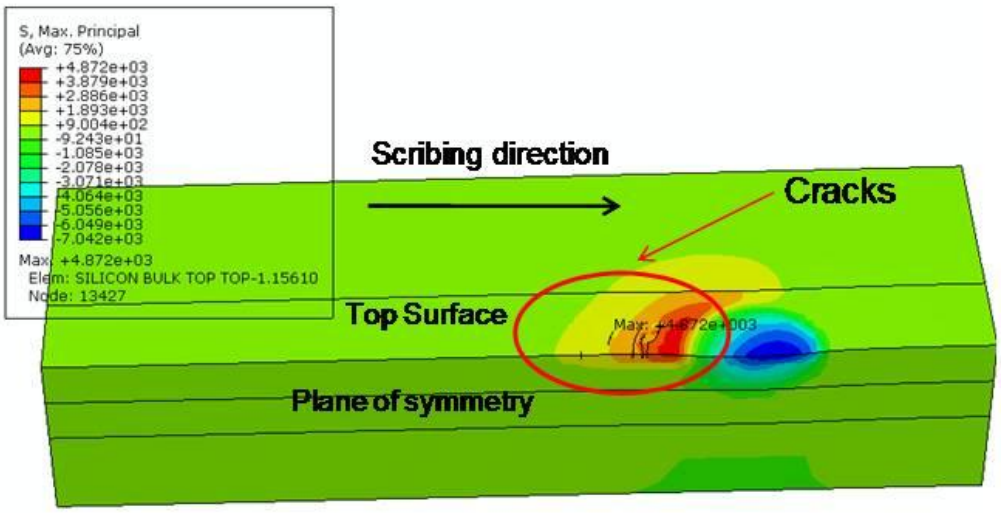

Figure 5.5: Principal stress and crack generation for Scriber II (scriber not shown).

As shown in Fig. 5.6, two types of semi-circular (or "chevron") cracks are observed in the two scribing simulations. Type I refers to crack propagation that starts from the center of the scribing track and curves outward in accordance with the tensile stresses. Type 2 cracks are initiated from outside the scribing track and follow the maximum tensile stress contour towards the center of the scribing track.

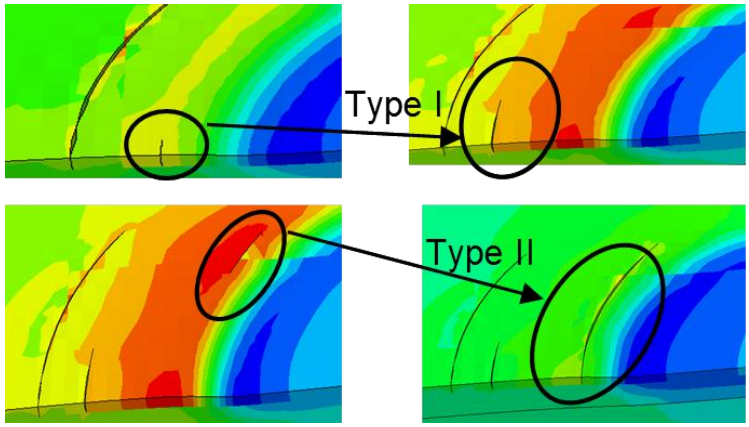

Figure 5.6: Crack propagation patterns (left figures: crack initiation, right figures: crack propagation).

Figure 5.7 shows the evolution of principal (tensile) stress with scribing depth for the two scriber shapes used in the simulations. It is seen that the tensile stress increases sharply with increase in cutting depth for Scriber II, while the increase is more gradual for Scriber I. Consequently, the critical depth of cut, which corresponds to the crack initiation point, is much greater for the blunt scriber (Scriber I) than for the sharp scriber (Scriber II). The hydrostatic pressures corresponding to the crack initiation points are 9.45 GPa and 9.19 GPa, respectively, which are sufficiently high for phase transformation of silicon. Consequently, ductile mode of cutting is expected prior to crack initiation.

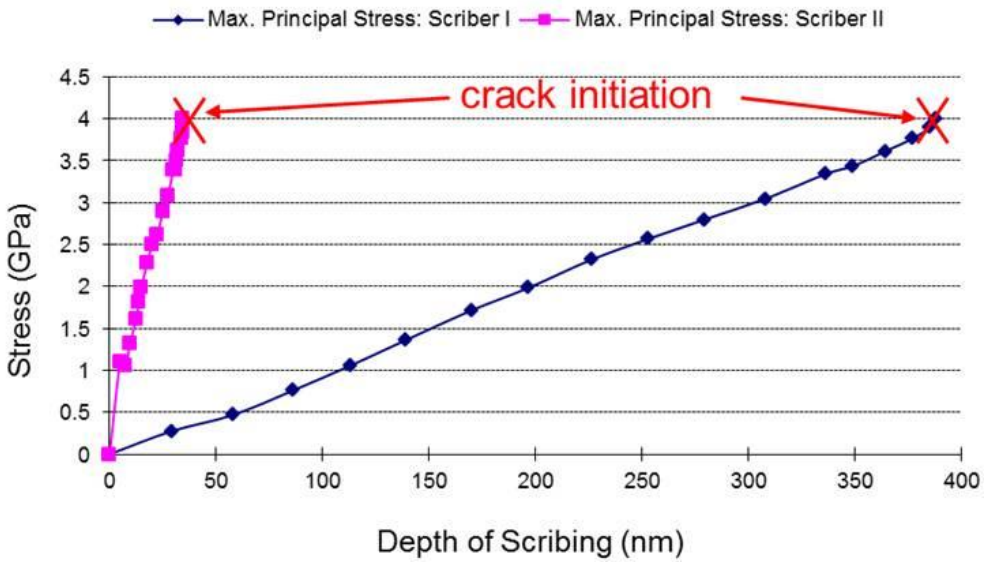

Figure 5.7: Evolution of stress with scribing depth.

5.3.2 Validation Experiments

Gradually increasing depth of cut (0-2µm) single grit diamond scribing experiments were carried out on a polished CZ silicon wafer in the (111) <110> orientation to validate the XFEM model. A semiconductor grade Czochralski (CZ) c-Si

wafer was mounted on stacked X-Y-Z motion stages (Aerotech ANT-4V) and a Kistler 9257B 3-component piezoelectric cutting force dynamometer was used to measure the dynamic scribing forces (see Fig. 4.2). Note that all the tests were performed under ambient conditions without any cutting fluid. The two scriber geometries used in the model simulations discussed previously were employed in the actual tests.

Figure 5.8 shows a comparison of the surface morphology (see SEM image) obtained with Scriber I and the corresponding model XFEM result. It can be seen that the simulated and predicted crack paths are similar. Prior to crack initiation in the experiment, the track produced by the scriber clearly shows evidence of ductile cutting. The simulated critical depth of cut (388 nm) is in reasonable agreement with the measured depth (318±37 nm). For Scriber II, the simulated critical depth (35 nm) was also found to be in reasonable agreement with the measured depth (52±8 nm). Differences in the measured and simulated critical depths can be attributed to the idealized model of the scriber geometry, variation in the fracture strength of silicon, and difficulty in precisely identifying the first crack initiation point in the experiment.

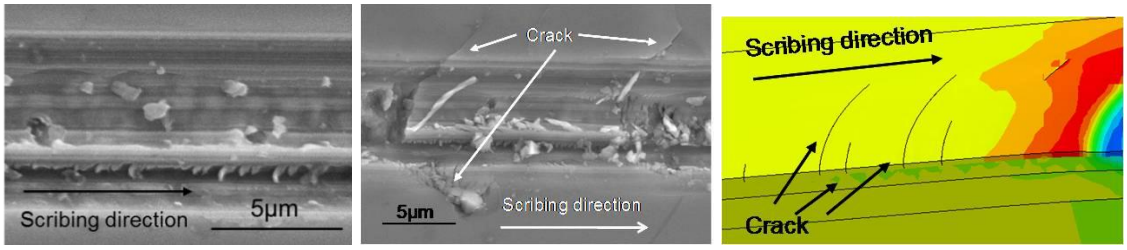

(a) (b) (c)

Figure 5.8: (a) Ductile flow prior to crack, (b) measured, and (c) simulated crack paths for Scriber I.

A sensitivity study was carried out to understand the impact of uncertainty in material properties on the critical depth of cut for Scriber I. For fracture strengths of 3.6 GPa, 3.8 GPa, 4.2 GPa and 4.4 GPa and a constant friction coefficient of 0.1, critical depths of cut of 287 nm, 294 nm, 424 nm and 431 nm, respectively, are obtained. These values are in the same range as the measurements in the current study. Keeping the fracture strength fixed at 4 GPa and changing the friction coefficient to 0.08, 0.09, 0.11 and 0.12, critical depths of cut of 408 nm, 397 nm, 378 nm and 371 nm, respectively, are obtained. These simulation results indicate that variation in the fracture strength has greater influence on the critical depth of cut than variation in the friction coefficient. Therefore, uncertainty in the fracture strength and/or friction coefficient in the experiments can also contribute to the observed discrepancy between the modeling and experimental results.

5.3.3 Effects of Scriber Shape and Friction

The validated XFEM model was used to analyze the effects of diamond scriber shape and friction coefficient on the stresses and crack initiation. A number of scriber shapes including spherical tips with different radii, conical tips with different included angles and faceted tips such as Berkovich and Vickers were modeled and simulated.

Figure 5.9 shows the effects of scribing depth and friction coefficient for a spherical tipped scriber with a tip radius of 3 μm (similar to Scriber II presented earlier). It can be seen that a higher friction coefficient produces a larger tensile stress with increasing depth and a correspondingly smaller critical depth of cut for ductile-to-brittle transition. This implies that lowering the friction coefficient will delay crack initiation and hence promote ductile cutting, which yields a smooth crack-free surface. The

frictionless case is presented here only for comparison and does not have practical significance.

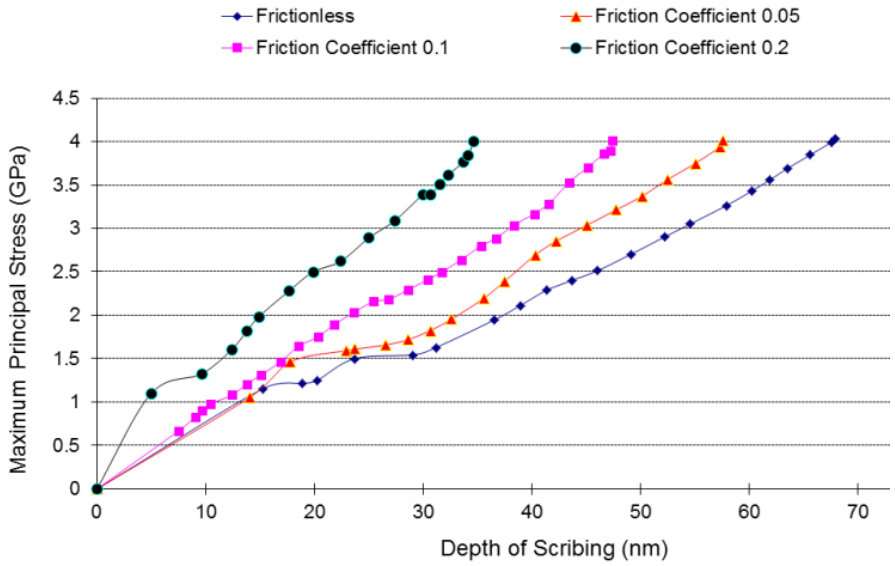

Figure 5.9: Effect of friction and scribing depth on stress evolution (spherical scriber with 3 µm tip radius).

Figure 5.10 shows the effects of scriber tip radius and friction coefficient on the critical depth of cut. It is clear that the critical depth is higher for a larger tip radius and lower friction coefficient. The higher critical depth is attributed to the large compressive stress field induced by the larger tip radius, which inhibits fracture initiation [36]. In all cases, the corresponding hydrostatic pressure for the crack initiation ranges from 9-15 GPa, which suggests material removal via ductile mode of cutting occurs prior to crack initiation.

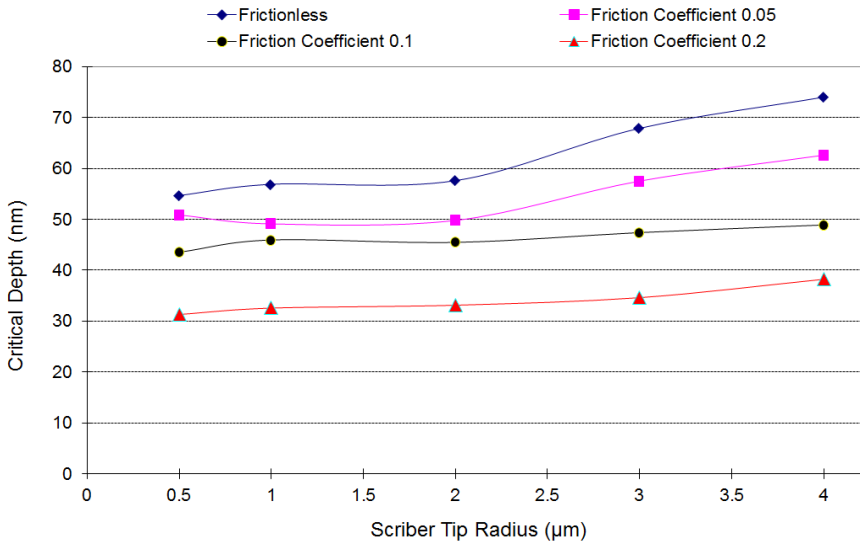

Figure 5.10: Effect of tip radius and friction on critical depth for spherical tips.

The effects of scribing depth and included angle of a sharp (20 nm tip radius) conical scriber on the stresses and critical depth were also simulated. A friction coefficient of 0.05 was assumed. Figure 5.11 shows the effect of scribing depth on the sub-surface stress contours for a 150° included angle scriber. It is seen that the maximum stress occurs under and slightly behind the scriber-silicon contact area. The sectional view reveals fairly high sub-surface tensile stresses, whose distribution resembles the shape of the median and/or lateral cracks that are known to occur in the sub-surface for sharp indenters [27-28]. However, the sub-surface tensile stress in the present case is insufficient (< 4GPa) to nucleate cracks, and as the scribing depth increases the maximum principal stress shifts to the surface and finally produces surface cracks.

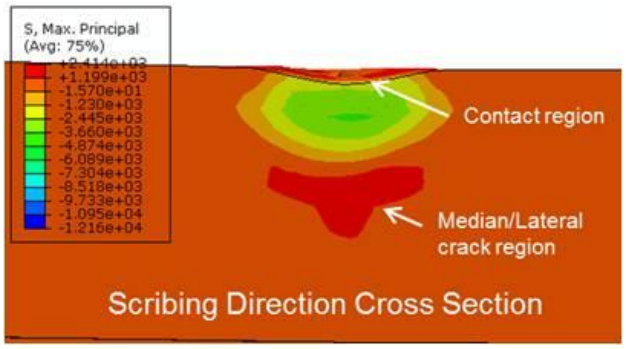

Figure 5.11: Subsurface stress contours (in a section normal to scribing direction) for a 150° conical tip and 2.6 nm scribing depth.

Fig. 5.12 summarizes the effects of the included angle on the stress and critical depth. It can be seen that the critical depth increases with the included angle. This is again due to the large compressive stresses induced in the material, which delay crack initiation and inhibit their propagation. This is consistent with results reported elsewhere for diamond turning of brittle materials with large negative rake angle tools, which exhibit ductile mode cutting behavior [36-38, 121]. The hydrostatic pressure corresponding to the critical depth ranges from 18-21 GPa, which suggests that ductile mode of cutting is dominant prior to material fracture.

Scribing by Berkovich and Vickers indenters was also studied to shed light on the cutting performance of faceted cutting grits due to their frequent appearance in diamond wires. Similar to the modeling of conical indenters presented earlier, all sharp edges in these scribers were rounded with 20 nm fillet radii and a friction coefficient of 0.05 was assumed.

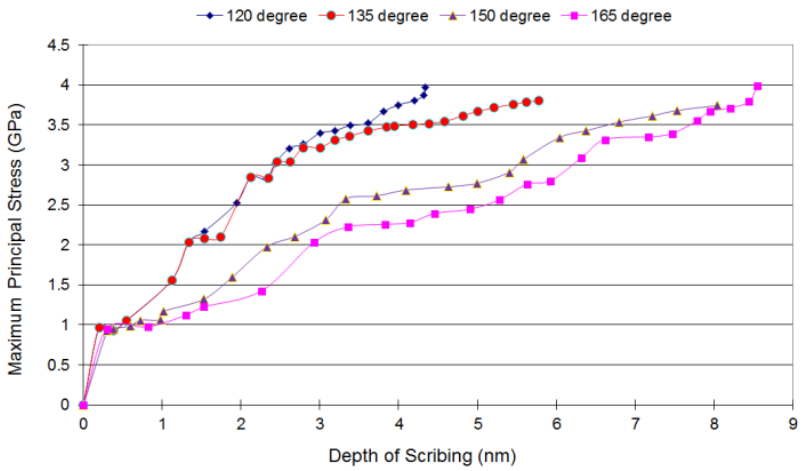

Figure 5.12: Effect of included angle and depth on stress for conical scriber.

It is found the stress distributions generated by the Berkovich and Vickers scribers exhibit the same features as the conical scriber. Namely, at a small depth of scribing the maximum principal stress is produced in the sub-surface, and the orientation of the tensile stress suggests the possible generation of median/lateral cracks. At larger scribing depths, the maximum principal stress moves to the surface of the silicon wafer. While a large tensile stress region is still produced in the sub-surface, cracks are first generated in the tensile stress region of the surface, as shown in Fig. 5.13.

Figures 5.13a and 5.13b show the geometry of scribing with the Berkovich tip. Figure 5.13a shows the scribing process with the edge of the Berkovich tip leading while Fig. 5.13b shows the face of the scriber tip leading. Note also that the Berkovich tip is modeled using shell elements instead of a solid body. It is interesting to note that the shape of the large tensile stress region and the crack formation paths are modified significantly if the tip is rotated 180 degrees around the vertical axis of the scriber (compare Figs. 5.13a, c and 5.13b, d). In both cases the large tensile stresses in the surface follow the scriber-silicon surface contact region, and the change in orientation of

the scriber tip has led to a change in the stress field, and crack initiation and propagation. The critical depth of cut in both cases is 8.9 nm.

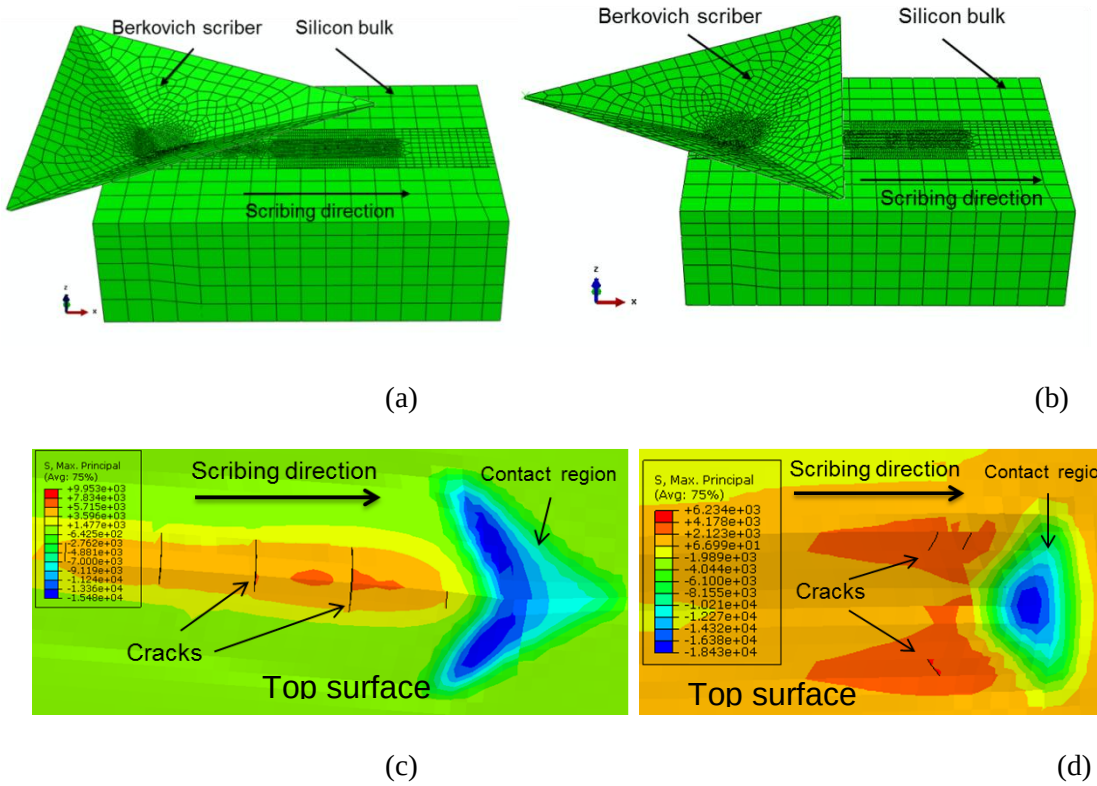

Figure 5.13: Stresses and cracks generated by Berkovich tip: edge leading (a and c) and face leading (b and d).

Similar patterns of stress distribution and crack generation are also observed for scribing with a Vickers tip (pyramidal tip with four facets). Scribing with one of the four edges of the scriber as the leading edge yields a critical depth of cut of 8.9 nm, while a slightly higher critical depth of 9.1 nm is obtained after a 45° rotation of the tip about its vertical axis. In both cases, the maximum tensile stresses occur in the sub-surface and then shift to surface as the scribing depth increases and finally surface cracks are formed.

The tensile stress in the sub-surface can be as large as 3.5 GPa. The two orientations of the scriber tip yield different maximum tensile stress distributions and crack propagation paths corresponding to the critical depths of cut for the two orientations. In actual sawing practice, due to the presence of microcracks, the fracture strength of c-Si could be lower than the 4 GPa fracture strength assumed in the XFEM model. If the fracture strength is less than 3.5 GPa, sub-surface cracks can be initiated before the generation of surface cracks.

5.3.4 Effects of Hydrostatic Pressure on Crack Initiation

It is well known that the fracture strength of a brittle material is higher when subjected to external hydrostatic pressure [122]. Single grit scribing tests on silicon carried out in a chamber with 400 MPa hydrostatic pressure have shown that crack generation in the material can be delayed, thereby allowing ductile mode cutting to be carried out at a larger scribing depth [123]. To analyze this effect using the XFEM model, scribing of monocrystalline silicon with a spherical scriber of 3 μm tip radius under different hydrostatic pressures was simulated. The results show that, for a friction coefficient of 0.05, as the hydrostatic pressure increases from zero to 800 MPa in increments of 200 MPa, the critical depth for ductile-to-brittle transition increases from 57.5 nm to 60.6 nm, 62.1 nm, 64.1 nm and 67.1 nm, respectively. The stress evolution as a function of scribing depth and the magnitude of hydrostatic pressure is shown in Fig. 5.14. This agrees with experimental observations reported in literature [123].

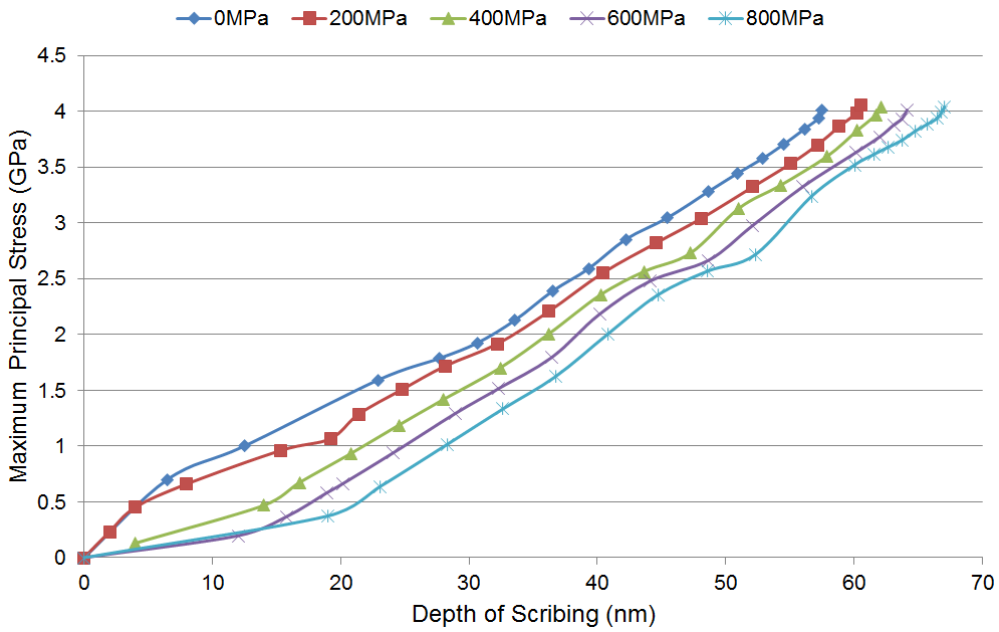

Figure 5.14: Effect of hydrostatic pressure and depth on stress for a spherical scriber (3 μm tip radius).

5.4 Summary

This chapter modeled and analyzed the effects of abrasive shape, friction coefficient, and external hydrostatic pressure on the ductile-to-brittle transition in single grit diamond scribing of monocrystalline silicon. The work was motivated by the need for fundamental understanding of the factors affecting material removal and surface generation in fixed abrasive diamond wire sawing of PV silicon wafers. An XFEM model of the single grit scribing process was built and shown to yield predictions of the critical depth of cut for ductile-to-brittle transition for silicon that are in reasonable agreement with diamond scribing experiments.

The modeling results show that ductile mode cutting, which yields a smooth crack-free surface, can be induced by suitably controlling abrasive shape parameters such

as the grit tip radius (for spherical abrasives) and included angle (for conical abrasives). Increasing the tip radius and/or the included angle increases the critical depth by delaying crack initiation in silicon. In contrast to blunt tips (flat and spherical), which only initiate surface cracks at the ductile-to-brittle transition point, sharp tips (conical, Berkovich and Vickers) always generate large tensile stress regions in the subsurface, which lead to the initiation of median and lateral cracks.

In addition, lowering the friction coefficient, e.g. by altering the cutting fluid properties in the actual wire sawing process, also yields a higher critical depth of cut. The model also correctly captures the increase in critical depth of cut with increasing hydrostatic pressure.

It is noted that a higher critical depth of cut implies the possibility of a higher feed rate in wire sawing without surface/subsurface cracking. These results are expected to be useful in optimizing the diamond wire and its application to wafering of PV silicon ingots.

CHAPTER 6

EFFECTS OF CARBIDE AND NITRIDE INCLUSIONS ON DIAMOND SCRIBING OF MULTICRYSTALLINE SILICON

In this chapter, single grit diamond scribing experiments were carried out to understand the effects of SiC and Si_3N_4 inclusions on cutting of photovoltaic multicrystalline silicon (mc-Si) substrate material. Explanations for the observations are given based on the material properties of mc-Si, diamond and inclusions. The detrimental effects of SiC and Si_3N_4 inclusions on diamond wire sawing are also discussed.

6.1 Introduction

Currently multicrystalline silicon (mc-Si) based solar cells make up more than half of the worldwide photovoltaic (PV) market. Unlike monocrystalline silicon materials, mc-Si has a higher density of defects and impurities [1]. The occurrence of SiC and Si_3N_4 inclusions in mc-Si has been reported by a number of researchers. Søiland et al. [67] identified the inclusions as β-SiC and β-Si_3N_4 and proposed that the nitrides act as nucleation centers for carbide precipitation. Due to their detrimental effects on cell efficiency, the electrical properties of SiC particles and filaments have been studied extensively [124]. Möller et al. [125] introduced two different approaches to explain the growth of SiC filaments. More recently, Lotnyk et al. [126] studied SiC particles and filaments using transmission electron microscopy (TEM). Their study showed that SiC particles are monocrystalline while SiC filaments are microcrystalline. They also

confirmed that both are β-SiC. Bakowskie et al. [127] developed a method for detecting SiC and β-Si_3N_4 precipitates and filaments.

It is known that the presence of SiC and Si_3N_4 inclusions can have a detrimental effect on the wire sawing process used to produce mc-Si substrates for solar cells. Du et al. [8, 69-70] studied the sawing ridges caused by the inclusions in multi-wire slurry sawing and suggested that SiC was the main cause for sawing defects, while the influence of Si_3N_4 was not noticeable. However, their conclusions were made from observations of the surface morphology of as-cut wafers and without investigation of the actual interaction between the abrasive, inclusions and substrate material during cutting/sawing.

In this chapter, the possible effects of SiC and Si_3N_4 inclusions in the diamond wire sawing process are investigated through fundamental single grit diamond scribing experiments performed on mc-Si substrate material.

6.2 Experiments

In order to gain a fundamental understanding of the role of carbide and nitride inclusions in diamond wire sawing, single grit diamond scribing studies on ~2mm thick as-cast mc-Si substrates were carried out. The experimental setup consists of a diamond scriber and a mc-Si sample with a high density of carbide and nitride inclusions mounted on a 3-component piezoelectric cutting force dynamometer (Kistler 9257B), which sits on stacked X-Y-Z precision motion stages (Aerotech ANT-4V, Z-axis resolution is 1 nm) as shown in Fig. 4.2. The diamond scribers have the conical shape with 90˚ included angle and the tip radius is measured to be 5~10 μm.

The following inclusions were found to be present in the mc-Si samples used in the study: SiC filaments, hexagonal Si_3N_4 rods and Si_3N_4 fibers. No SiC particles were found. The morphology of the inclusions before and after scribing was observed in a scanning electron microscope (SEM, Hitachi VP S3700) while the chemical compositions of the inclusions were identified using X-ray energy dispersive spectroscopy (EDS, Oxford Inca). The hardness of the inclusions was measured using a triboindenter (Hysitron) with a Berkovich tip. The indentation loads applied were 6000 ~ 9000 μN.

The SiC filaments, Si_3N_4 rods and Si_3N_4 fibers and their locations on the mc-Si sample were identified using the SEM. Afterwards, the inclusions were scribed using the diamond scriber.

6.3 Results

The SEM image in Fig. 6.1(a) shows a hexagonal Si_3N_4 rod surrounded by two SiC filaments. The surface morphology of this area after diamond scribing is shown in Fig. 6.1(b). It can be seen that the interaction between the diamond scriber and the Si_3N_4 rod is catastrophic and results in considerable localized brittle fracture of the mc-Si substrate in the immediate vicinity of the nitride inclusion. The SiC filament on the right of the Si_3N_4 rod in Fig. 6.1(a) is partially cut through. Also, the debris near the residual SiC filament suggests that ductile mode cutting of the filament occurred. The second SiC filament immediately below the Si_3N_4 rod in Fig. 6. 1(a) is chipped-off completely by the severe cracking of the mc-Si matrix caused by the interaction.

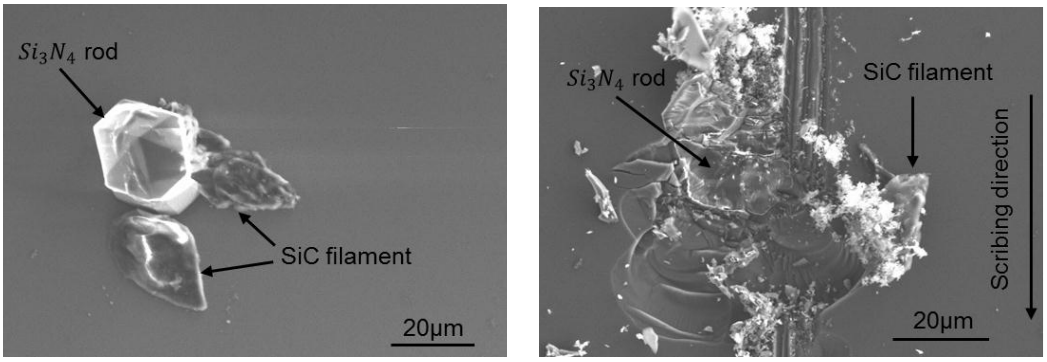

(a) (b)

Figure 6.1: SEM images of Si_3N_4 rod and SiC filament inclusions (a) before and (b) after diamond scribing.

It is known that the mode of cutting (ductile vs. brittle) in wire sawing plays a significant role in determining sawing productivity and the mechanical strength of the Si wafers produced [128-129]. In fact, evidence of more ductile mode cutting has been observed in diamond cut wafers than in slurry cut wafers [104]. As seen in Figs. 6.2(a) and 6.2(b), the cutting mode before and after interaction of the scriber and inclusion is mostly ductile. However, the presence of the silicon nitride inclusion leads to large scale brittle fracture in mc-Si, which generates severe cracking, as seen in Fig. 6.1(b).

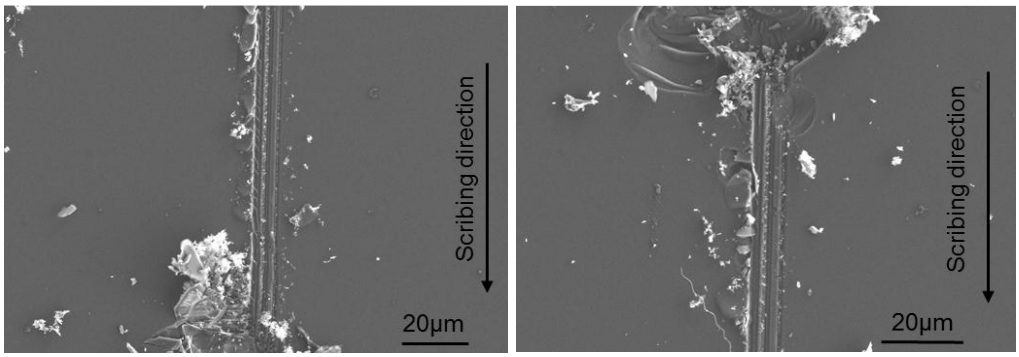

(a) (b)

Figure 6.2: Cutting mode before and after diamond scribing in the vicinity of inclusions shown in Fig. 6.1.

The measured scribing forces for the scribing test in Fig. 6.1(b) are shown in Fig. 6.3. The normal and tangential forces refer to the measured force components normal to the substrate and along the scribing direction, respectively. The out-of-plane force is the force component orthogonal to the normal and tangential forces and is considerably smaller in magnitude. There is a significant increase in the force magnitude of all three force components at the location of the nitride inclusion. After the increase, there is an abrupt drop in the forces to almost zero force. The drop is believed to be caused by crack propagation resulting from the scriber-inclusion interaction, which results in complete removal of the cracked area from the mc-Si matrix (see Fig. 6.1(b)).

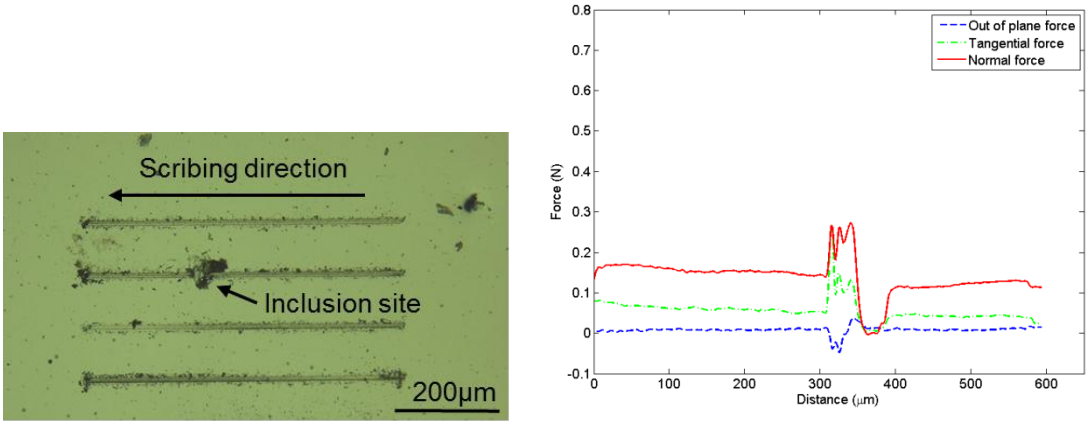

Figure 6.3: Measured scribing forces.

In another case of scribing across a Si_3N_4 rod (see Fig. 6.4(a)), the severe interaction between the diamond scriber and the Si_3N_4 rod causes a deviation in the scribing track, as seen from the displaced location of the track relative to its location prior to the interaction. The normal force during scribing (see Fig. 6.4(b)) is seen to increase by more than three times its value in the absence of inclusions.

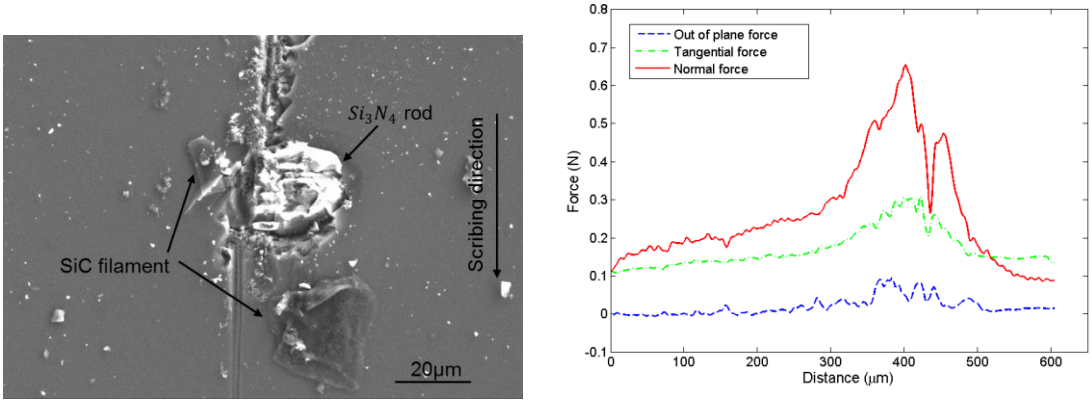

(a) (b)

Figure 6.4: Scribing through Si_3N_4 rod and measured forces.

An area on the substrate containing SiC filaments was identified and is shown in Fig. 6.5(a). Two tracks, S1 and S2, were made, as seen in Fig. 6.5(b). It can be seen that ductile mode of cutting persists even in the locations of the SiC filament, as indicated by the characteristic form of debris. The corresponding force measurements in Fig. 6.6 do not show the large variation observed in the case of the silicon nitride rod inclusion.

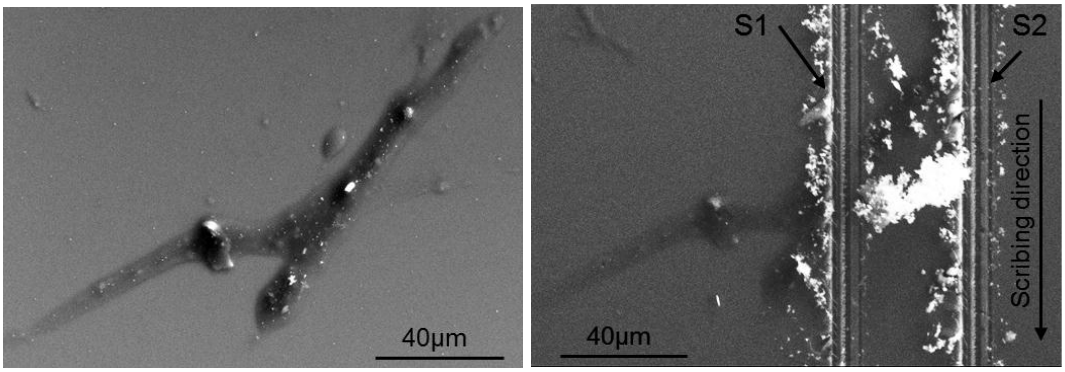

(a) (b)

Figure 6.5: Scribing of SiC filament.

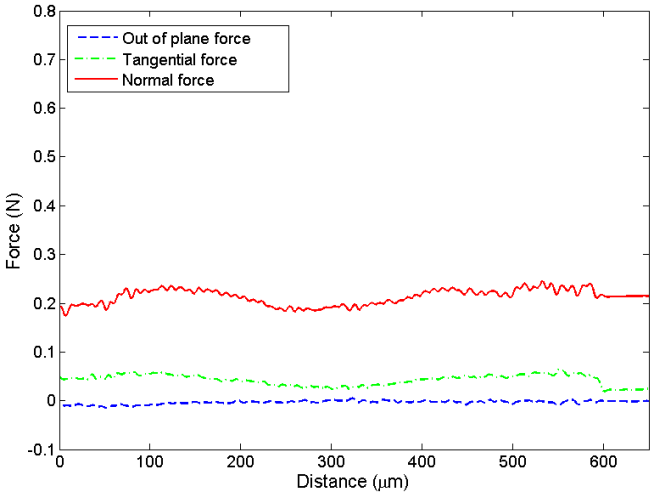

Figure 6.6: Measured forces during scribing across the SiC filament (S1).

Si_3N_4 fibers are also frequently observed in mc-Si samples. As shown in Fig. 6.7(a), Si_3N_4 fibers typically have widths of only a few micrometers but their lengths can be hundreds of micrometers or even millimeters. These fibers cannot be cut through even when the depth of scribing is large, which causes severe cracking in the mc-Si matrix, as seen in Fig. 6.7(b). In fact, the majority of fibers maintain their form and location after scribing. The corresponding force measurements do not reveal any impact of the fibers and are therefore not shown here.

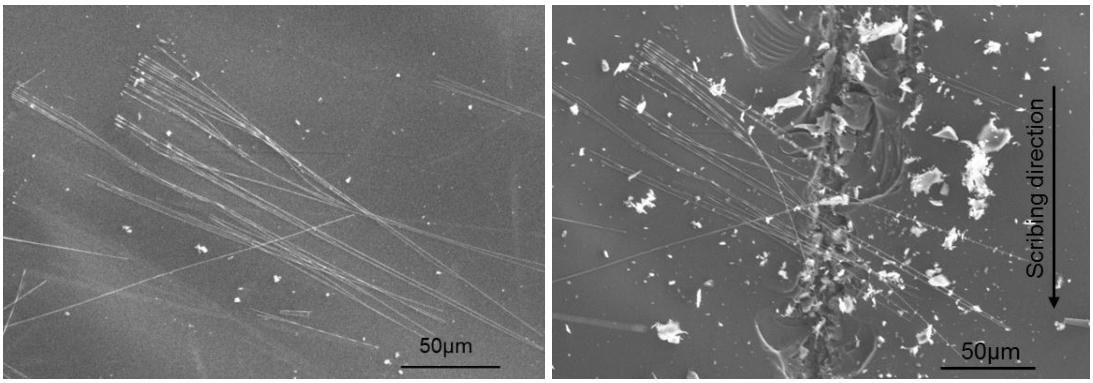

(a) (b)

Figure 6.7: Si_3N_4 fibers before and after scribing.

6.4 Discussion

It has been confirmed by other researchers that the SiC and Si_3N_4 inclusions in mc-Si are β-SiC and β-Si_3N_4, respectively [67, 126]. The hardness of the mc-Si matrix and the inclusions investigated in this work were measured using nano-indentation (Hysitron triboindenter) and are listed in Table 6.1. The hardness of diamond, fracture toughness of single crystal Si along different orientations, and the fracture toughness of β-SiC and β-Si_3N_4 from the literature are also listed. Note that both the SiC filaments and Si_3N_4 rods in the test samples have a lower hardness than those reported in literature [130-133]. The hardness values reported in literature were typically measured on polycrystalline forms of β-SiC and β-Si_3N_4 manufactured using either chemical vapor deposition (CVD) or hot-pressing. In contrast, the growth mechanisms of β-SiC and β-Si_3N_4 in the mc-Si substrate used in the current study are quite different from their CVD/hot-pressed counterparts and therefore their microstructure and hardness can differ significantly.

Table 6.1: Material properties of Si, SiC Filament, Si_3N_4 rod and diamond.

	Hardness (GPa)	Fracture toughness (MPa$\sqrt{m}$)
mc-Si substrate	11.60 ± 0.39	0.78-1.31 [130]
SiC filaments (β-SiC)	10.54 ± 1.25	2.4-5.1 [131]
Si_3N_4 rods (β-Si_3N_4)	11.99 ± 0.23	4.0-6.6 [132]
Diamond	60-120 [133]	7-8.4 [133]

The β-Si_3N_4 rods measured in this work are β-phase hexagonal single crystals, thus justifying their lower hardness than the hot-pressed polycrystalline β-Si_3N_4 reported in the literature. Nevertheless, the average hardness of the β-Si_3N_4 rods in the samples used in this study are slightly higher than the mc-Si substrate The difference in the

average hardness of the β-Si_3N_4 and mc-Si matrix can possibly explain the observations made when scribing through the Si_3N_4 rods. Since the depth of scribing was kept almost constant in the experiments, an increase in cutting force is expected at the location of the Si_3N_4 rod due to its higher hardness. Moreover, 3D confocal microscope images reveal that the Si_3N_4 rods typically protrude 1-5 μm from the mc-Si substrate surface. The height increase can also lead to the increase in the observed cutting force. Meanwhile, severe brittle fracture was observed in the mc-Si substrate but no cracking was observed in the Si_3N_4 rod due to its larger fracture toughness compared to Si (see Table 6.1). In addition, the diamond scriber tip did not exhibit any fracture after the experiments.

The large normal force observed in the scribing of silicon nitride rods suggests that the presence of hard inclusions can lead to bending and possibly breakage of the wire in the slurry sawing operation due to the impact force between the diamond abrasive embedded in the wire and the protruding inclusion [8, 69-70]. In addition, the large increase in tangential force can cause diamond grit fracture and potentially wire breakage in the actual diamond wire sawing process. The diamond grits electroplated or resin-bonded to the stainless steel wire have a rough interface and the application of tangential force can induce stress concentrations at the interface leading to microcrack propagation and finally breakage of the wire. It should be noted that the scribing speed used in this study is significantly lower (1 mm/min) than the wire speeds (5~20 m/s) used in industrial wire sawing. Consequently, the forces measured here are most likely much lower than those experienced by the grits and wire in the actual process. This is believed to be the reason for the absence of fracture of the diamond scriber in the current study.

Unlike the slurry sawing operation where material removal is achieved by three-

body abrasion (wire, SiC cutting grits and Si matrix), diamond wire sawing removes materials through a two-body wear (diamond grits and Si matrix) process. As the diamond grits are directly attached to the steel wire, the severe impact of the diamond abrasive and the hard inclusions and the sudden increase in cutting force is transferred directly to the wire, which makes it more susceptible to breakage than the wire in slurry sawing.

It is of interest to note that the SiC filaments did not affect the diamond scribing process (as seen from the force measurements) and the resulting surface morphology, especially given that the hardness of β-SiC reported in literature is significantly higher than the hardness of Si. A recent transmission electron microscopy (TEM) study has shown that SiC filaments have a different microcrystalline structure than SiC particles [126]. Specifically, it was shown that there is a high density of planar defects in the SiC filaments, which are thought to contribute to its lower hardness given in Table 6.1. The hardness of SiC filaments is close to that of the mc-Si substrate and therefore scribing across the SiC filaments does not cause abrupt change in the measured forces.

6.4 Summary

Single grit diamond scribing experiments were carried out to fundamentally understand the effects of SiC and Si_3N_4 inclusions on diamond wire sawing or cutting of photovoltaic multicrystalline silicon (mc-Si). Results show that hexagonal rod-type Si_3N_4 inclusions significantly increase the cutting force and lead to localized brittle fracture of the mc-Si substrate. The increase in cutting force is due to the inhomogeneity of material properties caused by the presence of rod-type Si_3N_4 inclusions. In contrast, SiC filament-

type inclusions do not affect the scribing/cutting process due to reduced hardness caused by the high density of planar defects in its microcrystalline structure. Si_3N_4 fibers are found to be flexible and are not cut by diamond scribing.

CHAPTER 7

INFLUENCE OF DISLOCATIONS ON THE MECHANICAL PROPERTIES AND CUTTING BEHAVIOR OF MULTICRYSTALLINE SILICON

This chapter studies the influence of dislocations generated during solidification on the mechanical properties and cutting behavior of multicrystalline silicon (mc-Si) material used in solar cells. Experiments have been carried out to measure the elastic modulus, hardness, and fracture toughness as a function of dislocation density variations in different regions of the same crystallographic grain. The results show that the presence of dislocations does not alter the elastic modulus or hardness significantly. However, regions of the same grain with higher dislocation density are characterized by higher fracture toughness. The influence of dislocation density on the cutting behavior of mc-Si in the single grit diamond scribing is also investigated.

7.1 Introduction

Industrial diamond wire sawing experience suggests that single crystal Si (sc-Si) ingots can be cut efficiently whereas significant challenges remain in the economic application of this process to cut multicrystalline Si (mc-Si) ingots. Unlike single crystal silicon, mc-Si has a higher density of defects and impurities [1, 8, 66]. As a major type of crystalline defect, dislocation clusters are widely known as recombination centers and therefore negatively impact the solar cell efficiency [71-72]. While its detrimental effect

on the electrical properties of silicon materials are well understood, the influence of dislocations on the mechanical properties and the resultant cutting performance of mc-Si during wafering are still not clear.

At temperatures above the brittle-to-ductile transition of crystalline silicon, it was found that interstitial oxygen and nitrogen atoms can cause locking of dislocations, which increases the strength of the silicon crystal [74-76]. In addition, crack tip shielding can be induced by crack tip dislocation multiplication in the same temperature range [77-79]. It is known that dislocations can also be generated in crystalline Si at room temperature under extreme loading conditions such as those encountered in indentation and scribing [80-82]. Evidence has shown that dislocation plasticity without phase transformation can be generated by nanoindentation at room temperature [81]. Wire sawing of silicon wafers typically does not involve very high temperatures. Therefore, an understanding of the influence of dislocations on the mechanical properties and cutting behavior of mc-Si at room temperature is necessary in order to shed light on its behavior during indentation and scribing processes.

7.2 Experimental Method

Experimental work has been carried out to investigate the effects of dislocation density on the hardness and fracture toughness of multicrystalline silicon material. Six sister wafers of thickness ~750 μm obtained from a mono-like cast ingot are selected for the experiments. Due to the directional solidification process of the multicrystalline ingot, the grain structures of the sister wafers are identical. One side of the wafers was mirror polished by removing 25-50μm of material in order to eliminate the influence of the

sawing process after crystal growth. Measurements were made on the polished side of the wafers. The dislocation etch pit density in the wafers was revealed through a Yang etching [134]. The wafers at the top and bottom of the sister wafer group were etched to confirm that the dislocation etch pit density distribution in all six sister wafers are identical. A large grain covering half of the wafer surface area was identified for evaluation of the mechanical properties. The crystallographic plane of the grain is identified using X-ray diffraction (Philips Pananalytical XRD) to be (100). In this grain, three regions of varying dislocation etch pit density (low, medium and high) were selected for evaluation (see Fig. 7.1). The dislocation etch pit images agree with those identified as dislocations in literature [134] and reproduced in Fig. 7.1(d).

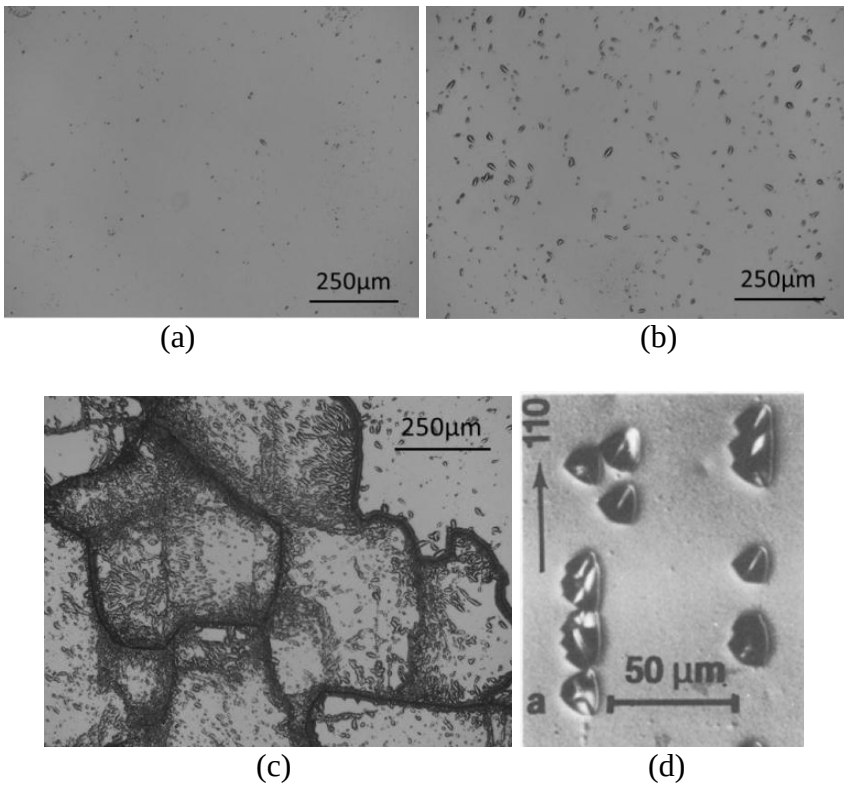

Figure 7.1: Regions with varying dislocation etch pit densities: low (Region I, a), medium (Region II, b), high (Region III, d) and dislocation etch pits reported in literature (d, [134]).

Another grain located adjacent to the (100) grain was measured to be a (311) grain. As seen in Fig. 7.2, across the grain boundary, the dislocation etch pit density is high in the (311) grain whereas the dislocation etch pit density in the (100) grain is similar to that in Region I in Fig. 7.1.

The high dislocation areas close to the grain boundary in (311) are identified as Region IV whereas a region with lower dislocation etch pit density in the (311) grain is identified as Region V. The dislocation etch pit densities in these two regions are shown in Fig. 7.3.

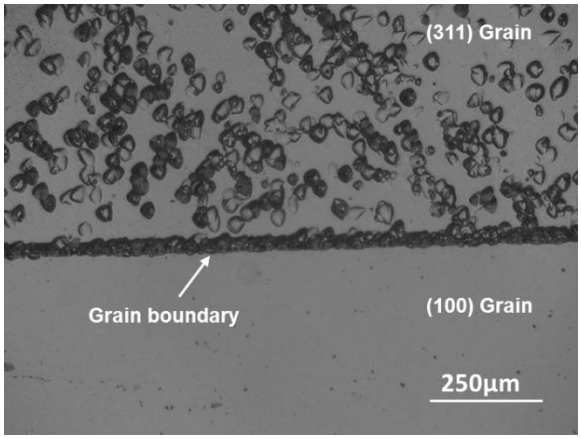

Figure 7.2: (311) and (100) grain dislocation contrast.

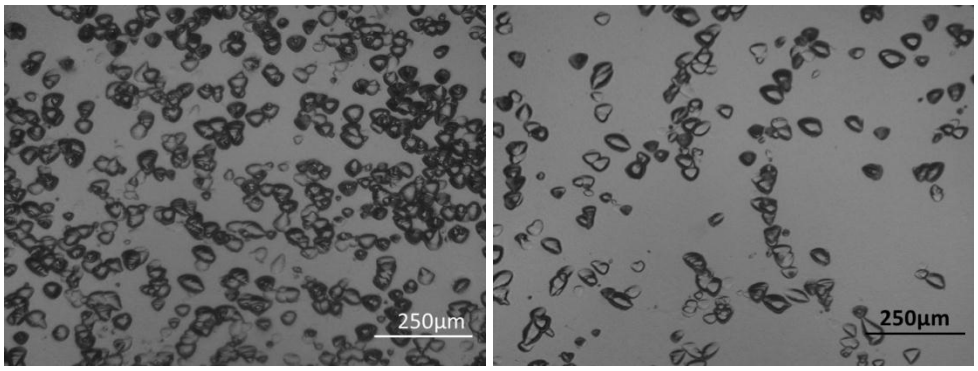

Figure 7.3: Regions with different dislocation etch pit densities in the (311) grain: high (Region IV, left), high (Region V, right).

Nanoindentation is widely used to characterize the mechanical properties of Si and other ceramics [135, 136]. In this study, a triboindenter (Hysitron) with a Berkovich tip was used to measure the elastic modulus and hardness in the regions of different dislocation density. To obtain statistical significance, six sets of 4x4 measurements were made in each region. The 16 indents in each of the six sets of measurements were located 300μm apart from each other.

Fracture toughness plays a significant role in determining the cutting performance of Si. The indentation method has been shown to be effective in evaluating the fracture toughness of brittle materials [28, 137-138]. A microhardness system (Buehler) equipped with a standard Vickers diamond indenter was used in this study to measure the fracture toughness. A series of indents were made with a load of 500mg. The radial crack length c and indent size a were measured using an optical microscope (Keyence VHX-600). A representative picture of the indentation cracks obtained is shown in Fig. 7.4.

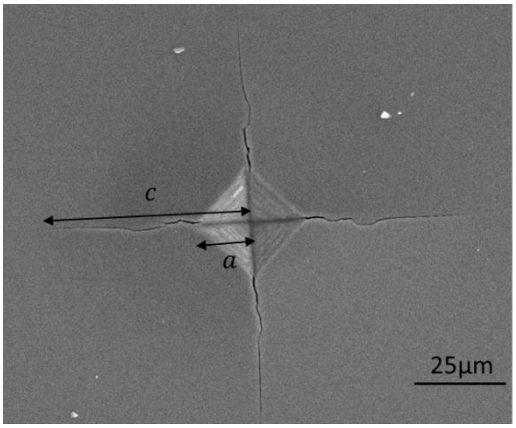

Figure 7.4: Indentation method to measure fracture toughness.

The fracture toughness, K_{Ic}, is calculated from the following relationship using a, c and the average values of E and H [138]:

$$K_{Ic} = 0.129\left(\frac{c}{a}\right)^{-\frac{3}{2}}\left(\frac{\varphi E}{H}\right)^{\frac{2}{5}}(Ha^{\frac{1}{2}}/\varphi) \quad (7.1)$$

where φ is a constraint factor (φ~3), E is Young's modulus and H is the hardness.

As presented in previous chapters, silicon exhibits ductile behavior when cut at low feed rates. Fig. 7.5 shows the typical cutting mode transition with increasing cutting depth in single grit diamond scribing experiments performed in the (100) grain under ambient conditions. The diamond scriber used is conical in shape with a 90˚ included angle. The tip radius was measured to be ~10μm. The setup shown in Fig. 4.2 was used for experiments.

Single grit diamond scribing experiments were carried out in the three regions of varying dislocation density along the same orientation and the critical depth of cut for ductile-to-brittle transition was measured using a confocal microscope (Olympus LEXT 3D).

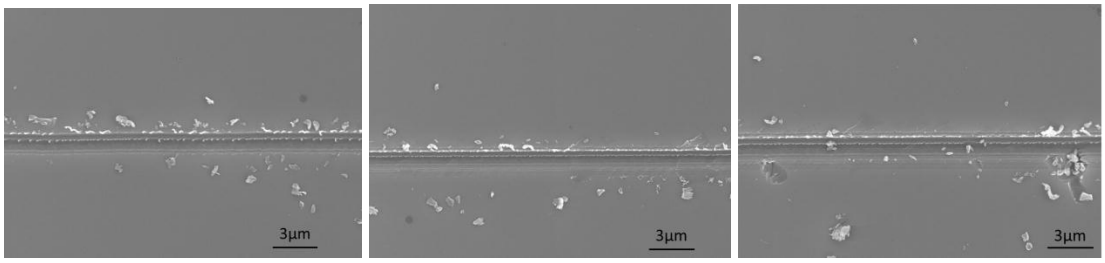

Figure 7.5: Surface morphology produced in diamond scribing of Region I at depths of 0.157 μm (left), 0.253 μm (middle), and 0.382 μm (right).

In the brittle fracture regime, the specific scribing energy represents the energy required to remove unit volume of material via fracture. The specific scribing energy is computed as follows:

$$SSE = \frac{F_c l}{V} \quad (7.2)$$

where F_c is the cutting force acting in the direction of the scribing velocity, l is the scribing length, and V is the volume of material removed.

Single grit diamond scribing experiments were carried out in the low, medium and high dislocation density regions of the (100) grain to determine the specific scribing energy. In each region, the nominal depth of cut was varied from 2 to 5 μm. Fifteen (15) scribing tests were carried out at each nominal depth. The scribing length was fixed at 300 μm and the cutting force was measured using the Kistler 9257B 3-component piezoelectric dynamometer. The volume removed was measured using the LEXT 3D confocal microscope. A representative scribe is shown in Fig. 7.6. It can be seen the material is removed primarily by severe brittle fracture.

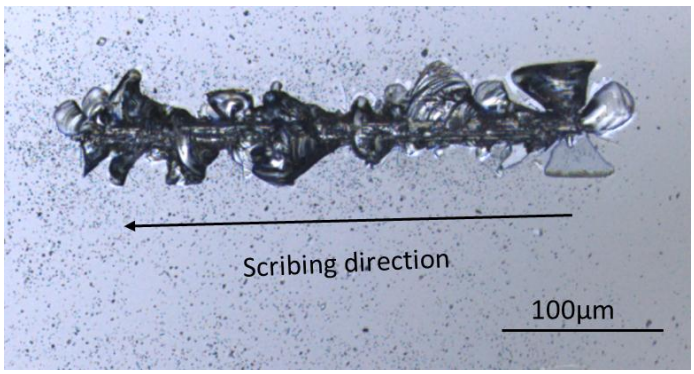

Figure 7.6: Single grit diamond scribing in the brittle fracture regime (4 μm nominal depth of cut).

7.3 Results and Discussion

The measured hardness and elastic moduli are shown in Table 7.1 and the fracture toughness measurements are presented in Fig. 7.7.

Table 7.1. Elastic modulus and hardness results.

	Modulus (GPa)	Hardness (GPa)
Region I	157.2 ± 3.3	11.8 ± 0.2
Region II	160.6 ± 2.8	11.9 ± 0.2
Region III	159.4 ± 2.2	12.2 ± 0.2
Region IV	175.6± 3.7	11.8 ± 0.3
Region V	174.6 ± 6.1	11.5 ± 0.7

It is seen that the hardness and elastic moduli do not vary much in the (100) three regions while the fracture toughness exhibits an increase of up to ~30% from the low to the high dislocation density region (1.122 ±0.088 to 1.491± 0.109MPa$\sqrt{m}$). The hardness and elastic moduli also do not vary significantly in the (311) grain whereas the fracture toughness is higher in Region IV than Region V (1.413 ±0.112 to 1.275± 0.071MPa$\sqrt{m}$). The fracture toughness is defined as [94]:

$$K_{(I,II,III)C} = Y\sigma\sqrt{\pi a} \tag{7.3}$$

where σ is the applied tensile stress, a is the characteristic crack dimension and Y is a dimensionless constant that depends on the geometry and loading mode. Under the same scribing conditions, areas with larger fracture toughness will require higher applied tensile stress to cause fracture. A larger depth of scribing will lead to a larger tensile stress. Assuming that the microcrack length and density are uniform in the (100) and (311) grains, region III and Region IV, which have larger fracture toughness, should yield a higher critical depth of cut for ductile-to-brittle transition than regions I and II, and Region V, respectively. This is confirmed by the critical depth measurements obtained from the scribing tests (see Fig. 7.8).

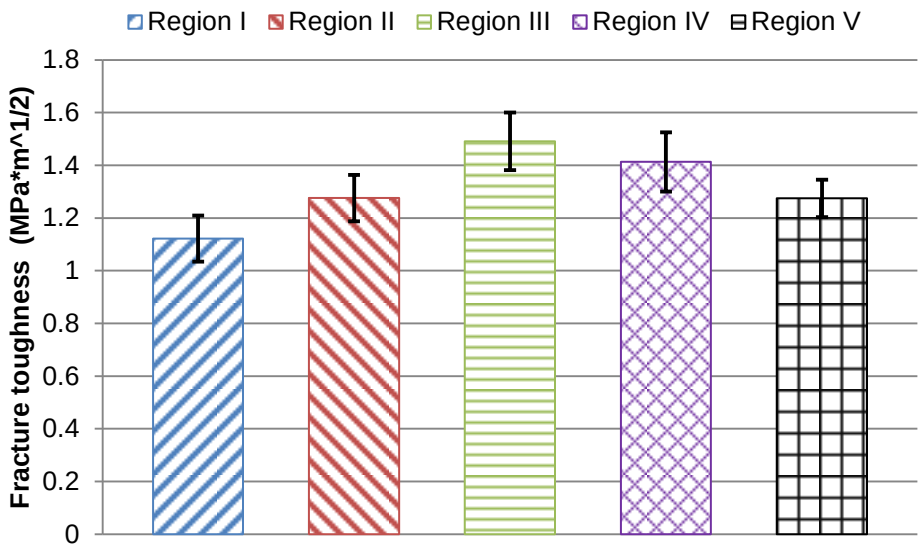

Figure 7.7: Fracture toughness in the three regions.

At temperatures above the brittle-to-ductile transition in silicon crystals, it has been shown that dislocations around the crack tip entangle and the resultant multiplication of dislocations can lead to crack tip shielding [74-76]. Crack tip shielding can cause the fracture toughness to be higher. Even at ambient temperature, direct evidence for micro-plastic fracture in single crystal Si has been observed by Wu and Xu [139]. High-resolution transmission electron microscopy (HRTEM) analysis reported by Wu and Xu shows the generation of dislocations at the crack tip, which indicates the occurrence of micro-plasticity during crack propagation. Based on these findings reported in the literature, it is likely that the increase in fracture toughness in the higher dislocation density region of the mc-Si observed in this study is due to crack tip shielding caused by the interaction of dislocations around the crack tip.

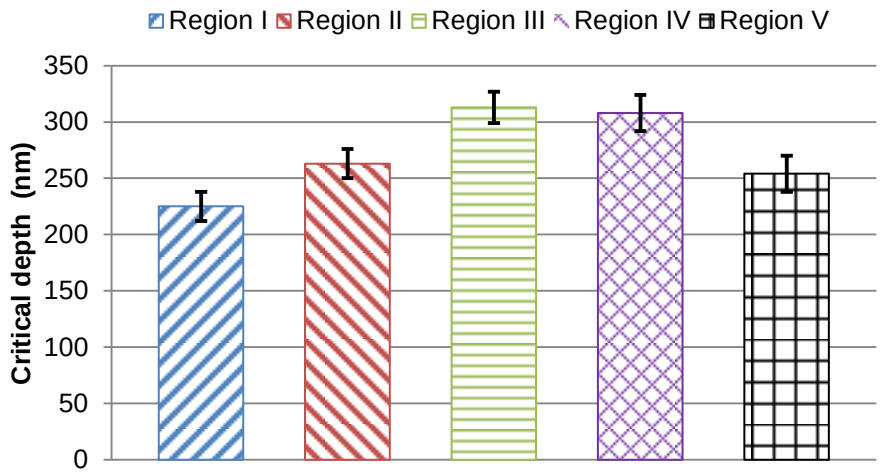

Figure 7.8: Critical depth of cut for ductile-to-brittle transition.

Due to the higher fracture toughness, more energy is required to remove material through brittle fracture in the high dislocation density region, as shown in Fig. 7.9. As the depth of cut increases, a decrease in specific scribing energy can be seen for all the three regions due to the well-known size effect [140]. At nominal depths of cut ranging from 2 to 5 µm, the average specific scribing energy is largest in Region III and smallest in Region I.

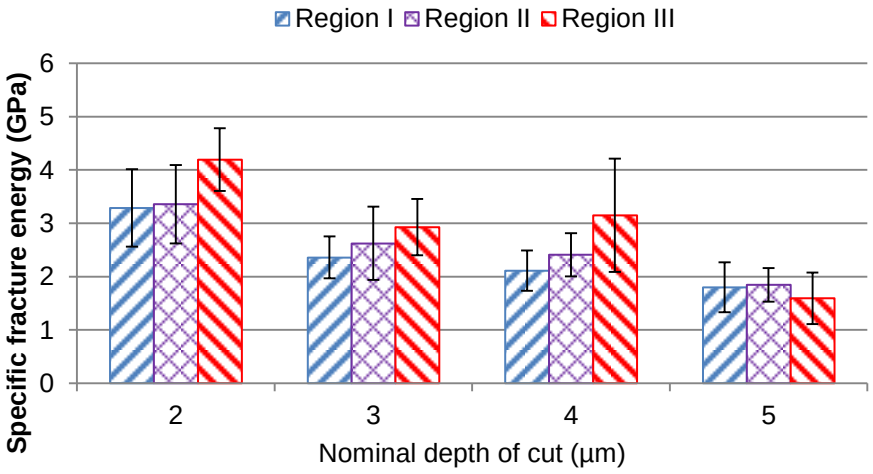

Figure 7.9: Specific scribing energy in regions I, II and III.

Single grit diamond scribing experiment was also carried out to scribe across the grain boundary between the (311) and (100) grains at a speed of 2mm/min. The scribing direction is perpendicular to the grain boundary, which is nearly a straight line (see Fig. 7.2). With a nominal depth of cut of 500nm, a representative cutting force measurement is shown in Fig. 7.10. The large fluctuation in magnitude is due to brittle fracture. It is found that after the grain boundary, there is a decrease in the magnitude of both the normal and tangential force components when scribing in the (100) grain, compared to scribing in the (311) grain. The average tangential and normal forces (15 tests) in the (311) grain are 0.147 N and 0.129N whereas those for the (100) grain are 0.085N and 0.116N. This is due to the larger elastic modulus in Region IV than Region I (175.63± 3.72 GPa vs. 157.17 ± 3.32 GPa, see Table 7.1). Given the same depth of cut as the displacement loading condition, scribing in the region with higher elastic modulus will require a higher cutting force. This indicates that the cutting force can vary when cutting across the grain boundary during diamond wire sawing. The cutting force variation can possibly lead to dynamic vibration of the sawing system and thereby sawing defects (saw marks, surface/subsurface damage).

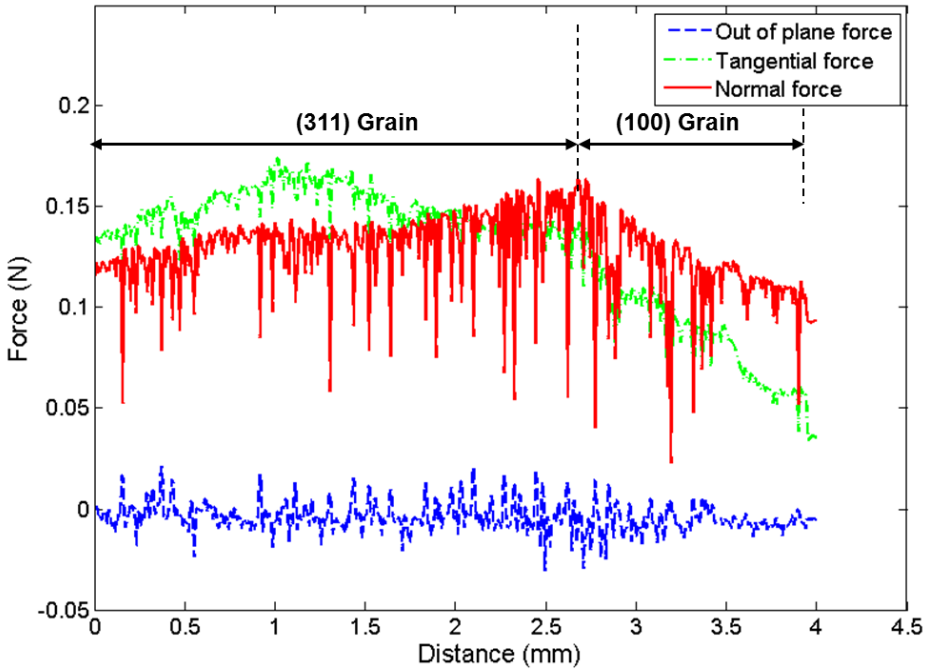

Figure 7.10: Scribing forces across the (311) and (100) grains.

7.4 Summary

This chapter analyzed the influence of intra-grain dislocation density variations on the mechanical material properties and cutting behavior of mc-Si material used for solar cells. Specifically, the effects of dislocation density variations in the (100) and (311) grains of a mono-like cast mc-Si material on the elastic modulus, hardness, fracture toughness, critical depth of cut for ductile-to-brittle transition and specific scribing energy were evaluated. Experimental results show that the dislocation density variations in the grain do not alter the elastic modulus or hardness significantly. However, regions with high dislocation density exhibit higher fracture toughness than regions of lower dislocation density. Single grit diamond scribing experiments show that the high dislocation density region yields a higher critical depth of cut for ductile-to-brittle transition, which implies that the material in this region will exhibit more ductile mode

cutting behavior. Due to material anisotropy, scribing across the grain boundary leads to variation in the cutting force, which can cause detrimental effects in the sawing process. The increase in fracture toughness is also found to be correlated with higher specific scribing energy in the brittle scribing regime. The observed correlation between the dislocation density and fracture toughness are thought to result from crack tip shielding arising from the interactions of dislocations with the crack.

CHAPTER 8

CONCLUSIONS AND RECOMMENDATIONS

This chapter summarizes the major conclusions of this thesis and suggests related areas for further investigations.

8.1 Major Conclusions

The major conclusions are as follows:

8.1.1 Analysis of Slurry and Fixed Abrasive Diamond Sawn Silicon Wafers

Silicon wafers cut by slurry sawing and fixed abrasive diamond wire sawing were analyzed and the key conclusions are:

- The surface morphology of slurry and diamond cut wafers are quite different. Slurry cut wafer surface has randomly distributed microcracks whereas the diamond cut wafers have cutting grooves in the cutting direction. The residual stresses (maximum shear stress) in diamond cut wafers follow the pattern of the cutting grooves.
- Slurry sawn wafers have a characteristic pattern of wafer thickness and surface roughness while diamond cut wafers do not. In slurry cut wafers, the surface roughness decreases and the wafer thickness increases along the wire travelling direction.
- Microcracks are present in both the wafer edges and center of slurry and diamond cut wafers. Edge cracks are generally longer than center cracks.

Slurry sawn wafers have lower crack density but larger characteristic microcrack length than diamond cut wafers.

- Breakage of silicon wafers is due to mixed mode fracture. Crack orientation has significant effect in four line bending but not in a biaxial bending test. The fracture strength in four line and biaxial bending correlate well with crack lengths determined from Linear Elastic Fracture Mechanics (LEFM). In general, diamond cut wafers are at least as strong as slurry sawn wafers when bent perpendicular to the saw marks.

8.1.2 Effects of Crystallographic Orientation on Ductile Scribing of Silicon

Experimental studies were carried out to understand the influence of anisotropy on the ductile mode of cutting of single crystal silicon. An explanation of the experimental observations based on phase transformation and slip generation was proposed. The following conclusions were derived from this study:

- (100) wafer is more prone to brittle fracture than others and (111) wafer exhibits the highest ductile cutting capability.
- <100> orientations are more likely to exhibit brittle fracture than other orientations in the same crystal plane and the <111> direction tends to have more ductile morphology under the same scribing conditions.
- Scribing velocity does not appear to have a significant effect on the ductile-to-brittle transition for the velocities and directions tested.
- The experimental results are explained by the roles of phase transformation and slip generation in the substrate. For a given scribing depth, orientations for which slip systems are easily activated require higher load and therefore

produce higher tensile stress in the material, which leads to increased brittle fracture and lower critical depth of cut.

8.1.3 Study of Ductile-to-brittle Transition in Single Grit Diamond Scribing of Silicon

XFEM modeling and analysis of the ductile-to-brittle cutting mode transition in single grit diamond scribing of single crystal silicon was carried out. After the validation of the XFEM models, the modeling study yields the following key conclusions were obtained:

- Larger scriber tip radius yields higher critical depth of cut, which indicates more ductile model cutting and therefore fewer microcracks.
- Blunt indenters such as punch and spherical indenters tend to generate only surface cracks, while sharp indenters (e.g. conical, Vickers and Berkovich) can generate subsurface cracks. Sharper indenters or indenters with smaller rake angle generate large tensile stresses and pressures under the same cutting conditions, which lead to smaller critical depth of cut for crack generation and hence reduced capability for ductile mode of cutting.
- Before cracks are generated, the hydrostatic pressure generated is large enough to cause phase transformation from silicon from the diamond cubic phase to a metallic β-Sn phase and therefore the ductile cutting mode dominates before crack generation.
- Friction has a significant effect on ductile-to-brittle cutting mode transition. Higher friction yields a smaller critical depth of cut and hence reduced ductile mode of cutting.

8.1.4 Effects of Hard Inclusions on Diamond Scribing of Multicrystalline Silicon

An experimental study of the influence of SiC and Si_3N_4 inclusions on the diamond scribing of mc-Si was carried out and the key observations were as follows:

- Presence of Si_3N_4 inclusions can lead to severe cracking in the silicon matrix and thereby higher damage level.
- SiC filament will not cause sawing challenges because of small hardness, which is due to defects in its microstructure.
- Si_3N_4 fibers are very flexible and are not cut through by the diamond scriber.

8.1.5 Influence of Dislocations on the Cutting Behavior of Multicrystalline Silicon

The effect of dislocation density on the mechanical properties and the cutting behavior of mc-Si were studied using mono-cast mc-Si material. The study yielded the following key conclusions:

- The presence of dislocations does not alter the hardness and elastic modulus of multicrystalline silicon significantly.
- Regions in the same grain with higher dislocation density are characterized by higher fracture toughness.
- Single grit diamond scribing experiments carried out in the same grain show that the high dislocation density region yields a higher critical depth of cut for ductile-to-brittle transition, which implies greater ductile mode cutting in this region of the mc-Si material.
- The higher fracture toughness in the higher dislocation density regions of the grain also leads to higher specific scribing energy in the brittle cutting regime.

- Scribing across grain boundaries can cause variation in the cutting force due to material anisotropy.

8.2 Discussion

The conclusions of this thesis are expected to be useful in developing a better scientific understanding of the role of fundamental parameters of the diamond wire sawing process. Specifically, the conclusions derived from the comparative study of wafer surface morphology, structural defects such as micro cracks and fracture strengths of slurry and diamond wire sawn wafers indicates the fundamental differences in cutting mechanisms: three body vs. two body wear, and suggests the possibility that diamond wire sawn wafers can be as strong as slurry sawn wafers subject to the loading condition relative to the saw marks.

The modeling and experimental study of single grit diamond scribing of silicon provides insight into the influence of cutting grit shape and frictional conditions on the cutting mode of silicon. This knowledge can serve as a basis for improved design of the diamond wire to minimize saw-induced damage to the wafer surface. Additionally, it provides the understanding necessary to optimize the sawing process parameters such as wire feed rate to achieve satisfactory material removal rates using a specific mode of cutting (ductile or brittle). The studies of the effects of hard inclusions and dislocation clusters on the mechanical properties and cutting performance in mc-Si provide fundamental understanding of the challenges in diamond wire sawing of mc-Si ingots.

8.3 Recommendations for Future Work

The results from the fundamental study of single grit diamond scribing of silicon can be extended to the study of wire sawing performance using a single looped diamond wire, which represents more closely the cutting behavior in multi-wire sawing operation. The interesting research issues in the single loop wire sawing problem may include the following:

- By applying the results of this thesis, namely by properly controlling the shape and size of the diamond cutting grits on the diamond wire, it may be possible to reduce surface/subsurface damage (e.g. microcracks) without compromising productivity.
- The correlation between the cutting forces and cutting performances (e.g. productivity, damage level) and be investigated through modeling and experimental approaches.
- Since a large number of diamond grits are cutting simultaneously, a statistical or stochastic method can be applied to study the effect of cutting parameters (wire speed, feed rate, diamond grit size, etc.) on the cutting performance.
- The detrimental influence of the dynamics and vibration of the wire sawing system on the cutting performance can be studied using analytical and experimental approaches.

REFERENCES

[1] H.J. Möller, C. Funke, M. Rinio and S. Scholz, "Multicrystalline silicon for solar cells", *Thin Solid Films*, 2005. 487: 179-187.

[2] T.J. Jester, "Crystalline silicon manufacturing progress", *Progress of Photovoltaics: Research and Applications,* 2002. 10: 99-106.

[3] C.d. Canizo, G.d. Coso and W.C. Sinke, "Crystalline silicon solar module technology: toward the 1€ per watt-peak goal", *Progress of Photovoltaics: Research and Applications,* 2009. 17: 199-209.

[4] H.J. Möller, "Wafering of silicon crystals", *Physica Status Solidi (a),* 2006. 203 (4): 659-669.

[5] www.Rockwellautomation.com

[6] www.dmt-inc.com

[7] T.G. Bifano, T.A. Dow and R.O. Scattergood, "Ductile-Regime Grinding: A New Technology *for* Machining Brittle Materials", *Journal of Engineering for Industry, ASME Transaction.* 1991. 113(2): 184-189.

[8] G. Du, L. Zhu, P. Rossetto and Y. Wan, "Hard inclusions and their detrimental effects on the wire sawing process of multicrystalline silicon", *Solar Energy Materials & Solar Cells,* 2007. 91: 1743- 1748.

[9] F. Shimura, "Semiconductor Silicon Crystal Technology", Academic Press, San Diego, 1989.

[10] J. Turley and G. Sines, "The anisotropy of Young's modulus, shear modulus and Poisson's ratio in cubic materials", *Journal of Physics D: Applied Physics,* 1971. 4: 264-271.

[11] J.J. Wortman and R.A. Evan, "Young's Modulus, shear modulus, and Poisson's ratio in silicon and germanium", *Journal of Applied Physics,* 1965. 36:153-156.

[12] X. Brun, "Analysis of handling stresses and breakage of thin crystalline silicon wafers", PhD thesis, *Georgia Institute of Technology,* 2008.

[13] R.Hull, "Properties of Crystalline Silicon", 1999, London, United Kingdom: INSPEC Dataviews Series No. 20.

[14] J.Z. Hu, L.D. Merkle, C.S. Menoni and I.L. Spain, "Crystal data for high-pressure phases of silicon", *Physical Review B,* 1986. 34: 4679 - 4684.

[15] M.I. Mcmahon, R. J. Nelmes, N.G. Wright and D.R. Allan, “Pressure dependence of the Imma phase of silicon”, *Physical Review B,* 1994. 50: 739-743.

[16] H. Hanfland, U. Schwarz, K. Syassen and K. Takemura, “Crystal structures of the high-pressure phase silicon VI”, *Physical Review Letter,* 1999. 82:1197-1200.

[17] S. Duclos, Y.Vohra, A. Ruoff, “Experimental study of the crystal stability and equation of state of Si to 248 GPa”, *Physical Review B,* 1990. 41(17): 12021-12028

[18] J. Crain, G.J. Ackland, J.R. Maclean, R.O. Piltz, P.D. Hatton, and G.S. Pawley, “Reversible pressure-induced structural transitions between metastable phases of silicon”, *Physical Review B,* 1994. 50:13043-13046.

[19] S.H. Tolbert, A.B. Herhold, L.E. Brus and A.P. Alivisatos, “Pressure-induced structural transformations in Si Nanocrystals: surface and shape effects”, *Physical Review Letter, 1996.* 76:4384-4387.

[20] T. Juliano, V. Domnich and Y. Gogotsi, “Examining pressure-induced phase transformations in silicon by spherical indentation and Raman spectroscopy: A statistical study”, *Journal of Materials Research,* 2004. 19: 3099-3108.

[21] J. Jang, M.J. Lance, S. Wen, T.Y. Tsui and G.M. Pharr, “Indentation-induced phase transformations in silicon: influences of load, rate and indenter angle on the transformation behavior”, *Acta Materialia,* 2005. 53: 1759-1770.

[22] T. Juliano, Y. Gogotsi and V. Domnich, “Effect of indentation unloading conditions on phase transformation induced events in silicon”, *Journal of Materials Research,* 2003. 18: 1192-1201.

[23] J. Li, I. Kao and V. Prasad, "Modeling stresses of contacts in wire saw slicing of polycrystalline and crystalline ingots: application to silicon wafer production," *Journal of Electronic Packaging, ASME Transactions.* 1998. 120:123-128.

[24] F. Yang and I. Kao, "Interior stress for axisymmetric abrasive indentation in the free abrasive machining process: slicing silicon wafers with model wire saw", *Journal of Electronic Packaging, ASME Transactions.* 1999. 121:191-195.

[25] M. Bhagavat and I. Kao, "Elasto-hydrodynamic interaction in the free abrasive wafer slicing using a wiresaw: modeling and finite element analysis", *Journal of Tribology, ASME Transactions.* 2000. 122: 394-404.

[26] F. Yang and I. Kao, "Free abrasive machining in slicing brittle materials with wire", *Journal of Electronic Packaging, ASME Transactions.* 2001. 123: 254- 259.

[27] B.R. Lawn and A.G. Evans, “Elastic/plastic indentation damage in ceramics: the median/radial crack system”, *Journal of American Ceramic Society*, 1980. 63: 574-581.

[28] D.B. Marshall, B.R. Lawn and A.G. Evans, “Elastic/plastic indentation damage in ceramics: the lateral crack system”, *Journal of American Ceramic Society*, 1982. 65: 561-566.

[29] S. Bhagavat and I. Kao, “A finite element analysis of temperature variation in silicon wafers during wiresaw slicing”, *International Journal of Machine Tool & Manufacture*, 2008. 48(1):95-106.

[30] L.Q. Zhu and I. Kao "Galerkin-based modal analysis on the vibration of wire-slurry system in wafer slicing using a wiresaw”, *Journal of Sound and Vibration*, 2005. 283(3-5): 589-620.

[31] H.J. Möller, “Basic mechanisms and models of multi-wire sawing”, *Advanced Engineering Materials*, 2004. 6(7): 501- 513.

[32] A. Bidiville, K. Wasmer, J. Michler, P.M. Nasch, M. Van der Meer and C. Ballif, “Mechanisms of wafer slicing and impact on wafer properties”, *Progress in Photovoltaics: Research and Application*, 2010. 18: 563-572.

[33] C. Bierwisch, R. Kubler, G. Kleer and M. Moseler, “Modeling of contact regimes in wire sawing with dissipative particle dynamics”, *Philosophical Transactions of The Royal Society: A*, 2011. 369: 2422-2430.

[34] H. Zhao., R. Jin., S. Wu., and J. Shi, “PDE-Constrained Gaussian process model on material removal rate of wire slicing process”, *Journal of Manufacturing Science and Engineering, ASME Transaction*, 2011. 133(2): 021012.

[35] T. Liedke and M. Kuna, "A macroscopic mechanical model of the wire sawing process", *International Journal of Machine Tool & Manufacture*, 2011. 51: 61-64.

[36] S. Arefin, X.P. Li, M. Rahman and K. Liu, “The upper bound of tool edge radius for nanoscale ductile mode cutting of silicon wafer”, *International Journal of Advanced Manufacturing Technology*, 2010. 48: 993-999.

[37] M.B Cai, X.P Li and M. Rahman, “Study of the mechanism of nanoscale ductile mode cutting of silicon using molecular dynamics simulation”, *International Journal of Machine Tool & Manufacture*, 2007. 47(1): 75-80.

[38] K. Liu, X.P. Li and S.Y. Liang, “The mechanism of ductile chip formation in cutting of brittle materials”, *International Journal of Advanced Manufacturing Technology*, 2007. 33: 875-884.

[39] J. Yan, T. Asami, H. Harada and T. Kuriyagawa, "Fundamental investigation of subsurface damage in single crystalline silicon caused by diamond machining", *Precision Engineering*, 2009. 33:378-386.

[40] J.J. Wang and Y.Y. Liao, "Critical depth of cut and specific cutting energy of a microscribing process for hard and brittle materials", *Journal of Engineering Materials and Technology, ASME Transactions*, 2008. 130: 011002.

[41] T. Shibata, S. Fujii, E, Makino and M. Ikeda, "Ductile-regime turning mechanism of single-crystal silicon", *Precision Engineering*, 1996. 18:129-137.

[42] T. Shibata, O. Atsushi, K, Kenji, M. Eiji and I. Masayuki, "Cross-section transmission electron microscope observations of diamond-turned single crystal Si surfaces", *Applied Physics Letters*, 1994. 65(20): 2553-2555.

[43] Y. Gogotsi, G. Zhou, S.S. Ku and S. Cetinkunt, "Raman microspectroscopy analysis of pressure-induced metallization in scratching of silicon", *Semiconductor Science and Technology*, 2001. 16(5): 345-352.

[44] J.C. Morris and D.L. Callahan, "Origins of microplasticity in low-load scratching of silicon", *Journal of Material Research*, 1994. 9 (11): 2907-2913.

[45] N.P. Hung and Y.Q. Fu, "Effect of crystalline orientation in the ductile-regime machining of silicon", *International Journal of Advanced Manufacturing Technology*, 2000. 16: 871-876.

[46] J. Yan, K. Syoji, T. Kuriyagawa and H. Suzuki, "Ductile regime turning at large tool feed", *Journal of Materials Processing Technology*, 2002. 121: 363-372.

[47] C.L. Chao, K.J. Ma, D.S. Liu, C.Y. Bai and T. L. Shy, "Ductile behaviour in single-point diamond-turning of single-crystal silicon", *Journal of Materials Processing Technology*, 2002. 127: 187-190.

[48] B. O'Connor, E. Marsh and J. Couey, "On the effect of crystallographic orientation on ductile material removal in silicon", *Precision Engineering*, 2005. 29: 124-132.

[49] B.R. Lawn and M.V. Swain, "Microfracture beneath point indentation in brittle solids", *Journal of Materials Science*, 1975. 10: 113-122.

[50] A.G. Evans and D.B. Marshall, *Fundamentals of Friction and Wear of Materials*, Ed. By D. A. Rigney, ASME, p. 439.

[51] M. Buijs and K. Korpel-van Houten, "A model for lapping of glass", *Journal of Materials Science*, 1993. 28: 3014-3020.

[52] M. Buijs and K. Korpel-van Houten, "A model for three-body abrasion of brittle materials", *Wear*, 1993. 162-164: 954-956.

[53] S.M. Wiederhorn and B.J. Hockey, "Effect of material parameters on the erosion resistance of brittle materials", *Journal of Materials Science*, 1983. 18: 766-780.

[54] J.L. Routbort and H.J. Matzke, "On the correlation between solid-particle erosion and fracture parameters in SiC", *Journal of Materials Science*, 1983. 18: 1491-1496.

[55] A.K. Mukhopadhyay, D. Chakraborty, M.V. Swain and Y.W. Mai, "Scratch deformation behavior of alumina under a sharp indenter", *Journal of the European Ceramic Society*, 1997. 17: 91-100.

[56] M.A. Moore and F.S. King, "Abrasive wear of brittle solids", *Wear*, 1980. 60: 123-140.

[57] H.H.H. Xu and S. Jahanmir, "Microfracture and material removal in scratching of alumina", *Journal of Materials Science*, 1995. 30: 2235-2247.

[58] B.R. Lwan, "Partial cone crack formation in a brittle material loaded with a sliding spherical indenter", *Proceedings of the Royal Society: A*, 1967. 299: 307-316.

[59] M.V. Sawin, "Microfracture about scratches in brittle solids", *Proceedings of the Royal Society: A.* 1979. 366(1727): 575-597.

[60] A.F. Bower and N.A. Fleck, "Brittle fracture under a sliding line contact", *Journal of the Mechanics and Physics of Solids*, 1994. 42(5): 1375-1396.

[61] X. Jing, S. Maiti and G. Subbash, "A new analytical model for estimation of scratch-induced damage in brittle solids", *Journal of American Ceramic Society*, 2007. 90(3): 885-892.

[62] W. Zhang and G. Subhash, "An elastic-plastic-cracking model for finite element analysis of indentation cracking in brittle materials", *International Journal of Solids and Structures*, 2001, 34/35: 5893-5913.

[63] G. Subhash and W. Zhang, "Finite element analysis of brittle cracking due to single grit rotating scratch", *Journal of Applied Mechanics*, 2003, 70(1): 147-151.

[64] S. Danyluk and R. Reaves, "Influence of fluids on the abrasion of silicon by diamond", *Wear*, 1982. 77: 81-87.

[65] X. Li, J. Lu and S. Yang, "Effect of lubricant on tribo-induced phase transformation of Si", *Tribology Letters*, 2006. 24: 61-66.

[66] H.J. Möller, T. Kaden, S. Scholz and S. Wurzner, "Improving solar grade silicon by controlling entended defect generation and foreign atom defect interactions", *Applied Physics A.* 2009. 96: 207-220.

[67] A. K. Soiland, E.J. Orelid, T.A. Engh, O. Lohne, J.K. Tuset and O. Gjerstad, "SiC and Si3N4 inclusions in multicrystalline silicon ingots", *Materials Science in Semiconductor Processing*, 2004. 7: 39-43.

[68] C.V. Hari Rao, H.E. Bates and K.V. Ravi, "Electrical effects of SiC inclusions in EFG silicon ribbon solar cells", *Journal of Applied Physics*, 1976. 47(6): 2614-2619.

[69] G. Du, N. Chen and P. Rossetto, "On-wafer investigation of SiC and Si3N4 inclusions in multicrystalline Si grown by directional solidification", *Solar Energy Materials & Solar Cells,* 2008. 92: 1059-1066.

[70] G. Du, N. Chen and P. rossetto, "Wire-sawing defects on multicrystalline silicon wafers grown by a directional solidification method", *Semiconductor Science and Technology*, 2008. 23(5): 055011.

[71] H. EI Ghitani and S. Martinuzzi, "Influence of dislocations on electrical properties of large grained polycrystalline silicon cells. I. model", *Journal of Applied Physics,* 1989. 66: 1717-1722.

[72] W. Seifert, G. Morgenstern and M. Kittler, "Influence of dislocation density on recombination at grain boundaries in multicrystalline silicon", S*emiconductor Science and Engineering*, 1993. 8: 1687-1691.

[73] P.B. Hirsch and S.G. Roberts, "The brittle-ductile transition in silicon", *Philosophical Magazine A,* 1991. 64, 55.

[74] K. Sumino, I. Yonenaga, M. Imai and T. Abe, "Effects of nitrogen on dislocation behavior and mechanical strength in silicon crystal", *Journal of Applied Physics,* 1983. 54: 5016-5020.

[75] I. Yonenaga, K. Sumino and K. Hoshi, "Mechanical strength of silicon crystals as a function of the oxygen concentration", *Journal of Applied Physics*, 1984. 56: 2346-2350.

[76] K. Sumino, "Dislocation and mechanical properties of silicon", *Materials Science and Engineering B*, 1989. 4: 335-341.

[77] K. Higashida, M. Tanaka, A. Hartmaier and Y. Hoshino, "Analyzing crack-tip dislocations and their shielding effect on fracture toughness", *Materials Science and Engineering A*, 2008. 483-484: 13-18.

[78] K. Higashida, N. Narita, M. Tanaka, T. Morikawa, Y. Miura and R. Onodera, "Crack tip dislocation in silicon characterized by high-voltage electron microscopy", *Philosophical Magazine A*, 2002. 82: 3263-3273.

[79] M. Tanaka, K. Higashida and T. Haraguchi, "Microstructure of plastic zones around crack tips in silicon revealed by HVEM and AFM", *Materials Science and Engineering A*, 2004. 387-389: 433-437.

[80] I. Zarudi, J. Zou and L.C. Zhang, "Microstructures of phases in indented silicon: A high resolution characterization", *Applied Physics Letters*, 2003. 82(6): 874-876.

[81] A. M. Minor, E.T. Lilleodden, M. Jin, E.A. Stach, D.C. Chrzan and J.W. Morris, JR, "Room temperature dislocation plasticity in silicon", *Philosophical Magazine*, 2005. 85: 323-330.

[82] A. Kailer, Y.G. Gogotsi and K.G. Nickel, "Phase transformation of silicon by contact loading", *Journal of Applied Physics*, 1997. 81: 3057-3063.

[83] E. Smith, G. Dent, "Modern Raman Spectroscopy: A Practical Approach", John Wiley and Sons Ltd, Chichester, UK, 2004.

[84] E.A. Patterson and Z.F. Wang, "Towards full field automated photoelastic analysis of completes components", *Strain*, 1991. 27: 49-53.

[85] S. He, T. Zheng and S. Danyluk, "Analysis and determination of the stress-optic coefficients of thin crystal silicon samples", *Journal of Applied Physics*, 2004. 96: 3103-3109.

[86] A. Bidiville, K. Wasmer. R. Kraft and C. Ballif, "Diamond wire-sawn silicon wafers – from the lab to the cell production", *Proceeding of 24th European Photovoltaic Solar Energy Conference*, Hamburg, Germany, 2009.

[87] R.F. Cook, "Strength and sharp contact fracture of silicon", *Journal of Material Science* 2006. 41: 841-872.

[88] P.A. Wang, "Industrial challenges for thin wafer manufacturing", *Proceedings of the FourthWorld Conference on Photovoltaic Energy Conversion*, Waikoloa, HI, USA, 2006. 1179.

[89] X. Brun and S.N. Melkote, "Analysis of stresses and breakage of crystalline silicon wafers during handling and transport", *Solar Energy Materials & Solar Cells*, 2009. 93: 1238-1247.

[90] P. Rupnowski and B. Sopori, "Strength of silicon wafers: fracture mechanics approach", *International Journal of Fracture*, 2009. 155:67-74.

[91] H. Behnken, M. Apel, D. Franke, "Simulation of mechanical stress during bending tests for crystalline wafers", *Proceedings of the 3rd World Conference on Photovoltaic Energy Conversion*, Osaka, 2003. 1308.

[92] A. Hayter, "Probability and Statistics for Engineers and Scientists", 2nd edn. Duxbury: California, 2002.

[93] B. Yeung and T.Y. Lee, "An overview of experimental methodologies and their applications for die strength measurement", *IEEE Transaction on Components and Packaging Technologies*, 2003. 26: 423-428.

[94] T.L. Anderson, "Fracture Mechanics: Fundamentals and Applications", 3rd ed. Talyor & Francis Group: Florida 2005.

[95] W.A. Weibull, "A statistical theory of strength of materials", *Royal Swedish Institute for engineering Research*, Stockholm, Sweden, 1959.

[96] American Society for Testing and Materials. Standard practice for reporting uniaxial strength data and estimating Weibull distribution parameters for advanced ceramics, C1239-07. Americal Society for Testing and Materials, Philadelphia, PA, USA, 2007

[97] H. Tada, P.C. Paris and G.R. Irwin (Eds.), "The stress analysis handbook", ASME Press: New York 2000.

[98] C.P. Chen and M.H. Leipold, "Fracture toughness of silicon", *American Ceramic Society Bulletin* 1980. 59: 469-472.

[99] J. Bagdahn, J. Schischka, M. Petzold and W.N. Sharpe, "Fracture toughness and fatigue investigations of polycrystalline silicon", *Proceedings of SPIE* 2001. 4558: 159-168.

[100] I. Chasiotis, S.W. Cho and K. Jonnalagadda, "Fracture toughness and subcritical crack growth in polycrystalline silicon", *Journal of Applied Mechanics, ASME Transactions*, 2006. 73:714-722.

[101] American Society for Testing and Materials. "Tentative test method for biaxial flexure strength (modulus of rupture) of ceramic substrates, F394-74T", American Society for Testing and Materials, Philadelphia, PA, USA, 1974.

[102] C. Funke, E. Kullig, M. Kuna and H.J. Moller, "Biaxial fracture test of silicon wafers", *Advanced Engineering Materials* 2004. 6(7):594-598.

[103] K. Mcguire, S. Danyluk, T.L. Baker, J.W. Rupnow and D. Mclaughin, "The influence of backgrinding on the fracture strength of 100 mm diameter (111) p-type silicon wafers", *Journal of Material Sciences*, 1997. 32: 1017-1024.

[104] H. Wu, K, Skenes, C. Yang, F. Mess, S.N. Melkote and S. Danyluk, "Analysis of slurry and fixed abrasive diamond wire sawn silicon wafers", *Proceedings of the 21st Crystalline Silicon Workshop*, Breckenridge, Colorado, 2011.

[105] H. Wu, S.N. Melkote and S. Danyluk, "Mechanical strength of silicon wafers cut by loose abrasive slurry and fixed abrasive diamond wire sawing", *Advanced Engineering Materials*, 2012. 14: 342-348.

[106] N. Watanabe, Y. Kondo, D. Ide, T. Matsuki, H. Takato and I. Sakata. "Characterization of polycrystalline silicon wafers for solar cells sliced with novel fixed-abrasive wire", *Progress in Photovoltaics: Research and Application* 2010; 18: 485-490

[107] T.R. Hsu, "MEMS & Microsystems: Design and Manufacture", McGraw-Hill, New York, 2002.

[108] H. Wu and S.N. Melkote, "Effect of crystallographic orientation on ductile scribing of crystalline silicon: role of phase transformation and slip", *Materials Science and Engineering A*, 2012. 549: 200-205.

[109] J.E. Smith, Jr, M.H. Brodsky, B.L. Crowder and M.I. Nathan, "Raman spectra of amorphous Si and related tetrahedrally bonded semiconductors", *Physical Review Letters*, 1971. 26: 642-646.

[110] H. Alexander and P. Haasen, "Dislocations and plastic flow in the diamond structure", *Solid State Physics*, 1969. 22: 27-158.

[111] H. Saka, A. Shimatani, M. Suganuma and Suprijadi, "Transmission electron microscopy of amorphization and phase transformation beneath indents in Si", *Philosophical. Magazine A*, 2002. 82(10): 1971-1981.

[112] J.E. Bradby, J. Williams, J. Wong-Leung, M.V. Swain and P. Munroe, "Transmission electron microscopy observation of deformation microstructure under spherical indentation in silicon", *Applied Physics Letters*, 2000. 77(23): 3749-3751.

[113] J.E. Bradby, J. Williams, and J. Wong-Leung, "Mechanical deformation in silicon by micro-indentation", *Journal of Material Research*, 2001. 16(5): 1500-1507.

[114] T. Suzuki, S. Takeuchi, H. Yoshinaga, "Dislocation Dynamics and Plasticity", Springer-Verlag, Berlin, 1991.

[115] N. Moes, J. Dolbow and T. Belytschko, "A finite element method for crack growth without remeshing", *International Journal of Numerical Methods in Engineering*, 1999. 46: 131-150.

[116] P.M.A. Areias and T. Belytschko, "Analysis of three-dimensional crack initiation and propagation using the extended finite element method", *International Journal of Numerical Methods in Engineering*, 2005. 63: 760-788.

[117] ABAQUS Analysis User's Manual, Version 6.10.

[118] Y.B. Gerbig, S.J. Stranick, D.J. Morris, M.D. Vaudin and R.F. Cook, "Effect of crystallographic orientation on phase transformations during indentation of silicon", *Journal of Material Research*, 2009. 24(3): 1172-1182.

[119] V.V. Kozhushko and P. Hess, "Comparison of mode-resolved fracture strength of silicon with mixed-mode failure of diamond crystals", *Engineering Fracture Mechanics*, 2010, (77): 193-200.

[120] P.J. Hesketh, C. Ju and S. Gowda, "Surface free energy model of silicon anisotropic etching", *Journal of Electrochemical Society*, 1993. 140(4): 1080-1085.

[121] F.Z. Zhang, H. Wu and Y.C. Liu, "Modeling and experimental investigation on manometric cutting of monocrystalline silicon", *International Journal of Machine Tools and Manufacture*, 2005. 45: 1681-1686.

[122] P.W. Bridgeman, "The effect of hydrostatic pressure on the fracture of brittle substances", *Journal of Applied Physics*, 1947. 18: 246-258.

[123] M. Yoshino, T. Aoki, T. Shirakashi and R. Kumandari, "Some experiments on the scratching of silicon: in situ scratching inside an SEM and sractching under high external hydrostatic pressure", *Journal of Mechanical Sciences*, 2001. 43: 335-347.

[124] J. Bauer, O. Breitenstein and J. Rakotoniaina, "Electronic activity of SiC precipitates in multicrystalline solar silicon", *Physica Status Solidi (a)*, 2007. 204: 2190-2195.

[125] H.J. Möller, T. Kaden, S. Scholz and S. Würzner, "Improving solar grade silicon by controlling extended defect generation and foreign atom defect interactions", *Applied Physics A*, 2009. 96: 207-220.

[126] A. Lotnyk, J. Bauer, O. Breitenstein and H. Blunmtritt, "A TEM study of SiC particles and filaments precipitated in multicrystalline Si for solar cells", *Solar Energy Materials & Solar Cells*, 2008. 92: 1236-1240.

[127] R. Bakowskie, K. Petter, S. Eiternick, D. Lausch and G. Müller, "Efficient methods for detection of SiC and Si_3N_4 precipitates and filaments in multicrystalline silicon wafers and solar cells", *Physica Status Solidi C*, 2011. 8: 1380-1383.

[128] H. Wu and S.N. Melkote, "Modeling and analysis of ductile-to-brittle transition in diamond scribing of silicon: application to wire sawing of silicon wafers", *Journal of Engineering Materials and Technology, ASME Transaction*, 2012. 134: 041011.

[129] H. Wu and S.N. Melkote, "Modeling and experimental study of ductile-to-brittle cutting mode transition in single grit diamond scribing of silicon: application to wire sawing of silicon wafers", *Proceeding of 26th European Photovoltaic Solar Energy Conference,* Hamburg, Germany, 2011, 966- 970.

[130] F. Ebrahimi and L. Kalwani, "Fracture anisotropy in silicon single crystal", *Material Science and Engineering A,* 1999. 268: 116-126.

[131] L.L. Snead, T. Nozawa, Y. Katoh, T. Byun, S. Kondo and D.A. Petti, "Handbook of SiC properties for fuel performance modeling", *Journal of Nuclear Materials,* 2007. 317: 329-377.

[132] A.R. De Arellano-López, M.A. Mcmann, J.P. Singh and J. Martinez-Fernandez, "Microstructure and room-temperature mechanical properties of Si_3N_4 with various α/β phase ratios", *Journal of Materials Science,* 1998. 33: 5803-5810.

[133] Q. Liang, C. Yan, Y. Meng, J. Lai, S. Krasnicki, H. Mao and R.J. Hemley, "Enhancing the mechanical properties of single-crystal CVD diamond", *Journal of Physics: Condensed Matter,* 2009. 21: 364215.

[134] K.H. Yang, "An etch for delineation of defects in silicon", *Journal of the Electrochemical Society,* 1984. 34: 1140-1145.

[135] P.K. Kulshreshtha, K.M. Youssef and G. Rozgonyi, "Nano-indentation: a tool to investigate crack propagation related phase transition in PV silicon", *Solar Energy Materials & Solar Cells,* 2012. 96: 166-172.

[136] J. Woirgard, C. Tromas, J.C. Girard and V. Audurier, "Study of the mechanical properties of ceramic materials by the nanoindentation technique", Journal of the European Ceramic Society, 1998. 18(15): 2297-2305.

[137] K. Niihara, "A fracture mechanics analysis of indentation-induced Palmqvist crack in ceramics", *Journal of Materials Science Letters,* 1983.2: 221-223.

[138] K. Niihara, R. Morena and D.P.H. Hasselman, "Evaluation of K_{Ic} of brittle solids by the indentation method with low crack-to-indent ratios", *Journal of Materials Science Letters,* 1982. 1: 13-16.

[139] Y.Q. Wu and Y.B. Xu, "Direct evidence for microplastic fracture in single-crystal silicon at ambient temperature", *Philosophical Magazine Letters,* 1994.18: 9-13.

[140] A. Carpinteri, "Fractal nature of material microstructure and size effects on apparent mechanical properties", *Mechanics of Materials,* 1994. 18(2): 89-101.